Dear Dr. Maenhaut,

Thank you for considering our manuscript and for your helpful comments on self-absorption correction factors, which we feel have significantly improved the analysis. We have now assessed this correction across the full range of measured elements, and have concluded that it is non-negligible for Na-Ca. We attach a detailed discussion of this issue, together with a revised manuscript and supplement in which our modifications are visible.

Kind regards,

Suzanne Visser and co-authors

Comment:

> *The correction for X-ray self-absorption led to very large changes for the SR-XRF data of the elements Na-Si, with for Si still a decrease by a factor of about 2 in the finest RDI size fraction. As a consequence, a correction for self-absorption is definitely also required for several elements beyond Si, certainly for P, S and Cl, and perhaps even for K and Ca. I suspect that such correction may decrease the SR-XRF data for P and S by 25-30%. Furthermore, the uncertainty that results from the correction for self-absorption should not be limited to the elements Na-Si, but should also be incorporated for the subsequent elements. Thus Table S3 needs to be modified and the total uncertainties should be increased for the elements from P on. Also the data in Table S1 will be affected.*

Response:

We appreciate this comment about self-absorption and have now assessed self-absorption corrections throughout the range of measured elements. To summarize, we find that these effects are significant for elements up to and including Ca (which has approximately a 15 % correction), whereas for heavier elements the correction is negligible (3 % or less). This is discussed in detail below.

In our measurements, self-absorption effects are mainly caused by the large particle size of our calibration standards (9 ± 5 µm) relative to the X-ray penetration depth. Due to the lower XRF response from lighter elements, we use two sets of calibration foils: a heavily loaded set (Na to Ca) and lightly-loaded foils (Ti to Zn). The X-ray penetration depth of these lightly-loaded foils are comparable to those of ambient samples and have an X-ray penetration depth of about 33 µm at 3.7 keV (Ca Kα1 line) or 58 µm at 4.5 keV (Ti Kα1 line). This would yield a self-absorption correction of approximately 6 % for Ca and 3 % for Ti.

However, as noted above, the elements Na to Ca utilize more heavily loaded calibration standards, where the X-ray penetration depth at 3.8 keV (Ca Kα1) is between 10.4 and 14.2 µm, which are comparable to the particle size. This results in significant self-absorption corrections for these elements and additional uncertainties in their calculated concentrations.

We have applied the self-absorption corrections for the elements Na to Ca to all ambient samples. The text, figures and tables in the manuscript and supplement have been revised accordingly. The main changes include (see below):

- The last paragraph of Section 2.2.1, p. 8-9 of the current manuscript.
- Table 2. Self-absorption correction factors.
- Table S3. Estimated total uncertainties of the ambient samples.
- Table S1. S in RDI and AMS.

The last paragraph of Section 2.2.1, p. 8-9 of current manuscript (p. 13-14 of this document) addresses the self-absorption corrections.

"XRF is sensitive to self-attenuation of fluorescence radiation in the sample and depends on the sample composition and density, as well as particle layer thickness or particle size. The PM sample thickness of the coarse and intermediate fractions was maximally 0.7-1.5 µm at a maximum concentration of 10 µg m^{-3} total PM mass for each sample. For these fractions, self-absorption therefore mainly occurs within the individual particles (geometric mean of 5 and 1.6 µm for $PM_{10-2.5}$ and $PM_{2.5-1.0}$ fractions, respectively). For the fine fraction the PM layer is several micrometres thick, resulting in absorption inside the PM layer. However, this layer is mainly composed of species not resolved by SR-XRF (H, C, N, O). Furthermore, most mass of the lightest elements (Na-Ca) is restricted to the coarse and intermediate fractions (except for S and K). We therefore neglect self-absorption effects in the fine fraction samples. The calculated layer thickness of the dried calibration solution on the calibration standards is negligible at 3-60 nm, but the particle size of the dried droplets shows a geometric mean volume size distribution of 9 ± 5 µm and is therefore relevant for self-attenuation. Attenuation factors (AF) were calculated for the calibration standards as well as for the coarse and intermediate fraction samples, as a function of density, mass attenuation coefficient and particle size, according to a simple attenuation model (Table 2; Formenti et al., 2010). For ambient samples and calibration standards, the attenuation length or penetration depth of X-rays for the heavier elements (i.e. above Ca) is greater than 33 µm, resulting in the near-complete excitation of these elements and correction factors below 3 %. Self-absorption correction factors for Na-Ca are non-negligible, as discussed below and in Table 2. The attenuation of the calibration standards is taken into account for all samples, and additional corrections are applied to the coarse and intermediate samples. Calzolai et al. (2010) found comparable self-absorption effects for samples of different composition, total loading and sampling site. Because the elemental composition and particle size distribution of each sample are unknown, we assume a uniform correction for each element within a given size fraction. The overall AF for Na to Ca are 0.52-0.87, 0.30-0.84 and 0.22-0.82 for coarse, intermediate and fine fraction samples, respectively."

Table 2. Self-absorption correction factors.

	Calibration standard 1		Calibration standard 2		$PM_{10-2.5}$ sample		$PM_{2.5-1.0}$ sample				
Particle size (µm)[a]	9.0		9.0		5.0		1.6				
Density (g cm-3)[b]	2.19		2.27		2.00		2.00		Total correction factor[d]		
	AF[c]	*a*[c]	AF[c]	*a*[c]	AF[c]	*a*[c]	AF[c]	*a*[c]	$PM_{10-2.5}$ sample	$PM_{2.5-1.0}$ sample	$PM_{1.0-0.3}$ sample
Na	0.22	0.49			0.43	0.40	0.74	0.40	0.52	0.30	0.22
Mg			0.32	0.33	0.58	0.25	0.83	0.25	0.55	0.38	0.32
Al	0.43	0.23			0.70	0.15	0.89	0.15	0.61	0.48	0.43
Si			0.51	0.17	0.79	0.10	0.93	0.10	0.64	0.55	0.51
P	0.60	0.13			0.85	0.07	0.95	0.07	0.70	0.63	0.60
S			0.65	0.10	0.90	0.04	0.97	0.04	0.72	0.67	0.65
Cl	0.71	0.08			0.88	0.05	0.96	0.05	0.80	0.73	0.71
K			0.79	0.05	0.94	0.03	0.98	0.03	0.84	0.81	0.79
Ca	0.82	0.05	0.76	0.06	0.95	0.02	0.98	0.02	0.87[e]	0.84[e]	0.82[e]

[a] Particle size given as geometric mean diameter.

[b] Average density of the calibration standards and of ambient aerosol. The composition of calibration standard 1 is $Na_{3.76}Al_{3.76}P_{3.76}Cl_{3.76}Ca_{3.76}CoN_8O_{24}$, of calibration standard 2 $Mg_{3.76}Si_{3.76}S_{3.76}K_{3.76}Ca_{3.76}CoN_7O_{21}$, and of ambient samples $C_{39}H_{29}N_{10}O_{18}S_3Fe$.

[c] Attenuation factors and a (μm^{-1}; $a = 2/3 * \mu * \rho$ with μ the mass attenuation coefficient ($cm^2\ g^{-1}$) and ρ the particle mass density ($g\ cm^{-3}$)) according to Eq. (4) in Formenti et al. (2010).

[d] Total correction factor defined as ratios AF calibration standard / AF sample. Self-absorption effects are neglected in the $PM_{1.0-0.3}$ samples; therefore these samples are only corrected for AF calibration standards.

[e] Ca is corrected based on the average AF of calibration standards 1 and 2, and a calibration standard used to calibrate the elements Ti to Zn at SLS (Ca present in all three standards).

Data for this third calibration standard are: particle size of 7.0 ± 2 µm, average density of 2.37 g cm^{-3} and AF and *a* for Ca of 0.89 and 0.03 $µm^{-1}$, respectively.

The uncertainties associated with the self-absorption effects for the elements Na to Ca (54-9 %) have been added to Table S3.

Table S3. Estimated total uncertainty (% of measured value) of the calculated element concentrations per size fraction, and detection limits for each element (ng m^{-3}).

Element	$PM_{10-2.5}$ (%)[a]	$PM_{2.5-1.0}$ (%)[a]	$PM_{1.0-0.3}$ (%)[a]	DL (ng m^{-3})[b]
Na	59	59	60	2.552
Mg	55	55	55	0.962
Al	48	48	48	1.709
Si	43	43	43	0.420
P	37	37	37	0.118
S	34	34	34	0.503
Cl	31	31	31	0.158
K	28	28	28	0.031
Ca	23	23	23	0.267
Ti	24	26	27	0.024
V	30	30	24	0.008
Cr	27	27	26	0.015
Mn	83	69	46	0.042
Fe	21	21	21	0.033
Ni	22	22	21	0.005
Cu	21	21	21	0.028
Zn	21	21	21	0.058
Br	21	21	21	0.117
Sr	21	21	21	0.036
Zr	21	21	21	0.036
Mo	21	21	21	0.037
Sn	21	21	21	0.061
Sb	21	21	21	0.052
Ba	21	21	21	0.254
Pb	21	21	21	0.137

[a] Combination of uncertainties regarding sample inhomogeneity (20 %), self-absorption corrections (Na 54, Mg 49, Al 41, Si 35, P 27, S 23, Cl 19, K 13 and Ca 9 %)[d], RDI flow rate (5 %), absolute and relative calibration (Na-K 13 %, Ca-Pb 2 %) and spectral analysis specific per element and size fraction (median uncertainties for all data points).

[b] Taken as 3x the standard deviation of the spectra signals used for continuum corrections.

[c] Na uncertainties might be underestimated due to the overlap with the L lines of Ni, Cu and Zn. In the current analysis the ratio of the Lα to Kα lines are determined empirically, and quantification of the associated uncertainties is under investigation.

[d] Uncertainties regarding self-absorption corrections are based on the microscopic analysis of the particle size on the calibration standards. The particle size of the dried droplets shows a geometric mean of the volume size distribution of 9 µm, and 50 % of the particles are in the range 4-14 µm (see also Table 2 in main text).

The self-absorption correction for S of 35 % for the finest size fraction results in a change in the comparison between S from the RDI $PM_{1.0\text{-}0.3}$ fraction and backup filters and S from the AMS, as discussed in Supplement A. Meanwhile, we have also received revised AMS data from all three measurement sites. These changes together have led to reasonable mass-closure between both measurement methods with RDI to AMS ratios of 0.67-1.26.

In Supplement A:

Table S1 compares the S concentrations from the RDI $PM_{1.0\text{-}0.3}$ stage with S (from SO_4^{2-}) collected by the backup filter. The sum of both (Total S < 1 µm) is compared with S from AMS sulphate measurements. The ratios of 0.67 to 1.26 in the last column reveal reasonable mass-closure between the RDI and AMS.

Table S1. Comparison between S from RDI $PM_{1.0\text{-}0.3}$ fractions and backup filters (S from SO_4^{2-}) with S from the AMS (S from SO_4^{2-}). Units in ng m^{-3}. The ratio of S in the RDI to the AMS is given in the last column (ratio of RDI Total S < 1 µm to AMS S).

Site	RDI $PM_{1.0\text{-}0.3}$ S	S in backup filter	Total S <1 µm	AMS S	Ratio RDI : AMS
MR	127	398	525	607	**0.86**
NK	113	405	518	412	**1.26**
DE	145	359	504	749	**0.67**

Kerb and urban increment of highly time-resolved trace elements in PM_{10}, $PM_{2.5}$ and $PM_{1.0}$ winter aerosol in London during ClearfLo 2012

S. Visser[1], J.G. Slowik[1], M. Furger[1], P. Zotter[1], N. Bukowiecki[1], R. Dressler[2], U. Flechsig[3], K. Appel[4*], D.C. Green[5], A.H. Tremper[5], D.E. Young[6], P.I. Williams[6,7], J.D. Allan[6,7], S.C. Herndon[8], L.R. Williams[8], C. Mohr[9], L. Xu[10], N.L. Ng[10,11], A. Detournay[12], J.F. Barlow[13], C.H. Halios[13], Z.L. Fleming[7,14], U. Baltensperger[1] and A.S.H. Prévôt[1]

[1] {Laboratory of Atmospheric Chemistry, Paul Scherrer Institute, Villigen, Switzerland}

[2] {Laboratory of Radiochemistry and Environmental Chemistry, Paul Scherrer Institute, Villigen, Switzerland}

[3] {Swiss Light Source, Paul Scherrer Institute, Villigen, Switzerland}

[4] {HASYLAB, DESY Photon Science, Hamburg, Germany}

[5] {School of Biomedical Sciences, King's College London, London, UK}

[6] {School of Earth, Atmospheric and Environmental Sciences, University of Manchester, Manchester, UK}

[7] {National Centre for Atmospheric Science, University of Manchester, Manchester, UK}

[8] {Aerodyne Research, Inc., Billerica, MA, USA}

[9] {Department of Atmospheric Sciences, University of Washington, Seattle, WA, USA}

[10] {School of Chemical and Biomolecular Engineering, Georgia Institute of Technology, Atlanta, GA, USA}

[11] {School of Earth and Atmospheric Sciences, Georgia Institute of Technology, Atlanta, GA, USA}

[12] {Centre for Ecology and Hydrology, Penicuik, Midlothian, Scotland}

[13] {Department of Meteorology, University of Reading, Reading, UK}

[14] {Department of Chemistry, University of Leicester, Leicester, UK}

[*] {now at: European XFEL, Hamburg, Germany}

Correspondence to: M. Furger (markus.furger@psi.ch)

Abstract

Ambient concentrations of trace elements with 2 h time resolution were measured in $PM_{10-2.5}$, $PM_{2.5-1.0}$ and $PM_{1.0-0.3}$ size ranges at kerbside, urban background and rural sites in London during winter 2012. Samples were collected using rotating drum impactors (RDIs) and subsequently analysed with synchrotron radiation-induced X-ray fluorescence spectrometry (SR-XRF). Quantification of kerb and urban increments (defined as kerb-to-urban and urban-to-rural concentration ratios, respectively), and assessment of diurnal and weekly variability provided insight into sources governing urban air quality and the effects of urban micro-environments on human exposure. Traffic-related elements yielded the highest kerb increments, with values in the range of 10.4 to 16.6 for SW winds (3.3-6.9 for NE) observed for elements influenced by brake wear (e.g. Cu, Sb, Ba) and 5.7 to 8.2 for SW (2.6-3.0 for NE) for other traffic-related processes (e.g. Cr, Fe, Zn). Kerb increments for these elements were highest in the $PM_{10-2.5}$ mass fraction, roughly 2 times that of the $PM_{1.0-0.3}$ fraction. These elements also showed the highest urban increments (~ 3.0), although no difference was observed between brake wear and other traffic-related elements. All elements influenced by traffic exhibited higher concentrations during morning and evening rush hour, and on weekdays compared to weekends, with the strongest trends observed at the kerbside site, and additionally enhanced by winds coming directly from the road, consistent with street canyon effects. Elements related to mineral dust (e.g. Al, Si, Ca, Sr) showed significant influences from traffic-induced resuspension, as evidenced by moderate kerb (3.4-5.4 for SW, 1.7-2.3 for NE) and urban (~ 2) increments and increased concentrations during peak traffic flow. Elements related to regional transport showed no significant enhancement at kerb or urban sites, with the exception of $PM_{10-2.5}$ sea salt (factor of up to 2), which may be influenced by traffic-induced resuspension of sea and/or road salt. Heavy duty vehicles appeared to have a larger effect than passenger vehicles on the concentrations of all elements influenced by resuspension (including sea salt) and wearing processes. Trace element concentrations in London were influenced by both local and regional sources, with coarse and intermediate fractions dominated by traffic-induced resuspension and wearing processes and fine particles influenced by regional transport.

1 Introduction

Ambient particulate matter (PM) has long been recognized to have a detrimental effect on public health in urban areas (e.g. Dockery and Pope, 1994). Of particular interest are particles with an aerodynamic diameter less than 10 µm (PM_{10}) as these particles can penetrate deeply into the lungs (Franklin et al., 2008; Zhou et al., 2011). Reche et al. (2012) reported even higher toxicity to human cells for the $PM_{2.5-1.0}$ than for the $PM_{10-2.5}$ fraction. Particle toxicity is known to vary significantly with PM composition and emission sources (Kelly and Fussell, 2012), with identified toxic constituents including soluble secondary inorganic particles, elemental and organic carbon, and especially metals. Effective mitigation strategies therefore require detailed, size-dependent characterization of particle composition and emission sources.

In addition to their direct effects on human health, metals and trace elements are of importance because their high source specificity and atmospheric stability make them effective tracers for source apportionment. In Europe, four main source types in PM_{10} are commonly identified: vehicles (with tracers including e.g. Fe, Ba, Zn, Cu), crustal materials (e.g. Al, Si, Ca, Fe), sea salt (mainly Na, Cl, Mg) and mixed industrial/fuel-oil combustion (mainly V, Ni, S) and secondary aerosol (mainly S) (Putaud et al., 2010; Viana et al., 2008). The contribution of mineral dust and sea salt in most urban areas is larger in PM_{10} than in $PM_{2.5}$ (Harrison et al., 2001; Weijers et al., 2011). Emissions from vehicle exhaust, industry and secondary aerosol are predominantly emitted and formed as $PM_{1.0}$ or in $PM_{2.5}$ (Bukowiecki et al., 2010; Harrison et al., 2011; Richard et al., 2011). Several of these sources have been directly linked to adverse health effects. For example, the largest aerosol source of human toxicity in Barcelona was attributed to traffic activities (encompassing vehicle emissions, road dust and secondary nitrate), with fuel oil combustion and industrial emissions also contributing to increased cancer risk (Reche et al., 2012). Turoczi et al. (2012) observed higher toxicity from direct emissions (e.g. from traffic) than from photochemically processed aerosol.

The Clean Air for London project (ClearfLo; www.clearflo.ac.uk) is a multinational effort to elucidate the processes driving poor air quality in London, implemented through comprehensive measurements of particle- and gas-phase composition, and meteorological parameters (Bohnenstengel et al., 2014). ClearfLo builds upon recent modelling and monitoring studies in London (Arnold et al., 2004; Bohnenstengel et al., 2011; Bohnenstengel et al., 2013; Harrison et al., 2012a; Mavrogianni et al., 2011). Despite improved air quality, PM_{10} concentrations are not decreasing, resulting in frequent exceedances of the daily PM_{10} limit (Harrison et al., 2008). Such exceedances are caused by complex interactions of regional and local emission sources, together with meteorological factors such as wind speed, air mass origin, and daily cycles of the atmospheric boundary layer (Charron and Harrison, 2005; Harrison and Jones, 2005; Jones et al., 2010). Currently, emissions by industrial sources and stationary combustion are modest, while traffic is thought to contribute up to 80 % of the total PM_{10} in London, compared to less than 20 % for the entire UK, according to emission inventories between 1970 and 2001 (Dore et al., 2003).

The spatial density of emission sources found in typical urban environments leads to elevated particle concentrations compared to nearby rural locations. As an example, buildings may influence local meteorology by restricting air circulation (street canyon effect), producing human exposures that are orders of magnitude higher than those predicted by regional dispersion models (Zhou and Levy, 2008). This provides both acute exposure risk and increased long-term exposure for those passing through regularly, thereby producing a non-negligible impact on public health. To assess the impact of such micro-environments, we here investigate London trace element concentrations in terms of increments, defined as the concentration ratios between an environment of interest and a reference site (e.g. Charron et al., 2007).

Only a few studies have investigated trace elements through simultaneous measurements at multiple sites. Harrison et al. (2012b) reported increments of kerbside to urban background sites in London for non-size segregated aerosol with a time resolution of 1 to 4 days. Theodosi et al. (2011) found that at urban and suburban sites in Athens and a regional site in Finokalia, Greece crustal elements dominate coarse particles ($PM_{10-2.5}$), whereas anthropogenic sources such as fossil fuel combustion were confined to fine particles (V, Ni and Pb have > 70 % of their mass in $PM_{1.0}$). Bukowiecki et al. (2009a) and Bukowiecki et al. (2010) examined trace elements in $PM_{10-2.5}$, $PM_{2.5-1.0}$ and $PM_{1.0-0.1}$ aerosol at street canyon and urban background sites in Zürich, Switzerland, and showed increasing increments (note: 1 means no increment) with particle size from about 1.2 (fine mode) to 2.4 (coarse mode) (averaged over all elements). All these studies report increments close to 1 for elements originating from regional sources such as sea salt and Saharan dust, while local, especially traffic-related sources yield increments around 2 for resuspension-related elements and between 3 and 5 for traffic-related elements. Additionally, the 1 h time resolution used by Bukowiecki et al. (2009a) and Bukowiecki et al. (2010) enabled identification of enhanced increments for resuspension and wearing related elements like Si and Sb during peak traffic flows.

There is a need for more high time-resolved size segregated increment analyses to assess the exposure to trace elements from emission sources within urban areas under varying meteorological conditions. Here we present size segregated measurements of aerosol trace elements with 2 h time resolution performed simultaneously at kerbside and urban background sites in London, and a rural site outside London. We assess the effects of urban micro-environments on human exposure to particulate pollutants through the quantification of urban and kerb increments. These exposures are further investigated in terms of contributing emission sources, diurnal and weekly variability, local wind patterns, and regional transport effects.

2 Methods

2.1 Measurement campaigns

The ClearfLo project was a measurement program in and around London lasting two years (2011-2012) and including two month-long Intensive Observation Periods (IOPs) in 2012 (Bohnenstengel et al., 2014). This paper focuses on the winter IOP lasting from 6 January to 11 February 2012. Measurements took place at three sampling sites located at or near permanent air quality measurement stations in the Automatic Urban and Rural Network (AURN): a kerbside site close to a very busy road, an urban background site in a residential area, and a rural background site away from direct emission sources (see Fig. 1).

The urban background sampling site was at the grounds of the Sion Manning Secondary School in North Kensington (NK, lat 51°31’21’’N, lon 0°12’49’’W). NK is situated within a highly trafficked suburban area of London (Bigi and Harrison, 2010; Harrison et al., 2012a). During the ClearfLo IOPs this site served as the main measurement site and was upgraded with a full suite of particle- and gas-phase instruments, and instruments to measure meteorological parameters (Bohnenstengel et al., 2014). The kerbside site was located at Marylebone Road (MR, lat 51°31’21’’N, lon 0°09’17’’W) about 4.1 km to the east of NK (Charron and Harrison, 2005; Harrison et al., 2011). This site is located at the southern side of a street canyon, with an axis running approximately 260° to 80°. Measurements took place at 1 m from a busy six-lane road with a traffic flow of approximately 73 000 vehicles per day of which 15 % consist of heavy duty vehicles. Braking and stationary vehicle queues are frequent at the site due to a heavily used pedestrian light-controlled crossing (65 m west of MR) and a signal-controlled junction (200 m west of MR). The rural site at the Kent Showgrounds at Detling (DE, lat 51°18′07″N, lon 0°35′22″E) was approximately 45 km to the southeast of London downtown on a plateau at 200 m a.s.l. surrounded by fields and villages, and was close to the permanent measurement station of Kent and Medway Air Quality Monitoring Network. The site provides excellent opportunities to compare the urban and kerbside air pollution with the rural background pollution levels (Bohnenstengel et al., 2014; Mohr et al., 2013). A busy road with ~ 160 000 vehicles per day is located approximately 150 m south of DE. Meteorological parameters were measured at DE and at the British Telecom (BT) Tower (lat 51°31’17”N, lon 0°08’20”W), ~ 0.5 km east of MR (Harrison et al., 2012a).

2.2 Instrumentation

2.2.1 RDI-SR-XRF

Rotating drum impactors

Rotating drum impactors (RDIs) were deployed at MR, NK and DE with a 2 h time resolution (see Table 1 for details). A detailed description of the RDI can be found in Bukowiecki et al. (2005), Bukowiecki et al. (2009c) and Richard et al. (2010). In short, aerosols are sampled through an inlet that removes all particles with aerodynamic diameter $d > 10$ µm at a flow rate of 1 m^3 h^{-1}. The particles are size segregated in three size ranges based on d ($PM_{10-2.5}$ (coarse), $PM_{2.5-1.0}$ (intermediate) and $PM_{1.0-0.3}$ (fine)) by passing sequentially through three rectangular nozzles of decreasing size. Particle deposition occurs via impaction on 6 µm thick polypropylene (PP) foils mounted on aluminium wheels and coated with Apiezon to minimize particle bouncing effects. After the last impaction stage a backup filter samples all remaining particles before the air passes through a pump. After each 2 h sampling interval the three wheels rotate stepwise to a blank section of the foil before a new sampling interval takes place. The small-size collection limit of the fine fraction was previously estimated at 100 nm (Bukowiecki et al., 2009c; Richard et al., 2010). However, new laboratory measurements of the RDI collection efficiency indicate an instrument-dependent (i.e. based on the machining of the specific nozzle) small-end cut point of approximately 290-410 nm (see Supplement A for details). This results in sampling of a smaller size range ($PM_{1.0-0.3}$) than the $PM_{1.0-0.1}$ range reported in previous studies, and influences the measured concentrations of elements with significant mass near this cut point (S, K and Pb).

SR-XRF analysis

Trace element analysis on the RDI samples was performed with synchrotron radiation-induced X-ray fluorescence spectrometry (SR-XRF) at the X05DA beamline (Flechsig et al., 2009) at the Swiss Light Source (SLS) at Paul Scherrer Institute (PSI), Villigen PSI, Switzerland and at Beamline L at Hamburger Synchrotronstrahlungslabor (HASYLAB) at Deutsches Elektronen-Synchrotron (DESY), Hamburg, Germany (beamline dismantled November 2012). The samples with the deposited particles were placed directly into the X-ray beam. Irradiation of the samples took place at a 45° angle for 30 s. The light spot of the incoming beam was ~ 140 by 70 µm at SLS (monochromatic excitation at 10.5 keV, in vacuum) and ~ 80 by 150 µm at HASYLAB (polychromatic excitation, in air). Fluorescence light produced by the elements in the samples was detected by energy-dispersive detectors (silicon drift detector at SLS, nitrogen cooled Si(Li)-detector at HASYLAB) at a 90° angle relative to the incoming beam. At SLS Kα lines of the elements with atomic number Z = 11-30 (Na-Zn) were measured, and at HASYLAB Kα lines of the elements with Z = 22-56 (Ti-Ba) and Lα lines of Z = 82 (Pb).

The fluorescence counts per element were calibrated to the element mass concentration using multi-element standards, where each standard consisted of a set of preselected elements in 5 different concentrations ranging between 0.05 and 0.4 µg cm^{-2}. The absolute element concentrations in these standards were determined with inductively coupled plasma-optical emission spectroscopy (ICP-OES). The absolute calibration factor for the SR-XRF system was referenced to Fe and determined from the linear relation between the SR-XRF response and the ICP-OES measurements. Because the fluorescence yield increases with atomic number Z, a relative calibration curve was constructed as follows: for each element present in the standards and having a detectable Kα_1 line, an absolute calibration factor was determined as for Fe, and a dimensionless relative response factor was calculated as the ratio of this absolute factor to that of Fe. These relative response factors were plotted as a function of line energy and a polynomial curve was fit to obtain response factors by interpolation for elements not present in the standard. In total 25 elements were quantified (Na, Mg, Al, Si, P, S, Cl, K, Ca, Ti, V, Cr, Mn, Fe, Ni, Cu, Zn, Br, Sr, Zr, Mo, Sn, Sb, Ba, Pb). Details of the methodology can be found elsewhere (Bukowiecki et al., 2005; Bukowiecki et al., 2008; Richard et al., 2010), with the following significant changes (see Supplement B for further details):

1. At SLS, we used an e2v SiriusSD detector (SiriusSD-30133LE-IS) and in-house built vacuum chamber to extend the measured range of elements down to Na and Mg.

2. Reference standards for calibration of element fluorescence counts to mass concentrations were produced on the same 6 µm PP substrate as used for RDI sampling allowing the use of identical geometry and irradiation time for RDI samples and reference standards, thereby reducing uncertainties in absolute and relative calibrations.

3. Data were processed with the Spectral Analysis for Multiple Instruments – toolkit for XRF (SAMI-XRF) developed in-house within the IGOR Pro software environment (Wavemetrics, Inc., Portland, OR, USA). SAMI handles spectral fitting, quantification of associated uncertainties, and calculation and application of calibration parameters.

XRF is sensitive to self-attenuation of fluorescence radiation in the sample and depends on the sample composition and density, as well as particle layer thickness or particle size. The PM sample thickness of the coarse and intermediate fractions was maximally 0.7-1.5 µm at a maximum concentration of 10 µg m^{-3} total PM mass for each sample. For these fractions, self-absorption therefore mainly occurs within the individual particles (geometric mean of 5 and 1.6 µm for PM$_{10\text{-}2.5}$ and PM$_{2.5\text{-}1.0}$ fractions, respectively). For the fine fraction the PM layer is several micrometres thick, resulting in absorption inside the PM layer. However, this layer is mainly composed of species not resolved by SR-XRF (H, C, N, O). Furthermore, most mass of the lightest elements (Na-Ca) is restricted to the coarse and intermediate fractions (except for S and K). We therefore neglect self-absorption effects in the fine fraction samples. The calculated layer thickness of the dried calibration solution on the calibration standards is negligible at 3-60 nm, but the particle size of the dried droplets shows a geometric mean volume size distribution of 9 ± 5 µm and is therefore relevant for self-attenuation. Attenuation factors (AF) were calculated for the calibration standards as well as for the coarse and intermediate fraction samples, as a function of density, mass attenuation coefficient and particle size, according to a simple attenuation model (Table 2; Formenti et al., 2010). For ambient samples and calibration standards, the attenuation length or penetration depth of X-rays for the heavier elements (i.e. above Ca) is greater than 33 µm, resulting in the near-complete excitation of these elements and correction factors below 3 %. Self-absorption correction factors for Na-Ca are non-negligible, as discussed below and in Table 2. The attenuation of the calibration standards is taken into account for all samples, and additional corrections are applied to the coarse and intermediate samples. Calzolai et al. (2010) found comparable self-absorption effects for samples of different composition, total loading and sampling site. Because the elemental composition and particle size distribution of each sample are unknown, we assume a uniform correction for each element within a given size fraction. The overall AF for Na to Ca are 0.52-0.87, 0.30-0.84 and 0.22-0.82 for coarse, intermediate and fine fraction samples, respectively."

~~XRF is sensitive to self-attenuation of fluorescence radiation in the sample and depends on the sample composition and density, as well as particle layer thickness or particle size. The PM sample thickness of the coarse and intermediate fractions was maximally 0.7-1.5 µm at a maximum concentration of 10 µg m^{-3} total PM mass for each sample. For these fractions, self-absorption therefore mainly occurs within the individual particles (geometric mean of 5 and 1.6 µm for PM$_{10-2.5}$ and PM$_{2.5-1.0}$ fractions, respectively). For the fine fraction the PM layer is several micrometres thick, resulting in absorption inside the PM layer. However, most mass of the lightest elements (Na-Si) is restricted to the coarse and intermediate fraction. We therefore neglect self-absorption effects in the fine fraction samples. The calculated layer thickness of the dried calibration solution on the calibration standards is negligible at 3-60 nm, but the particle size of the dried droplets shows a geometric mean volume size distribution of 9 ± 5 µm and is therefore relevant for self-attenuation. Attenuation factors (AF) were calculated for the calibration standards as well as for the coarse and intermediate fraction samples for Na, Mg, Al and Si, as a function of density, mass attenuation coefficient and particle size, according to a simple attenuation model (Table 2; Formenti et al., 2010). The AF of heavier elements were negligible within the measurement uncertainties. The attenuation of the calibration standards is taken into account for all samples, and additional corrections are applied to the coarse and intermediate samples. Calzolai et al. (2010) found comparable self-absorption effects for samples of different composition, total loading and sampling site. Because the elemental composition and particle size distribution of each sample are unknown, we assume a uniform correction for each element within a given size fraction. The overall AF are 0.22-0.52, 0.32-0.55, 0.43-0.61 and 0.51-0.64 for Na, Mg, Al and Si, respectively (calculated as correction factor of calibration standard/sample).~~

2.2.2 Other measurements

Here a short description is given of relevant particle- and gas-phase instruments deployed at MR, NK and DE during the winter IOP. Daily PM_{10} filter samples (midnight to midnight) were collected at MR and NK using Partisol 2025 samplers (Thermo Scientific, Inc.). The filters were digested in a 1:2 mixture of perchloric and hydrofluoric acid, and subsequently analysed by ICP-mass spectrometry (ICP-MS, calibration with NIST standards) for the determination of Na, Al, Ca, Ti, V, Mn, Fe, Ni, Cu, Zn, Sr, Mo, Sb, Ba and Pb. Additionally, Mg, K and Sn were available at NK. High-resolution time-of-flight aerosol mass spectrometers (HR-ToF-AMS, Aerodyne Research, Inc., Billerica, MA, USA) were deployed at MR (5 min time resolution), NK (5 min resolution every 30 min), and DE (2 min resolution) to characterise the non-refractory submicron aerosol components (DeCarlo et al., 2006). PM_{10} mass concentrations were measured at all three sites with FDMS-TEOM (Filter Dynamics Measurement System Tapered Element Oscillating Microbalances; Thermo Scientific, Inc.) with a 1 h time resolution. NO_x measurements at MR and NK were performed with a NO_x chemiluminescent analyser with a single chamber and a single detector (API, A Series, model M200A; 15 min resolution). At DE NO was determined with a Thermo Scientific 42i analyser and NO_2 with an Aerodyne CAPS-NO_2 (SN 1002) and an Aerodyne QCL-76-D. These NO and NO_2 measurements were summed together to obtain NO_x (1 min resolution). Black carbon (BC) was measured with a 2-wavelength Aethalometer (λ = 370 and 880 nm, model AE22, Magee Scientific) at MR and a 7-wavelength Aethalometer (λ = 370-950 nm, model AE31, Magee Scientific) at NK and DE (5 min resolution), with a 2.5 µm cyclone at MR and DE and a 3.5 µm cyclone at NK. Traffic counts by vehicle group at MR from road sensors (number of vehicles per 15 min) were available as well. Wind direction and wind speed data for MR and NK were taken from the BT Tower (30 min resolution) where anemometers were placed to the top of an open lattice scaffolding tower of 18 m height on top of the main structure (190.8 m a.g.l.; Wood et al., 2010), whereas local data were used at DE (1 min resolution). Air mass origins were analysed with back trajectory simulations using the UK Met Office's Numerical Atmospheric Modelling Environment (NAME) dispersion model (Jones et al., 2007).

3 Data intercomparison and uncertainty

Here we compare RDI-SR-XRF data with independent filter data (24 h PM_{10} trace element data analysed with ICP-MS; roughly 9 % uncertainty at a 95 % confidence interval) for 18 elements collected at MR and NK (no filter data was available at DE). For this comparison, the three size ranges of the RDI were summed up to total PM_{10} and averaged to the filter collection period. Details of the intercomparison results can be found in Supplement C. In short, the majority of the elements (Al, Ca, Ti, Mn, Fe, Cu, Zn, Sr, Sb, Ba) agree within approximately ± 50 % with Pearson's $R > 0.78$. Na and Mg agree as well, but have higher uncertainties due to self-absorption corrections. For the other elements, disagreement can be attributed to low or unknown filter sample extraction efficiencies (Ni, Mo) and differences in the particle size range sampled by the two measurement techniques (K, V, Sn, Pb). However, all elements are retained in the ensuing analysis as (1) they yield internally consistent results, as described in the following sections; (2) the ensuing analysis relies on relative changes/ratios per element across sites and is therefore not affected by a systematic bias in absolute magnitude.

The agreement between XRF and filter measurements in the present study compares favourably with that obtained in previous intercomparisons of trace element measurement techniques. Comparison of RDI-SR-XRF with daily element concentrations from a high volume sampler followed by subsequent analysis using laboratory-based wavelength dispersive XRF (Bukowiecki et al., 2005) and by ICP-OES and ICP-MS (Richard et al., 2010) yielded slopes between 0.7 and 1.6 (except for S and K) with Pearson's $R > 0.5$. The spread/biases in these intercomparisons are not necessarily due to SR-XRF issues, as can be seen from a comparison by Salcedo et al. (2012) of ICP with proton-induced X-ray emission (PIXE) and AMS trace element measurements. Agreement between ICP and PIXE data was in the same range as between either method and the AMS data, with slopes ranging between 0.06 and 0.93 with Pearson's R from about 0.3 to 0.7.

Estimated uncertainties (per size fraction) and detection limits for each measured element are given in Supplement Table S3. A brief overview is presented here:

1. RDI sampling: the fluctuations in the flow rate are negligible within 5 % (Richard et al., 2010) and the uncertainties in the size cut off are discussed in Supplement A.

2. SR-XRF accuracy: uncertainties in the absolute and relative calibrations affect absolute/fractional concentrations, but cancel out for relative changes/ratios, because all samples were measured under the same calibration conditions.

3. Issues such as imperfect flatness of the sample foils and detector dead time corrections (Richard et al., 2010) reduce measurement precision but affect all elements with the same scaling factor.

4. SR-XRF measurement precision is affected by sample inhomogeneity, spectral analysis and self-absorption correction uncertainties. Sample inhomogeneity was assessed by Bukowiecki et al. (2009c) and found to contribute ± 20 % uncertainty.

For most elements, except Mn and the lightest elements, sample inhomogeneity is the largest source of uncertainty. Mn is affected by spectral analysis uncertainties due to peak overlap with Fe, which is present in much higher concentrations. Therefore, a small bias in the energy calibration as function of detector channel leads to a large change in the peak area of Mn. Self-absorption effects are a significant source of uncertainty for the lightest elements (Na-~~Si~~Ca), but the good comparisons to the filter data suggest that the corrections lead to reasonable results. All data points lie well above their element detection limits, resulting in negligible uncertainties from the signal strength. In addition, RDI-SR-XRF measurements (both absolute/fractional and relative/ratio) are affected by atmospheric variability. This variability is likely the predominant source of the data spread evident in Table and the following analyses.

4 Results and discussion

4.1 Trace element concentrations

During the ClearfLo winter IOP total mass concentrations of the analysed trace elements ranged from less than 0.1 µg m^{-3} to ~ ~~13~~10 µg m^{-3}. Typically, concentrations were highest at MR and lower at NK and DE, and decreased with particle size. An overview of the obtained trace element concentrations as a function of size and site is given in Table 3. Note that S is not a trace element, but is commonly reported in trace element studies and is a good tracer for regional transport. Among the analysed trace elements, highest concentrations at MR were found for Na (28 %), Cl (~~28~~25 %)~~, Na (27 %)~~ and Fe (~~21~~22 %). At NK this was the case for Na (39 %), Cl (~~33~~29 %)~~, Na (22 %)~~ and Fe (11 %) and at DE Na (40 %), Cl (~~30~~28 %)~~, Na (25 %)~~ and ~~S (20 %)~~Fe (8 %). Total analysed mass measured by the RDI-SR-XRF (trace elements + S) contributed on average ~~16~~14 % to the total PM$_{10}$ mass (from FDMS-TEOM) of 32 (5-74) µg m^{-3} at MR (not extrapolated to the corresponding oxides), ~~12~~10 % to the mass of 23 (1.4-63) µg m^{-3} at NK and ~~10~~7.4 % to the mass of 17 (0.5-58) µg m^{-3} at DE.

A comparison between the contributions of coarse, intermediate and fine fractions to the total PM$_{10}$ mass of each trace element is shown in Fig. 2 for the three sites. Trace elements at MR are dominated by the coarse fraction. Analysis in the following sections and previous measurements at this site (Charron and Harrison, 2005) suggest this is caused by large contributions of resuspension and traffic-related mechanical abrasion processes, which primarily contribute to the coarse fraction. For all elements at this site, except S, Br and Pb, the coarse fraction contributes more than 50 %. Mass fractions of intermediate mode elements to total PM_{10} are rather constant with contributions ranging from ~~13~~11 to 27 %. The fine fraction contributes up to 50 % of total mass for S, K, Zn, Br and Pb; for other elements fine contributions are less than 20 %. S, K, Zn, Br and Pb are typically dominated by the fine fraction with known sources including heavy oil combustion (S, K, Zn; Lucarelli et al., 2000), traffic exhaust (Br, Pb; Formenti et al., 1996), industrial processes (Zn, Pb; Moffet et al., 2008), and secondary sulphate and wood combustion (S, K, Pb; Richard et al., 2011).

For most elements, particle mass contributions of the smaller size fractions are more important as one moves from kerbside to urban background to rural sites (Fig. 2). The relatively large fine fraction contribution at DE is probably caused by the absence of local traffic which results in lower contributions of resuspension and traffic-related processes to total element concentrations. A different behaviour is observed for Cr, Ni and Mo with on average 80 % of their mass at DE in the coarse fraction, compared to 73 % at MR and 60 % at NK. The time series of these coarse mode species are very spiky, are slightly enhanced with SW winds, but are not collocated with measurements of BC and AMS species, suggesting emissions from a local industrial source, potentially from stainless steel production (Querol et al., 2007; Witt et al., 2010) near DE rather than regional transport.

Comparing the contributions of groups of elements to total trace element concentrations at the sites provides an overview of local and regional sources affecting London; a detailed source apportionment study will be the subject of a future manuscript. Na, Mg and Cl are typical sea salt elements and contribute around ~~58~~66 % to the total PM_{10} trace element mass at all three sites, indicating that the air pollutant levels caused by elements are dominated by natural emission sources being transported to London. Mineral dust elements (Al, Si, Ca, Ti) mainly brought into the air via resuspension contribute on average ~~12~~13 % at MR, NK and DE. For some specific brake wear elements (Cu, Sb, Ba) these contributions are 1.5, ~~0.7~~0.6 and 0.4 % at MR, NK and DE, respectively. Although these metals contribute a small fraction of total PM_{10} mass concentrations, they induce adverse health effects. Xiao et al. (2013) e.g. found that Zn, Fe, Pb and Mn were the major elements responsible for plasmid DNA damage, whereas Kelly and Fussell (2012) found that increases in PM_{10} as a result of increased Ni, V, Zn and Cu contributions showed highest mortality risks, as opposed to increased Al and Si.

4.2 Urban and kerb increment

4.2.1 Urban increment

The urban increment compares the trace element concentrations at the urban background site to the concentrations at the rural site, and is calculated here as the ratio of concentrations at NK to DE. Figure 3 shows the mean, median and 25-75th percentile urban increment ratios for the coarse, intermediate and fine fractions per element. Most elements, except Ni and coarse mode Cr are enriched at the urban background site by factors between 1.0 and 6.5 (median ratios). Increments decrease towards smaller sizes. Ni and coarse mode Cr show higher concentrations at DE relative to NK, as does the mean value of coarse Mo. Especially at DE Cr and Ni show strong correlations with Pearson's R of 0.85. As discussed in the previous section, enhanced coarse mode Cr, Ni and Mo may indicate an industrial source near the rural site.

Coarse mode Zr exhibits low concentrations at DE, where the median value actually falls below detection limit, though discrete events above detection limit also exist. For this reason, the median-based urban increment is not plotted, while the mean ratio is driven by several large concentration peaks at NK, resulting in a large mean ratio of 21. In the case of Cl, a large spread in the urban increment values is seen for all three size ranges. Cl is likely depleted relative to other sea salt elements like Na and Mg (throughout the campaign Cl concentrations fall to 0, whereas Na and Mg concentrations remain positive) due to replacement by nitrate, and the extent of such depletion is greater in small particles (Nolte et al., 2008). At DE, Cl depletion seems apparent at all size ranges, whereas at MR depletion mainly takes place in the $PM_{1.0-0.3}$ fraction. NK shows Cl depletion especially in the $PM_{1.0-0.3}$ fraction, but to some extent also in intermediate mode particles.

For ease of discussion, we empirically group elements based on similar urban increment values. Mn, Fe, Cu, Zn, Zr, Mo, Sn, Sb and Ba show urban increments on average of 3.5 in the coarse, 3.1 in the intermediate and 2.0 in the fine fraction (Fig. 3). These have been identified as traffic-related elements by e.g. Amato et al. (2011); Bukowiecki et al. (2010); Minguillón et al. (2014); Richard et al. (2011) and Viana et al. (2008). Zr has also been linked to mineral dust (Moreno et al., 2013). We can understand that from analysing the Enrichment Factors of these elements (EF). EF is a measure of the enrichment of elements relative to the upper continental crust (UCC) and is defined as ppm metal in the sample / ppm metal in UCC with Si as reference material (UCC from Wedepohl, 1995). Zr is the only element in this traffic group that is depleted in the atmosphere relative to their UCC concentrations, but with concentrations at NK higher than at DE. Most other elements clearly indicate anthropogenic origin with EF > 10. Dependent on the method, Zr can be either grouped with traffic-related elements or with dust elements. The urban increments are similar to that of NO$_x$, where concentrations at NK were on average a factor 4.9 higher than at DE (the mean concentration at NK was 68 ppb, at DE 14 ppb). Black carbon (BC), a marker for both traffic and wood burning emissions, had an urban increment of only 1.1 (concentration at NK 757 ng m^{-3}, at DE 633 ng m^{-3}), likely due to local wood burning emissions around DE (Mohr et al., 2013). Al, Si, Ca, Ti and Sr as markers for mineral dust (e.g. Amato et al., 2009; Lin et al., 2005; Lucarelli et al., 2000) show a factor 2.0 higher concentrations at NK relative to DE in the coarse, 1.9 in the intermediate and 1.6 in the fine fraction (EF < 10). These results indicate that moving from rural to urban backgrounds yields a larger relative increase in traffic than in mineral dust elements. Surprisingly, sea salt elements (Na, Mg, Cl) show higher concentrations at NK than at DE of up to a factor of 2 for the coarse mode, despite the expected dominance of regional over local sources. This highlights the potential importance of sea or road salt resuspension by traffic. Similar urban increment values for traffic-related, resuspension and sea salt elements have been observed by Lee et al. (1994) for particles below a few µm. Theodosi et al. (2011) also found higher increments (> 2) for trace elements in PM$_{10}$ aerosol from local anthropogenic sources like fossil fuel combustion (V, Ni, Cd) and traffic (Cu), relative to long-range transported Saharan dust (Fe, Mn) with increments close to 1. However, our study suggests that the non-size-resolved increment values reported in the cited studies do not fully capture the urban/rural differences.

The influence of regional transport by anthropogenically produced elements (Fig. 3) is seen by the low urban increments between 1.1 and 1.8 for P, S, K, Zn, Br, Sn and Pb in PM$_{1.0-0.3}$ (EF > ~~25~~22) and of 1.6 for total PM$_{10}$ mass (concentration at NK 23 µg m^{-3}, at DE 17 µg m^{-3}). The concentrations of the main components in PM$_{10}$ (sulphate, nitrate and secondary organic compounds) within an urban area are mostly influenced by regional transport, as found in London during the REPARTEE project (Harrison et al., 2012a) and in Paris during the MEGAPOLI project (Crippa et al., 2013; Freutel et al., 2013), resulting in low increments for total PM_{10} mass. Similar urban increment values (1.3 to 1.8) for 1 and 24 h total $PM_{2.5}$ mass concentrations were reported across many sites in the UK (Harrison et al., 2012c).

4.2.2 Kerb increment

While the urban increment investigates the effect of diffuse emission sources on particle concentrations, the kerb increment investigates an urban micro-environment, specifically the local effects of roadside emissions and activities. Here, the kerb increment is calculated as the ratio of concentrations at MR to NK. However, observed concentrations at MR strongly depend on wind direction, because the road runs from approximately 260° to 80° and the street canyon with the surrounding buildings and intersections creates a complex wind circulation system (Balogun et al., 2010). Since the measurement station is located at the southern side of the canyon, measurements during time periods with winds from the south are influenced by on-road emissions on top of the urban background pollution. Higher concentrations were observed with SSE winds, i.e. perpendicular to the direction of the road by e.g. Balogun et al. (2010), Charron and Harrison (2005) and Harrison et al. (2012b).

In this study, the RDI-SR-XRF data was split into four equally spaced wind direction sectors based on wind direction data; N (315-45°), E (45-135°), S (135-225°) and W (225-315°). Figure 4 shows size-resolved trace element concentrations per wind sector normalized to the global median concentration for each element at MR. As expected, winds from the south yield the highest concentrations, whereas northern winds yield the lowest, independent of size fraction. West and east winds are parallel to the street canyon and yield intermediate concentrations. Similar behaviour is observed for NO_x, and no directional biases for high wind speeds are observed (Supplement Fig. S6).

Traffic-related and some other anthropogenically-related elements (V, Cr, Mn, Fe, Ni, Cu, Zn, Zr, Mo, Sn, Sb, Ba) show the strongest wind direction dependency with up to a factor of 2-3 higher concentrations during S relative to N winds for the three size fractions (Fig. 4). A factor of 1.5-2 is obtained for resuspended dust elements. Harrison et al. (2012b) found a ratio of 2 for Fe (as tracer for brake wear) and 1.2 for Al (as tracer for mineral dust) for SW versus NE winds for particles between 2 and 3 µm. However, they were limited by their time resolution of several days, resulting in potentially substantial wind direction variations during each measurement, which would blur the different conditions and yield reduced ratios.

Other elements show only minor correlations with wind direction (Fig. 4), indicating more influence from regional transport, instead of being locally affected by traffic. Only fine mode S, K and Br seem to be enriched with winds from the east, potentially related to long-range transport from the European continent.

Local wind direction has a greatly reduced effect at urban background and rural sites. At NK, the element concentrations are only subject to high concentration outliers for E winds (Supplement Fig. S4), potentially caused by the transport of pollutants from downtown London, or by lower wind speeds occurring with E winds resulting in reduced dilution and increased concentrations of traffic pollutants (e.g. NO_x) throughout the city (Supplement Fig. S6). The rural site hardly shows wind direction dependent concentrations (Supplement Fig. S5-6). Interpretation of data from the E sector is unclear due to the low number of data points (45 out of 318 data points). Only data from the N sector show enhanced concentrations for several elements correlating with higher wind speeds and back trajectories consistent with transport from continental Europe.

To simplify reporting of the kerb increment and facilitate comparison with previous studies (e.g. Harrison et al., 2012b), we combined the south/west sectors and the north/east sectors into SW (135-315°) and NE (315-135°) sectors. To eliminate meteorological and/or regional transport effects, this segregation is performed at both MR and NK. The kerb increment is then calculated as the ratio of MR to NK and shown in Fig. 5 (Supplement Fig. S7 shows the increments for the 4 individual sectors). As with the urban increment, we focus on the ratio of the medians at MR and NK to reduce the effects of outliers. Two features become directly visible; the kerb increment is much higher for coarse than for intermediate and fine particles, and kerb increments are much higher for SW than for NE wind conditions. With the latter, kerb increments are on average 2.7, 1.6 and 1.7 for coarse, intermediate and fine mode particles, respectively. This significant enhancement is likely due to recirculation of particles within the street canyon following their resuspension and/or emission by traffic. However, these increments are much smaller than those observed in the SW sector, where enhancements relative to NK of 6.7, 3.3 and 3.1 (coarse, intermediate, fine) are observed. These results indicate the existence of micro-environments within the street canyon dependent on wind direction.

As in the previous discussion, we again group elements by kerb increment (Fig. 5). The first group consists of Cu, Zr, Mo, Sn, Sb and Ba and yields the highest increments in the coarse mode ranging from 10.4 to 16.6 in the SW sector (3.3-6.9

for NE). These elements are typically associated with brake wear (e.g. Bukowiecki et al., 2009b; Harrison et al., 2012b), and are much higher than the increments of 4.1 to 4.4 reported by Harrison et al. (2012b) at the same sites for particles < 21 µm. They assigned Fe, Cu, Sb and Ba to brake wear, but in the current study Fe has a significantly lower kerb increment than other brake wear tracers, suggesting a significant alternative source. When combining all size fractions and ignoring wind direction influences, increments in this study are about 4.9, and more similar to previous studies. The discrepancies between the kerb increments obtained using these two calculation strategies highlights the difficulties in characterizing human exposure to locally generated pollutants in urban environments, as the detailed topography and microscale meteorology greatly alter particle concentrations, and the effects are size-dependent. Amato et al. (2011) calculated road side increments in Barcelona for trace elements in PM_{10} with a 1 h time resolution and found increments for brake wear elements of only 1.7 (based on Fe, Cu, Sb, Cr, Sn). These low increments are probably due to the reduced dispersion in Barcelona caused by a complex topography, resulting in high urban background levels.

The second group consists of V, Cr, Mn, Fe, Ni, Zn and Pb with increments of 5.7-8.2 ($PM_{10-2.5}$) in the SW sector (2.6-3.0 for NE) (Fig. 5). V and Ni are typically assigned to industrial sources and heavy-oil combustion (e.g. Mazzei et al., 2007; Viana et al., 2008), Zn is usually associated with tire wear (e.g. Harrison et al., 2012b; Lin et al., 2005), and the other elements are commonly associated with traffic-related emissions (e.g. Amato et al., 2013; Bukowiecki et al., 2009a; Richard et al., 2011). We label this group as anthropogenically-influenced (ANTH). The EF of V, Cr and Ni are much lower than those of the other elements in this group (4 vs. > 10), indicating at least to some extent different source origins. These kerb increments are similar to the ones for NO_x of 8.5 for SW and 2.4 for NE, confirming the anthropogenic influence (traffic and other sources) on these elements. The high braking frequency at MR due to congested traffic probably resulted in increased kerb increments of brake wear relative to ANTH elements that are also influenced by local traffic and other sources around NK. Increments of these ANTH elements are higher than previously reported values of 1.8-4.5 for studies with low time resolution and non-size segregated particles (Boogaard et al., 2011; Janssen et al., 1997). The high increments presented here might be caused by street canyon effects, trapping pollutants emitted at street level and preventing dilution to the urban background. The enhanced kerb increments for brake wear relative to ANTH elements are apparent in all three size fractions, although increments become more similar towards smaller sizes with a factor 1.7 between both element groups in the coarse, 1.5 in the intermediate and 1.4 in the fine mode. Both groups show the additional information gained with size-segregated aerosol, where exposure to trace elements in the street canyon relative to the urban background increases with particle size, either caused by increased traffic-related emissions with particle size or by more efficient transport of submicron particles from street sites to the urban background. Furthermore, the highly time-resolved element measurements presented here enabled us to resolve the systematic, wind direction dependent variability in kerb increments.

The third group is associated with mineral dust (Al, Si, Ca, Ti, Sr) with coarse mode increments of 3.4-5.4 for SW winds (1.7-2.3 for NE) (Fig. 5). These elements are brought into the air both by traffic-induced resuspension and transport from other locations. This second process increases both urban background and kerbside concentrations, and thus reduces kerb increments relative to direct traffic-related elements. Lower kerb increments for mineral dust than traffic-related elements are generally observed in increment studies (Amato et al., 2011; Boogaard et al., 2011; Bukowiecki et al., 2009b; Harrison et al., 2012b), although the dust increments found in this study are larger than most reported increments (typically 1-2). As in the traffic-related groups, increments increase with particle size, indicating enhanced human exposure at the street side of particles above 1 µm.

Na, Mg and Cl (sea salt) form the fourth group and yield kerb increments of 1.0 to 2.7, independent of size fraction but with slightly enhanced ratios with SW compared to NE winds (Fig. 5). Similar increments were observed for total PM_{10} mass. As discussed for urban increments, even though these elements have regional sources, they are influenced by resuspension processes within the urban area which are enhanced at kerbside sites.

The remaining elements (P, S, K, Br) can be grouped together. In the coarse mode, these elements yield increments similar to the mineral dust group, indicating that this group is influenced by resuspension processes in the street canyon (Fig. 5). However, especially in the fine mode increments around 1 were found, consistent with regional transport dominating over local emission sources.

4.3 Temporal trends in trace element concentrations

In contrast to traditional trace element measurements, the RDI-SR-XRF enables measurement of element concentrations with high time resolution (2 h in this work). This enables investigation of diurnal cycles, which are useful both for source discrimination and in determining the processes contributing to elevated PM levels. We also discuss weekly cycles, which can be useful in distinguishing emissions from heavy duty and passenger vehicles (HDV and LDV); HDV numbers typically diminish during the weekend. Back trajectory analysis aids source discrimination by understanding regional transport influences by different air mass origin. Here we discuss the temporal trends of trace elements in five groups based on expected sources and the increment analyses in Sect. 4.2, in order of increasing local influence: regional background, sea salt, mineral dust, traffic-related and brake wear.

Figures 6 and 7 show size-segregated median diurnal and weekly cycles, respectively, for 5 elements representative of the classes mentioned above: Na (sea salt), Si (mineral dust), S (regional background), Fe (traffic-related) and Sb (brake wear) at the three sites. Because of the wind direction effect evident at MR, diurnal cycles at all three sites are shown for SW and NE winds. Wind direction analyses are not incorporated into the weekly cycles because the month-long campaign provided insufficient data points for meaningful division. This also means that weekly cycles are subject to influences by mesoscale events. For example, sea salt shows no clear weekly cycle, except for a peak on Fridays in intermediate and fine fractions coinciding with westerly winds, which coincidentally occurred more frequently on Fridays than on other days. Except for such events, regionally dominated elements tend to display flat, featureless diurnal/weekly cycles, while elements dominated by recurring local processes (e.g. traffic patterns) show interpretable features. Diurnal and weekly cycles of all other elements can be found in Supplement Fig. S8-9. For comparison, diurnal and weekly cycles of NO_x and total PM_{10} mass at all sites, and of traffic flow at MR are shown in Fig. 8. The time series of these species were averaged to the RDI collection times before obtaining the cycles. BC diurnal and weekly cycles (not shown) are very similar to those of NO_x.

4.3.1 Regional influences

Elements dominated by regional sources (P, S, K, Br) occur mainly in the fine fraction and are similar to total PM_{10} mass in showing no obvious diurnal and weekly patterns. This interpretation is consistent with the urban/kerb increment analysis discussed in Sect. 4.2. Weekly patterns suggest fine Zn and Pb are also dominated by regional transport (Supplement Fig. S9). P, S and K have been identified as tracers for mixed wood combustion and secondary sulphate (Amato et al., 2011; Richard et al., 2011), whereas Hammond et al. (2008) have identified S, K and Pb from mixed secondary sulphate and coal combustion. Br is usually associated with sea salt (Lee et al., 1994; Mazzei et al., 2007) or traffic emissions (Gotschi et al., 2005; Lee et al., 1994), but Maenhaut (1996) has also found Br, together with S, K, Pb and other elements in biomass burning. In this study, the diurnal cycle of fine Br is different from the Na, Mg and Cl cycles, but more similar to K. Br is thus likely more associated with wood burning than with other sources.

The time series of fine S, K, Zn, Pb at NK (very similar at MR and DE) are explored in relation to total PM_{10} mass, wind direction and air mass origin, and compared to representative elements from the other emission groups (coarse Na, Si, S, Sb; Fig. 9). Air mass origin was studied with back trajectories simulated for three case study periods (marine, European mainland and locally influenced) using the NAME model (Jones et al., 2007). Particles are released into the model atmosphere from the measurement location and their origin is tracked using meteorological fields from the Unified Model, a numerical weather prediction model. Each particle carries mass of one or more pollutant species and evolves by various physical and chemical processes during 24 h preceding arrival at NK. Potential emission source regions can be highlighted along the pathway to the measurement site at 0-100 m above ground.

Under marine air mass origin (case A, 18-24 January, Fig. 9) with strong W winds the concentrations of the fine mode elements are fairly low, whereas sea salt concentrations are enhanced (see Na in Fig. 9). Although the air mass has also passed over Ireland and the Midlands, the influence of these rather sparsely populated regions on pollution levels seems small. This is confirmed by low total PM_{10} mass and NO_x concentrations. Enhanced fine fraction and total PM_{10} mass concentrations (latter not shown) occur during north easterlies with high wind speeds from the European mainland (case B) bringing in pollutants through regional transport.

During this episode, both the urban background and rural site observed the highest concentrations for these trace elements of the entire campaign. Traffic influenced species were not enhanced during this pollution episode. Elevated concentrations of all trace elements, NO_x and PM_{10} mass occurred only during a local pollution episode of roughly 3 days caused by local air mass stagnation over London and the south eastern UK (case C). The very high concentrations observed in case B through regional transport from the European mainland were identified as the main reason for PM_{10} limit exceedances at urban background sites in London by Charron et al. (2007), while exceedances were much less frequent under marine influenced air as represented by case A in this study.

4.3.2 Sea salt

The sea salt group yields comparable, rather flat diurnal cycles for fine and intermediate mode Na, Mg and Cl, and coarse mode Na and Cl (Na in Fig. 6; others in Supplement Fig. S8), and no obvious weekly patterns (Na in Fig. 7; others in Supplement Fig. S9). This indicates that the regional transport of sea salt is probably the main source of Na, Mg and Cl, as seen in case A in Fig. 9.

Interestingly, although coarse mode sea salt exhibits no obvious temporal trend, the urban and kerb increments indicate additional source contributions besides regional transported sea salt. The urban increment might be caused by the natural sea salt gradient observed in the UK, with reducing concentrations from west to east (Fowler and Smith, 2000), while the kerb increment could be the result of road salt resuspension in addition to sea salt resuspension. Coarse mode Mg originates probably both from mineral dust and sea salt, because at MR with SW winds Mg correlates with Al and Si temporal trends, while with NE winds Mg correlates better with Na and Cl.

4.3.3 Mineral dust and traffic

Both mineral dust and traffic-related elements are strongly influenced by traffic patterns at MR, which are shown in Fig. 8 as the number of vehicles per 2 h split in LDV and HDV (shorter/longer than 5.2 m). HDV numbers peak in the morning, whereas LDV numbers peak in the evening when the flow of traffic leaves the urban area, consistent with Harrison et al. (2012b). A single peak during midday in the weekend compared to a double peak at weekdays is observed for LDV. HDV numbers show a similar pattern during weekdays, but with a reduced maximum on Saturday and a small maximum that is shifted towards midday on Sunday. Charron and Harrison (2005) reported similar traffic patterns during two years of traffic counts, and stated very small week-to-week variability, except during holidays.

The element diurnal (Fig. 6 for Si, Fe and Sb; Supplement Fig. S8 for others) and weekly (Fig. 7 for Si, Fe and Sb; Supplement Fig. S9 for others) cycles yield highest concentrations at MR and lower concentrations at NK and DE, consistent with observed urban and kerb increments. More importantly, and only retrievable with high time-resolved data, concentrations are higher during the day than at night, with night time concentrations at MR and NK similar to median urban background and rural concentrations, respectively, demonstrating the effects of local traffic and enhanced human exposure during daytime. Weekdays yield stronger increments than weekends and closely follow NO_x and HDV traffic patterns (Fig. 8), indicating the strong influence of these vehicles on element concentrations. This confirms observations by Charron et al. (2007), who stated that PM_{10} limit exceedances at MR are more likely to occur on weekdays, in combination with large regional contributions from the European mainland with easterly winds. Similarly, Barmpadimos et al. (2011) found strong weekly cycles for $PM_{10-2.5}$ and $PM_{2.5}$ mass concentrations in Switzerland over a 7-12 year period, with higher concentrations on weekdays and lowest on Sundays.

In the street canyon with SW winds, all coarse mode elements (including dust elements) except Na and Cl exhibit a double peak in the diurnal cycles, closely following the flow of traffic and confirming that traffic-related processes such as braking and resuspension dominate the concentration of most elements. With NE winds, source discrimination is possible between mineral dust (Si in Fig. 6) and traffic-related elements (Fe and Sb in Fig. 6). Mineral dust yields a strong maximum between 8:00 and 14:00 LT, and continued high concentrations throughout the day, while the traffic-related group yields a reduced double peak relative to SW winds. The increase in dust concentrations coincides with the start of traffic flows at 6:00 LT resulting in resuspension of particles within the street canyon. However, concentrations decrease before traffic flows reduce, possibly as a result of increased mixing and dilution during boundary layer growth. At NK diurnal and weekly patterns of the dust and traffic groups yield similar variability but reduced concentrations relative to MR, which suggests increased human exposure during day time and weekdays and confirms that traffic dominates urban background element concentrations in London (see Dore et al., 2003). At DE, freshly emitted pollutants from London and other cities in the south eastern UK have been diluted and mixed with other pollutants during their transport to the rural background, resulting in no obvious diurnal and weekly patterns independent of size range.

The kerb increments at MR under SW winds were divided into two traffic-related groups: brake wear and other traffic-related elements. However, the diurnal and weekly cycles of all these elements correlate well and no obvious split into two groups is seen. Apparently, both groups are co-emitted as a single group under comparable vehicle fleet and/or set of driving conditions, at least on a 2 h time scale, but in different ratios at MR and NK. The ratio of these two element classes for SW to NE wind sectors at MR is almost 2, with the lack of difference between these classes supporting co-emission. In a future manuscript we will further explore the diurnal variability of emission sources at both sites with statistical analyses based on the Multilinear Engine (Canonaco et al., 2013; Paatero, 1999).

5 Conclusions

Aerosol trace element composition was measured at kerbside, urban background and rural sites in the European megacity of London during winter 2012. Sampling with rotating drum impactors (RDI) and subsequent measurements with synchrotron radiation-induced X-ray fluorescence spectrometry (SR-XRF) yielded trace element mass concentrations in $PM_{10-2.5}$, $PM_{2.5-1.0}$ and $PM_{1.0-0.3}$ aerosol with a 2 h time resolution. Total median element mass concentrations of ~~4.0~~4.1, ~~2.0~~2.1 and ~~0.7~~1.0 $\mu g\ m^{-3}$ were found at kerbside, urban background and rural sites, respectively, which constitutes ~~10~~ to ~~16~~14 % to total PM_{10} mass (highest at kerbside; lowest at rural site), neglecting the corresponding oxides. The contribution of emission sources to coarse fraction elements was on average largest at kerbside (65 %) and reduced for urban background (~~51~~52 %) and rural sites (49 %).

Urban and kerb increments were defined as the concentration ratios of urban background to rural, and kerbside to urban background, respectively, and the kerb increments were further explored as a function of wind direction. The group with the largest kerb increments consisted of elements typically associated with brake wear (Cu, Zr, Mo, Sn, Sb, Ba). The second largest kerb increments were observed for anthropogenically-influenced elements typically assigned to non-brake wear traffic emissions (Cr, Mn, Fe, Zn, Pb) but also V and Ni. This could indicate either a traffic source for these elements or a similar kerbside-to-urban emission gradient. Kerb increments were larger for the brake wear group and under SW winds due to local street canyon effects, with coarse fraction increments between 10.4 and 16.6 for SW winds (3.3-6.9 for NE winds) against increments for the anthropogenically-influenced group between 5.7 and 8.2 for SW winds (2.6-3.0 for NE winds). The kerb increments for all these elements in the $PM_{10-2.5}$ size fraction are roughly twice that of the $PM_{1.0-0.3}$ fraction. Urban increments (no distinction between both groups) were around 3.0. In addition to direct emissions, traffic-related processes influence the concentrations of other elements by resuspension, with mineral dust (Al, Si, Ca, Ti, Sr) increments of 1.3-3.3.

The highly time-resolved data enabled studying diurnal patterns. The cycles of mineral dust elements and coarse Na, Mg and Cl both indicate major concentration enhancements during periods of heavy traffic, whereas regionally-influenced elements (fine P, S, K, Zn, Br, Pb) showed no enhancements. All traffic-related elements at the kerbside site yielded temporal patterns similar to variations in heavy duty vehicle numbers as opposed to total vehicle numbers, and resulted in enhanced exposure to elements during day time and weekdays. Traffic-related processes therefore exhibit a dominant influence on air quality at the kerbside and urban background sites, and should be the main focus of health effect studies and mitigation strategies. With technological improvements for the reduction of traffic exhaust emissions, the traffic contribution to coarse PM is becoming more important as shown by decreasing $PM_{2.5}$ mass trends with no significant changes of coarse PM (Barmpadimos et al., 2012).

Trace element and total PM_{10} mass concentrations are also affected by mesoscale meteorology, increasing with the transport of air masses from the European mainland. Under these conditions, coarse and intermediate fraction trace elements are hardly affected, but fine fraction elements showed elevated concentrations. Trace element concentrations in London are therefore influenced by both local and regional sources, with coarse and intermediate fractions dominated by anthropogenic activities (particularly traffic-induced resuspension and wearing processes), whereas fine fractions are significantly influenced by regional processes.

These observations highlight both the strong influence of regional factors on overall air quality, as well as the need for detailed characterization of urban micro-environments for accurate assessment of human exposure to airborne particulates and the associated health risks.

Acknowledgements

This research, which was conducted in the context of the ClearfLo project, is mainly financed by the Swiss National Science Foundation (SNSF grant 200021_132467/1), the ClearfLo project (NERC grant NE/H00324X/1) and the European Community's

Seventh Framework Programme (FP/2007-2013, grant number 312284). The Detling site was supported by the US Department of Energy Atmospheric Systems Research Program (DOE Award No. DE-SC0006002). J.G. Slowik acknowledges support from the SNSF through the Ambizione program (grant PX00P2_31673). Filter digestions were carried out by the wet geochemistry laboratory at Royal Holloway, University of London. Empa loaned us a RDI during the ClearfLo project. Parts of the work were carried out at the Swiss Light Source, Paul Scherrer Institute, Villigen, Switzerland. We thank Andreas Jaggi for technical support at the beamline X05DA. Parts were performed at the light source facility DORIS III at HASYLAB/DESY. DESY is a member of the Helmholtz Association (HGF). We thank Christophe Frieh for excellent support in acquiring and testing the detector, and we thank Peter Lienemann and Sylvia Köchli for valuable input for the production of calibration standards.

References

Amato, F., Pandolfi, M., Escrig, A., Querol, X., Alastuey, A., Pey, J., Perez, N., and Hopke, P. K.: Quantifying road dust resuspension in urban environment by Multilinear Engine: A comparison with PMF2, Atmos. Env., 43, 2770-2780, 2009.

Amato, F., Viana, M., Richard, A., Furger, M., Prevot, A. S. H., Nava, S., Lucarelli, F., Bukowiecki, N., Alastuey, A., Reche, C., Moreno, T., Pandolfi, M., Pey, J., and Querol, X.: Size and time-resolved roadside enrichment of atmospheric particulate pollutants, Atmos. Chem. Phys., 11, 2917-2931, 2011.

Amato, F., Schaap, M., Denier van der Gon, H. A. C., Pandolfi, M., Alastuey, A., Keuken, M., and Querol, X.: Short-term variability of mineral dust, metals and carbon emission from road dust resuspension, Atmos. Env., 74, 134-140, 2013.

Arnold, S. J., ApSimon, H., Barlow, J., Belcher, S., Bell, M., Boddy, J. W., Britter, R., Cheng, H., Clark, R., Colvile, R. N., Dimitroulopoulou, S., Dobre, A., Greally, B., Kaur, S., Knights, A., Lawton, T., Makepeace, A., Martin, D., Neophytou, M., Neville, S., Nieuwenhuijsen, M., Nickless, G., Price, C., Robins, A., Shallcross, D., Simmonds, P., Smalley, R. J., Tate, J., Tomlin, A. S., Wang, H., and Walsh, P.: Introduction to the DAPPLE Air Pollution Project, Sci. Total Environ., 332, 139-153, 2004.

Balogun, A. A., Tomlin, A. S., Wood, C. R., Barlow, J. F., Belcher, S. E., Smalley, R. J., Lingard, J. J. N., Arnold, S. J., Dobre, A., Robins, A. G., Martin, D., and Shallcross, D. E.: In-street wind direction variability in the vicinity of a busy intersection in central London, Bound.-Layer Meteor., 136, 489-513, doi:10.1007/s10546-010-9515-y, 2010.

Barmpadimos, I., Nufer, M., Oderbolz, D. C., Keller, J., Aksoyoglu, S., Hueglin, C., Baltensperger, U., and Prévôt, A. S. H.: The weekly cycle of ambient concentrations and traffic emissions of coarse (PM10–PM2.5) atmospheric particles, Atmos. Env., 45, 4580-4590, 2011.

Barmpadimos, I., Keller, J., Oderbolz, D., Hueglin, C., and Prévôt, A. S. H.: One decade of parallel fine (PM2.5) and coarse (PM10–PM2.5) particulate matter measurements in Europe: trends and variability, Atmos. Chem. Phys., 12, 3189-3203, doi:10.5194/acp-12-3189-2012, 2012.

Bigi, A., and Harrison, R. M.: Analysis of the air pollution climate at a central urban background site, Atmos. Env., 44, 2004-2012, 2010.

Bohnenstengel, S. I., Evans, S., Clark, P. A., and Belcher, S. E.: Simulations of the London urban heat island, Quart. J. Roy. Meteorol. Soc., 137, 1625-1640, doi:10.1002/qj.855, 2011.

Bohnenstengel, S. I., Hamilton, I., Davies, M., and Belcher, S. E.: Impact of anthropogenic heat emissions on London's temperatures, Quart. J. Roy. Meteorol. Soc., doi:10.1002/qj.2144, 2013.

Bohnenstengel, S. I., Belcher, S. E., Aiken, A., Allan, J. D., Allen, G., Bacak, A., Bannan, T. J., Barlow, J. F., Beddows, D. C. S., Bloss, W. J., Booth, A. M., Chemel, C., Coceal, O., Di Marco, C. F., Dubey, M. K., Faloon, K. H., Fleming, Z. L., Furger, M., Gietl, J. K., Graves, R. R., Green, D. C., Grimmond, C. S. B., Halios, C. H., Hamilton, J. F., Harrison, R. M., Heal, M. R., Heard, D. E., Helfter, C., Herndon, S. C., Holmes, R. E., Hopkins, J. R., Jones, A. M., Kelly, F. J., Kotthaus, S., Langford, B., Lee, J. D., Leigh, R. J., Lewis, A. C., Lidster, R. T., Lopez-Hilfiker, F. D., McQuaid, J. B., Mohr, C., Monks, P. S., Nemitz, E., Ng, N. L., Percival, C. J., Prévôt, A. S. H., Ricketts, H. M. A., Sokhi, R., Stone, D., Thornton, J. A., Tremper, A. H., Valach, A. C., Visser, S., Whalley, L. K., Williams, L. R., Xu, L., Young, D. E., and Zotter, P.: Meteorology, air quality, and health in London: The ClearfLo project, Bull. Am. Meteor. Soc., (online release), doi:10.1175/bams-d-12-00245.1, 2014.

Boogaard, H., Kos, G. P. A., Weijers, E. P., Janssen, N. A. H., Fischer, P. H., van der Zee, S. C., de Hartog, J. J., and Hoek, G.: Contrast in air pollution components between major streets and background locations: Particulate matter mass, black carbon, elemental composition, nitrogen oxide and ultrafine particle number, Atmos. Env., 45, 650-658, 2011.

Bukowiecki, N., Hill, M., Gehrig, R., Zwicky, C. N., Lienemann, P., Hegedus, F., Falkenberg, G., Weingartner, E., and Baltensperger, U.: Trace metals in ambient air: Hourly size-segregated mass concentrations determined by synchrotron-XRF, Environ. Sci. Technol., 39, 5754-5762, 2005.

Bukowiecki, N., Lienemann, P., Zwicky, C. N., Furger, M., Richard, A., Falkenberg, G., Rickers, K., Grolimund, D., Borca, C., Hill, M., Gehrig, R., and Baltensperger, U.: X-ray fluorescence spectrometry for high throughput analysis of atmospheric aerosol samples: The benefits of synchrotron X-rays, Spectrochim. Acta B, 63, 929-938, 2008.

Bukowiecki, N., Gehrig, R., Lienemann, P., Hill, M., Figi, R., Buchmann, B., Furger, M., Richard, A., Mohr, C., Weimer, S., Prevot, A. S. H., and Baltensperger, U.: PM10 emission factors of abrasion particles from road traffic, Schweizerische Eidgenossenschaft, 2009a.

Bukowiecki, N., Lienemann, P., Hill, M., Figi, R., Richard, A., Furger, M., Rickers, K., Falkenberg, G., Zhao, Y. J., Cliff, S. S., Prevot, A. S. H., Baltensperger, U., Buchmann, B., and Gehrig, R.: Real-world emission factors for antimony and other brake wear related trace elements: Size-segregated values for light and heavy duty vehicles, Environ. Sci. Technol., 43, 8072-8078, 2009b.

Bukowiecki, N., Richard, A., Furger, M., Weingartner, E., Aguirre, M., Huthwelker, T., Lienemann, P., Gehrig, R., and Baltensperger, U.: Deposition uniformity and particle size distribution of ambient aerosol collected with a rotating drum impactor, Aerosol Sci. Technol., 43, 891-901, 2009c.

Bukowiecki, N., Lienemann, P., Hill, M., Furger, M., Richard, A., Amato, F., Prevot, A. S. H., Baltensperger, U., Buchmann, B., and Gehrig, R.: PM10 emission factors for non-exhaust particles generated by road traffic in an urban street canyon and along a freeway in Switzerland, Atmos. Env., 44, 2330-2340, 2010.

Calzolai, G., Chiari, M., Lucarelli, F., Nava, S., and Portarena, S.: Proton induced gamma-ray emission yields for the analysis of light elements in aerosol samples in an external beam set-up, Nucl. Instrum. Methods Phys. Res. Sect. B-Beam Interact. Mater. Atoms, 268, 1540-1545, 2010.

Canonaco, F., Crippa, M., Slowik, J. G., Baltensperger, U., and Prevot, A. S. H.: SoFi, an IGOR-based interface for the efficient use of the generalized multilinear engine (ME-2) for the source apportionment: ME-2 application to aerosol mass spectrometer data, Atmos. Meas. Tech., 6, 3649-3661, doi:10.5194/amt-6-3649-2013, 2013.

Charron, A., and Harrison, R. M.: Fine (PM2.5) and coarse (PM2.5-10) particulate matter on a heavily trafficked London highway: Sources and processes, Environ. Sci. Technol., 39, 7768-7776, doi:10.1021/es050462i, 2005.

Charron, A., Harrison, R. M., and Quincey, P.: What are the sources and conditions responsible for exceedences of the 24 h PM10 limit value (50 µg m−3) at a heavily trafficked London site?, Atmos. Env., 41, 1960-1975, 2007.

Crippa, M., DeCarlo, P. F., Slowik, J. G., Mohr, C., Heringa, M. F., Chirico, R., Poulain, L., Freutel, F., Sciare, J., Cozic, J., Di Marco, C. F., Elsasser, M., Nicolas, J. B., Marchand, N., Abidi, E., Wiedensohler, A., Drewnick, F., Schneider, J., Borrmann, S., Nemitz, E., Zimmermann, R., Jaffrezo, J. L., Prévôt, A. S. H., and Baltensperger, U.: Wintertime aerosol chemical composition and source apportionment of the organic fraction in the metropolitan area of Paris, Atmos. Chem. Phys., 13, 961-981, doi:10.5194/acp-13-961-2013, 2013.

DeCarlo, P. F., Kimmel, J. R., Trimborn, A., Northway, M. J., Jayne, J. T., Aiken, A. C., Gonin, M., Fuhrer, K., Horvath, T., Docherty, K. S., Worsnop, D. R., and Jimenez, J. L.: Field-deployable, high-resolution, time-of-flight aerosol mass spectrometer, Anal. Chem., 78, 8281-8289, doi:10.1021/ac061249n, 2006.

Dockery, D. W., and Pope, C. A., III: Acute respiratory effects of particulate air pollution, in: Annual Review of Public Health, edited by: Omenn, G. S., Annual Review of Public Health, Annual Reviews Inc., P.O. Box 10139, 4139 El Camino Way, Palo Alto, California 94306, USA, 107-132, 1994.

Dore, C. J., Goodwin, J. W. L., Watterson, J. D., Murrels, T. P., Passant, N. R., Hobson, M. M., Haigh, K. E., Baggott, S. L., Pye, S. T., Coleman, P. J., and King, K. R.: UK Emissions of Air Pollutants 1970 to 2001, National Atmospheric Emissions Inventory, 2003.

Flechsig, U., Jaggi, A., Spielmann, S., Padmore, H. A., and MacDowell, A. A.: The optics beamline at the Swiss Light Source, Nucl. Instrum. Methods Phys. Res. Sect. A-Accel. Spectrom. Dect. Assoc. Equip., 609, 281-285, 2009.

Formenti, P., Prati, P., Zucchiatti, A., Lucarelli, F., and Mando, P. A.: Aerosol study in the town of Genova with a PIXE analysis, Nucl. Instrum. Methods Phys. Res. Sect. B-Beam Interact. Mater. Atoms, 113, 359-362, 1996.

Formenti, P., Nava, S., Prati, P., Chevaillier, S., Klaver, A., Lafon, S., Mazzei, F., Calzolai, G., and Chiari, M.: Self-attenuation artifacts and correction factors of light element measurements by X-ray analysis: Implication for mineral dust composition studies, J. Geophys. Res.-Atmos., 115, 8, doi:10.1029/2009jd012701, 2010.

Fowler, D., and Smith, R.: Spatial and temporal variability in the deposition of acidifying species in the UK between 1986 and 1997, Department of Environment, Food and Rural Affairs, 2000.

Franklin, M., Koutrakis, P., and Schwartz, J.: The role of particle composition on the association between PM2.5 and mortality, Epidemiology, 19, 680-689, doi:10.1097/ede.0b013e3181812bb7, 2008.

Freutel, F., Schneider, J., Drewnick, F., von der Weiden-Reinmüller, S. L., Crippa, M., Prévôt, A. S. H., Baltensperger, U., Poulain, L., Wiedensohler, A., Sciare, J., Sarda-Estève, R., Burkhart, J. F., Eckhardt, S., Stohl, A., Gros, V., Colomb, A., Michoud, V., Doussin, J. F., Borbon, A., Haeffelin, M., Morille, Y., Beekmann, M., and Borrmann, S.: Aerosol particle measurements at three stationary sites in the megacity of Paris during summer 2009: meteorology and air mass origin dominate aerosol particle composition and size distribution, Atmos. Chem. Phys., 13, 933-959, doi:10.5194/acp-13-933-2013, 2013.

Gotschi, T., Hazenkamp-Von Arxb, M. E., Heinrich, J., Bono, R., Burney, P., Forsberg, B., Jarvis, D., Maldonado, J., Norback, D., Stern, W. B., Sunyer, J., Toren, K., Verlato, G., Villani, S., and Kunzli, N.: Elemental composition and reflectance of ambient fine particles at 21 European locations, Atmos. Env., 39, 5947-5958, 2005.

Hammond, D. M., Dvonch, J. T., Keeler, G. J., Parker, E. A., Kamal, A. S., Barres, J. A., Yip, F. Y., and Brakefield-Caldwell, W.: Sources of ambient fine particulate matter at two community sites in Detroit, Michigan, Atmos. Env., 42, 720-732, 2008.

Harrison, R. M., and Jones, A. M.: Multisite study of particle number concentrations in urban air, Environ. Sci. Technol., 39, 6063-6070, doi:10.1021/es040541e, 2005.

Harrison, R. M., Yin, J., Mark, D., Stedman, J., Appleby, R. S., Booker, J., and Moorcroft, S.: Studies of the coarse particle (2.5–10 μm) component in UK urban atmospheres, Atmos. Env., 35, 3667-3679, 2001.

Harrison, R. M., Stedman, J., and Derwent, D.: New Directions: Why are PM10 concentrations in Europe not falling?, Atmos. Env., 42, 603-606, 2008.

Harrison, R. M., Beddows, D. C. S., and Dall'Osto, M.: PMF analysis of wide-range particle size spectra collected on a major highway, Environ. Sci. Technol., 45, 5522-5528, 2011.

Harrison, R. M., Dall'Osto, M., Beddows, D. C. S., Thorpe, A. J., Bloss, W. J., Allan, J. D., Coe, H., Dorsey, J. R., Gallagher, M., Martin, C., Whitehead, J., Williams, P. I., Jones, R. L., Langridge, J. M., Benton, A. K., Ball, S. M., Langford, B., Hewitt, C. N., Davison, B., Martin, D., Petersson, K. F., Henshaw, S. J., White, I. R., Shallcross, D. E., Barlow, J. F., Dunbar, T., Davies, F., Nemitz, E., Phillips, G. J., Helfter, C., Di Marco, C. F., and Smith, S.: Atmospheric chemistry and physics in the atmosphere of a developed megacity (London): an overview of the REPARTEE experiment and its conclusions, Atmos. Chem. Phys., 12, 3065-3114, 2012a.

Harrison, R. M., Jones, A. M., Gietl, J., Yin, J., and Green, D. C.: Estimation of the contributions of brake dust, tire wear, and resuspension to nonexhaust traffic particles derived from atmospheric measurements, Environ. Sci. Technol., 46, 6523-6529, doi:10.1021/es300894r, 2012b.

Harrison, R. M., Laxen, D., Moorcroft, S., and Laxen, K.: Processes affecting concentrations of fine particulate matter (PM2.5) in the UK atmosphere, Atmos. Env., 46, 115-124, 2012c.

Janssen, N. A. H., Van Mansom, D. F. M., Van Der Jagt, K., Harssema, H., and Hoek, G.: Mass concentration and elemental composition of airborne particulate matter at street and background locations, Atmos. Env., 31, 1185-1193, 1997.

Jones, A. M., Harrison, R. M., and Baker, J.: The wind speed dependence of the concentrations of airborne particulate matter and NOx, Atmos. Env., 44, 1682-1690, 2010.

Jones, A. R., Thomson, D. J., Hort, M., and Devenish, B.: The UK Met Office's next-generation atmospheric dispersion model, NAME III, Air Pollution Modeling and its Application XVII, edited by: Borrego, C., and Norman, A.-L., Springer, 2007.

Kelly, F. J., and Fussell, J. C.: Size, source and chemical composition as determinants of toxicity attributable to ambient particulate matter, Atmos. Env., 60, 504-526, 2012.

Lee, D. S., Garland, J. A., and Fox, A. A.: Atmospheric concentrations of trace elements in urban areas of the United Kingdom, Atmos. Env., 28, 2691-2713, 1994.

Lin, C. C., Chen, S. J., Huang, K. L., Hwang, W. I., Chang-Chien, G. P., and Lin, W. Y.: Characteristics of metals in nano/ultrafine/fine/coarse particles collected beside a heavily trafficked road, Environ. Sci. Technol., 39, 8113-8122, 2005.

Lucarelli, F., Mando, P. A., Nava, S., Valerio, M., Prati, P., and Zucchiatti, A.: Elemental composition of urban aerosol collected in Florence, Italy, Environ. Monit. Assess., 65, 165-173, 2000.

Maenhaut, W.: "Global Change" related and other atmospheric aerosol research at the University of Gent, and the role of PIXE therein, Nucl. Instrum. Methods Phys. Res. Sect. B-Beam Interact. Mater. Atoms, 109, 419-428, 1996.

Mavrogianni, A., Davies, M., Batty, M., Belcher, S. E., Bohnenstengel, S. I., Carruthers, D., Chalabi, Z., Croxford, B., Demanuele, C., Evans, S., Giridharan, R., Hacker, J. N., Hamilton, I., Hogg, C., Hunt, J., Kolokotroni, M., Martin, C., Milner, J., Rajapaksha, I., Ridley, I., Steadman, J. P., Stocker, J., Wilkinson, P., and Ye, Z.: The comfort, energy and health implications of London's urban heat island, Build Serv. Eng. Res. Technol., 32, 35-52, doi:10.1177/0143624410394530, 2011.

Mazzei, F., Lucarelli, F., Nava, S., Prati, P., Valli, G., and Vecchi, R.: A new methodological approach: The combined use of two-stage streaker samplers and optical particle counters for the characterization of airborne particulate matter, Atmos. Env., 41, 5525-5535, 2007.

Minguillón, M. C., Cirach, M., Hoek, G., Brunekreef, B., Tsai, M., de Hoogh, K., Jedynska, A., Kooter, I. M., Nieuwenhuijsen, M., and Querol, X.: Spatial variability of trace elements and sources for improved exposure assessment in Barcelona, Atmos. Env., 89, 268-281, 2014.

Moffet, R. C., Desyaterik, Y., Hopkins, R. J., Tivanski, A. V., Gilles, M. K., Wang, Y., Shutthanandan, V., Molina, L. T., Abraham, R. G., Johnson, K. S., Mugica, V., Molina, M. J., Laskin, A., and Prather, K. A.: Characterization of aerosols containing Zn, Pb, and Cl from an industrial region of Mexico City, Environ. Sci. Technol., 42, 7091-7097, 2008.

Mohr, C., Lopez-Hilfiker, F. D., Zotter, P., Prévôt, A. S. H., Xu, L., Ng, N. L., Herndon, S. C., Williams, L. R., Franklin, J. P., Zahniser, M. S., Worsnop, D. R., Knighton, W. B., Aiken, A. C., Gorkowski, K. J., Dubey, M. K., Allan, J. D., and Thornton, J. A.: Contribution of nitrated phenols to wood burning brown carbon light absorption in Detling, United Kingdom during winter time, Environ. Sci. Technol., 47, 6316-6324, doi:10.1021/es400683v, 2013.

Moreno, T., Karanasiou, A., Amato, F., Lucarelli, F., Nava, S., Calzolai, G., Chiari, M., Coz, E., Artinano, B., Lumbreras, J., Borge, R., Boldo, E., Linares, C., Alastuey, A., Querol, X., and Gibbons, W.: Daily and hourly sourcing of metallic and mineral dust in urban air contaminated by traffic and coal-burning emissions, Atmos. Env., 68, 33-44, doi:10.1016/j.atmosenv.2012.11.037, 2013.

Nolte, C. G., Bhave, P. V., Arnold, J. R., Dennis, R. L., Zhang, K. M., and Wexler, A. S.: Modeling urban and regional aerosols—Application of the CMAQ-UCD Aerosol Model to Tampa, a coastal urban site, Atmos. Env., 42, 3179-3191, 2008.

Paatero, P.: The multilinear engine—A table-driven, least squares program for solving multilinear problems, including the n-way parallel factor analysis model, J. Comput. Graph. Stat., 8, 854-888, doi:10.1080/10618600.1999.10474853, 1999.

Putaud, J. P., Van Dingenen, R., Alastuey, A., Bauer, H., Birmili, W., Cyrys, J., Flentje, H., Fuzzi, S., Gehrig, R., Hansson, H. C., Harrison, R. M., Herrmann, H., Hitzenberger, R., Hüglin, C., Jones, A. M., Kasper-Giebl, A., Kiss, G., Kousa, A., Kuhlbusch, T. A. J., Löschau, G., Maenhaut, W., Molnar, A., Moreno, T., Pekkanen, J., Perrino, C., Pitz, M., Puxbaum, H., Querol, X., Rodriguez, S., Salma, I., Schwarz, J., Smolik, J., Schneider, J., Spindler, G., ten Brink, H., Tursic, J., Viana, M., Wiedensohler, A., and Raes, F.: A European aerosol phenomenology – 3: Physical and chemical characteristics of particulate matter from 60 rural, urban, and kerbside sites across Europe, Atmos. Env., 44, 1308-1320, 2010.

Querol, X., Viana, M., Alastuey, A., Amato, F., Moreno, T., Castillo, S., Pey, J., de la Rosa, J., Sánchez de la Campa, A., Artíñano, B., Salvador, P., García Dos Santos, S., Fernández-Patier, R., Moreno-Grau, S., Negral, L., Minguillón, M. C., Monfort, E., Gil, J. I., Inza, A., Ortega, L. A., Santamaría, J. M., and Zabalza, J.: Source origin of trace elements in PM from regional background, urban and industrial sites of Spain, Atmos. Env., 41, 7219-7231, 2007.

Reche, C., Moreno, T., Amato, F., Viana, M., van Drooge, B. L., Chuang, H.-C., Bérubé, K., Jones, T., Alastuey, A., and Querol, X.: A multidisciplinary approach to characterise exposure risk and toxicological effects of PM10 and PM2.5 samples in urban environments, Ecotox. Environ. Safe., 78, 327-335, 2012.

Richard, A., Bukowiecki, N., Lienemann, P., Furger, M., Fierz, M., Minguillon, M. C., Weideli, B., Figi, R., Flechsig, U., Appel, K., Prevot, A. S. H., and Baltensperger, U.: Quantitative sampling and analysis of trace elements in atmospheric aerosols: impactor characterization and synchrotron-XRF mass calibration, Atmos. Meas. Tech., 3, 1473-1485, 2010.

Richard, A., Gianini, M. F. D., Mohr, C., Furger, M., Bukowiecki, N., Minguillon, M. C., Lienemann, P., Flechsig, U., Appel, K., DeCarlo, P. F., Heringa, M. F., Chirico, R., Baltensperger, U., and Prevot, A. S. H.: Source apportionment of size and time resolved trace elements and organic aerosols from an urban courtyard site in Switzerland, Atmos. Chem. Phys., 11, 8945-8963, 2011.

Salcedo, D., Laskin, A., Shutthanandan, V., and Jimenez, J. L.: Feasibility of the detection of trace elements in particulate matter using online high-resolution aerosol mass spectrometry, Aerosol Sci. Technol., 46, 1187-1200, doi:10.1080/02786826.2012.701354, 2012.

Theodosi, C., Grivas, G., Zarmpas, P., Chaloulakou, A., and Mihalopoulos, N.: Mass and chemical composition of size-segregated aerosols (PM1, PM2.5, PM10) over Athens, Greece: local versus regional sources, Atmos. Chem. Phys., 11, 11895-11911, doi:10.5194/acp-11-11895-2011, 2011.

Turoczi, B., Hoffer, A., Toth, A., Kovats, N., Acs, A., Ferincz, A., Kovacs, A., and Gelencser, A.: Comparative assessment of ecotoxicity of urban aerosol, Atmos. Chem. Phys., 12, 7365-7370, doi:10.5194/acp-12-7365-2012, 2012.

Viana, M., Kuhlbusch, T. A. J., Querol, X., Alastuey, A., Harrison, R. M., Hopke, P. K., Winiwarter, W., Vallius, A., Szidat, S., Prevot, A. S. H., Hueglin, C., Bloemen, H., Wahlin, P., Vecchi, R., Miranda, A. I., Kasper-Giebl, A., Maenhaut, W., and Hitzenberger, R.: Source apportionment of particulate matter in Europe: A review of methods and results, J. Aerosol Sci., 39, 827-849, doi:10.1016/j.jaerosci.2008.05.007, 2008.

Wedepohl, K.: The composition of the continental crust, Geochim. Cosmochim. Ac., 59, 1217-1232, doi:10.1016/0016-7037(95)00038-2, 1995.

Weijers, E. P., Schaap, M., Nguyen, L., Matthijsen, J., van der Gon, H., ten Brink, H. M., and Hoogerbrugge, R.: Anthropogenic and natural constituents in particulate matter in the Netherlands, Atmos. Chem. Phys., 11, 2281-2294, doi:10.5194/acp-11-2281-2011, 2011.

Witt, M. L. I., Meheran, N., Mather, T. A., de Hoog, J. C. M., and Pyle, D. M.: Aerosol trace metals, particle morphology and total gaseous mercury in the atmosphere of Oxford, UK, Atmos. Env., 44, 1524-1538, doi:10.1016/j.atmosenv.2010.01.008, 2010.

Wood, C. R., Lacser, A., Barlow, J. F., Padhra, A., Belcher, S. E., Nemitz, E., Helfter, C., Famulari, D., and Grimmond, C. S. B.: Turbulent flow at 190 m height above London during 2006-2008: A climatology and the applicability of similarity theory, Bound.-Layer Meteor., 137, 77-96, doi:10.1007/s10546-010-9516-x, 2010.

Xiao, Z. H., Shao, L. Y., Zhang, N., Wang, J., and Wang, J. Y.: Heavy metal compositions and bioreactivity of airborne PM10 in a valley-shaped city in northwestern China, Aerosol Air Qual. Res., 13, 1116-1125, doi:10.4209/aaqr.2012.10.0287, 2013.

Zhou, J. A., Ito, K., Lall, R., Lippmann, M., and Thurston, G.: Time-series analysis of mortality effects of fine particulate matter components in Detroit and Seattle, Environ. Health Perspect., 119, 461-466, doi:10.1289/ehp.1002613, 2011.

Zhou, Y., and Levy, J. I.: The impact of urban street canyons on population exposure to traffic-related primary pollutants, Atmos. Env., 42, 3087-3098, 2008.

Tables

Table 1. Measurement campaign details.

Site	Start/End date	Site type	Sampling time	Inlet height	Sampling platform
MR	11 Jan – 14 Feb 2012	kerbside	2 h	4 m	container at 1 m from road
NK	11 Jan – 9 Feb 2012	urban background	2 h	4 m	container
DE	17 Jan – 13 Feb 2012	rural	2 h	1.5 m	grass field

Table 2. Self-absorption correction factors.

	Calibration standard 1		Calibration standard 2		$PM_{10-2.5}$ sample		$PM_{2.5-1.0}$ sample				
Particle size (µm)[a]	9.0		9.0		5.0		1.6				
Density (g cm-3)[b]	2.19		2.27		2.00		2.00		Total correction factor[d]		
	AF[c]	*a*[c]	AF[c]	*a*[c]	AF[c]	*a*[c]	AF[c]	*a*[c]	$PM_{10-2.5}$ sample	$PM_{2.5-1.0}$ sample	$PM_{1.0-0.3}$ sample
Na	0.22	0.49			0.43	0.40	0.74	0.40	0.52	0.30	0.22
Mg			0.32	0.33	0.58	0.25	0.83	0.25	0.55	0.38	0.32
Al	0.43	0.23			0.70	0.15	0.89	0.15	0.61	0.48	0.43
Si			0.51	0.17	0.79	0.10	0.93	0.10	0.64	0.55	0.51
P	0.60	0.13			0.85	0.07	0.95	0.07	0.70	0.63	0.60
S			0.65	0.10	0.90	0.04	0.97	0.04	0.72	0.67	0.65
Cl	0.71	0.08			0.88	0.05	0.96	0.05	0.80	0.73	0.71
K			0.79	0.05	0.94	0.03	0.98	0.03	0.84	0.81	0.79
Ca	0.82	0.05	0.76	0.06	0.95	0.02	0.98	0.02	0.87[e]	0.84[e]	0.82[e]

[a] Particle size given as geometric mean diameter.

[b] Average density of the calibration standards and of ambient aerosol. The composition of calibration standard 1 is $Na_{3.76}Al_{3.76}P_{3.76}Cl_{3.76}Ca_{3.76}CoN_{8}O_{24}$, of calibration standard 2 $Mg_{3.76}Si_{3.76}S_{3.76}K_{3.76}Ca_{3.76}CoN_{7}O_{21}$, and of ambient samples $C_{39}H_{29}N_{10}O_{18}S_{3}Fe$.

[c] Attenuation factors and *a* (μm^{-1}; $a = 2/3*\mu*\rho$ with μ the mass attenuation coefficient ($cm^{2}\ g^{-1}$) and ρ the particle mass density ($g\ cm^{-3}$)) according to Eq. (4) in Formenti et al. (2010).

[d] Total correction factor defined as ratios AF calibration standard / AF sample. Self-absorption effects are neglected in the $PM_{1.0-0.3}$ samples; therefore these samples are only corrected for AF calibration standards.

[e] Ca is corrected based on the average AF of calibration standards 1 and 2, and a calibration standard used to calibrate the elements Ti to Zn at SLS (Ca present in all three standards). Data for this third calibration standard are: particle size of 7.0 ± 2 µm, average density of 2.37 $g\ cm^{-3}$ and AF and *a* for Ca of 0.89 and 0.03 μm^{-1}, respectively.

~~**Table 2.** Self-absorption correction factors.~~

	~~Geometric mean diameter (µm)~~	~~Density[a] (g cm-3)~~	~~Na[b]~~	~~Mg[b]~~	~~Al[b]~~	~~Si[b]~~
~~Calibration standard 1~~	~~9~~	~~2.19~~	~~0.22~~ ~~*0.49*~~		~~0.43~~ ~~*0.23*~~	
~~Calibration standard 2~~	~~9~~	~~2.27~~		~~0.32~~ ~~*0.33*~~		~~0.51~~ ~~*0.17*~~
~~$PM_{10-2.5}$ sample~~	~~5~~	~~2.00~~	~~0.43~~ ~~*0.40*~~	~~0.58~~ ~~*0.25*~~	~~0.70~~ ~~*0.15*~~	~~0.79~~ ~~*0.10*~~
~~$PM_{2.5-1.0}$ sample~~	~~1.6~~	~~2.00~~	~~0.74~~ ~~*0.40*~~	~~0.83~~ ~~*0.25*~~	~~0.89~~ ~~*0.15*~~	~~0.93~~ ~~*0.10*~~

~~[a] Average density of the calibration standards and of ambient aerosol. The composition of calibration standard 1 is $Na_{3.76}Al_{3.76}P_{3.76}Cl_{3.76}Ca_{3.76}CoN_{8}O_{24}$, of calibration standard 2 $Mg_{3.76}Si_{3.76}S_{3.76}K_{3.76}Ca_{3.76}CoN_{7}O_{21}$, and of ambient samples $C_{39}H_{29}N_{10}O_{18}S_{3}Fe$.~~

~~[b] Attenuation factors and *a* (italic values, μm^{-1}; $a = 2/3*\mu*\rho$ with μ the mass attenuation coefficient ($cm^{2}\ g^{-1}$) and ρ the particle mass density ($g\ cm^{-3}$)) according to Eq. (4) in Formenti et al. (2010).~~

Table 3. Mean, median and 25-75th percentile trace element concentrations (ng m^{-3}) for $PM_{10-2.5}$, $PM_{2.5-1.0}$ and $PM_{1.0-0.3}$ at MR, NK and DE.

Marylebone Road

Element	**$PM_{10-2.5}$**				**$PM_{2.5-1.0}$**				**$PM_{1.0-0.3}$**			
	mean	**median**	**25th perc**	**75th perc**	**mean**	**median**	**25th perc**	**75th perc**	**mean**	**median**	**25th perc**	**75th perc**
Na	913.7	854.2	447.9	1301.6	121.6	85.2	53.6	159.1	27.5	15.9	10.7	28.0
Mg	104.5	95.6	65.6	135.4	25.3	19.6	13.5	34.3	8.3	7.0	4.9	9.6
Al	82.4	66.5	44.9	102.7	23.1	20.7	15.4	28.3	5.8	5.4	3.6	7.2
Si	190.0	147.0	89.9	244.3	54.8	43.7	25.3	70.7	14.9	12.3	7.4	19.0
P	11.4	10.1	6.9	14.6	4.2	3.8	2.4	5.6	2.9	2.2	1.5	3.9
S	90.2	80.0	56.8	111.3	43.1	36.0	25.7	54.4	127.1	53.8	24.3	185.2
Cl	790.6	689.4	292.7	1164.4	217.4	110.0	30.6	329.1	81.2	25.2	5.1	103.4
K	36.2	32.4	23.1	44.0	13.1	11.3	7.6	17.4	14.1	9.4	6.3	18.4
Ca	201.9	152.4	93.6	265.6	62.0	43.9	26.7	79.3	16.7	12.3	7.4	20.7
Ti	7.5	5.9	3.4	10.0	2.6	2.0	1.2	3.6	0.8	0.7	0.4	1.1
V	2.2	1.9	1.1	2.9	0.9	0.8	0.4	1.1	0.4	0.4	0.2	0.6
Cr	6.3	3.6	2.0	6.0	1.7	1.4	0.9	2.4	0.6	0.4	0.3	0.7
Mn	9.4	7.7	4.6	12.2	3.4	2.9	2.0	4.4	1.4	1.0	0.6	1.7
Fe	693.1	601.7	347.0	929.9	259.9	226.8	136.4	348.6	90.4	75.8	43.6	122.3
Ni	2.1	0.6	0.4	1.0	0.3	0.2	0.1	0.4	0.2	0.1	0.1	0.2
Cu	26.0	22.9	12.6	33.3	9.5	8.2	4.6	12.5	3.3	2.6	1.4	4.5
Zn	10.9	8.9	5.2	14.1	4.3	3.6	2.0	5.6	4.6	3.0	1.6	6.5
Br	2.3	1.8	1.0	3.0	0.8	0.6	0.4	1.0	1.7	1.1	0.6	2.3
Sr	1.1	0.9	0.7	1.4	0.4	0.4	0.2	0.6	0.2	0.1	0.1	0.2
Zr	2.5	1.8	0.9	3.3	1.1	0.8	0.4	1.4	0.4	0.2	0.1	0.5
Mo	3.1	2.2	1.1	3.9	1.3	1.0	0.6	1.6	0.5	0.4	0.2	0.6
Sn	4.1	3.3	1.9	5.5	1.7	1.5	0.8	2.3	0.7	0.6	0.3	1.0
Sb	3.3	2.5	1.3	4.4	1.3	1.0	0.6	1.8	0.5	0.4	0.3	0.7
Ba	18.3	14.5	8.3	24.7	7.6	6.5	3.9	10.3	2.7	2.1	1.2	3.7
Pb	1.6	0.9	0.6	1.7	0.7	0.5	0.3	0.9	1.6	0.8	0.4	2.1

North Kensington

Element	$PM_{10-2.5}$				$PM_{2.5-1.0}$				$PM_{1.0-0.3}$			
	mean	median	25th perc	75th perc	mean	median	25th perc	75th perc	mean	median	25th perc	75th perc
Na	595.1	511.6	269.6	897.9	123.5	87.1	56.4	163.7	28.6	14.2	9.8	31.7
Mg	57.2	49.9	30.2	83.9	23.0	17.9	12.7	30.8	7.1	5.2	3.1	8.8
Al	30.8	26.0	16.3	40.8	17.1	15.5	10.2	20.7	4.4	3.8	2.7	5.4
Si	63.1	51.2	25.6	78.7	33.1	26.5	14.7	45.0	8.3	5.9	3.5	10.2
P	4.5	4.0	2.3	6.3	2.7	2.3	1.4	3.3	1.9	1.4	0.8	2.4
S	45.8	40.7	27.5	61.7	36.1	28.8	20.3	44.2	113.3	53.1	24.6	137.0
Cl	435.6	343.1	110.6	702.3	199.2	79.1	18.2	289.8	63.7	9.9	2.5	66.6
K	18.9	16.7	10.8	25.9	11.5	9.9	6.7	16.1	12.2	8.1	4.9	14.8
Ca	79.9	60.7	35.0	99.0	41.7	31.1	17.5	50.1	9.7	7.1	4.0	11.6
Ti	2.7	1.7	0.9	3.2	1.6	1.2	0.5	2.3	0.4	0.3	0.1	0.5
V	0.6	0.4	0.2	0.7	0.4	0.3	0.1	0.5	0.2	0.2	0.1	0.3
Cr	1.2	0.8	0.4	1.5	0.6	0.5	0.3	0.8	0.2	0.1	0.0	0.2
Mn	2.4	1.7	1.0	3.0	1.7	1.5	0.8	2.2	0.8	0.5	0.1	0.9
Fe	163.8	120.8	69.9	202.6	98.8	72.7	39.0	126.0	30.1	18.5	9.6	34.8
Ni	0.4	0.2	0.1	0.4	0.1	0.1	0.0	0.2	0.1	0.1	0.0	0.1
Cu	4.9	3.6	1.8	6.4	3.7	2.5	1.4	4.6	1.2	0.6	0.4	1.4
Zn	2.9	1.9	1.0	3.4	2.1	1.5	0.8	2.8	3.2	1.9	0.8	4.3
Br	1.3	1.0	0.4	1.8	0.7	0.5	0.3	1.0	1.6	1.1	0.5	1.9
Sr	0.5	0.4	0.2	0.6	0.3	0.2	0.2	0.4	0.1	0.1	0.0	0.1
Zr	0.5	0.2	0.1	0.4	0.3	0.2	0.1	0.4	0.1	0.1	0.0	0.1
Mo	0.8	0.3	0.2	0.7	0.5	0.3	0.1	0.6	0.2	0.1	0.1	0.2
Sn	0.7	0.5	0.2	0.9	0.5	0.4	0.2	0.7	0.3	0.2	0.1	0.3
Sb	0.5	0.3	0.2	0.6	0.4	0.2	0.1	0.5	0.2	0.2	0.1	0.3
Ba	4.3	2.1	1.2	4.5	2.7	1.8	0.9	3.5	1.0	0.6	0.3	1.2
Pb	0.4	0.2	0.1	0.4	0.4	0.2	0.1	0.6	1.4	0.7	0.3	1.8

Detling												
Element	**$PM_{10-2.5}$**				**$PM_{2.5-1.0}$**				**$PM_{1.0-0.3}$**			
	mean	**median**	**25th perc**	**75th perc**	**mean**	**median**	**25th perc**	**75th perc**	**mean**	**median**	**25th perc**	**75th perc**
Na	271.9	194.7	17.2	437.0	66.2	37.2	13.0	82.2	21.3	11.4	5.0	28.3
Mg	27.5	20.8	5.2	39.9	12.4	8.8	2.7	17.1	6.2	4.4	1.6	7.7
Al	15.6	14.4	7.4	21.5	13.4	12.9	6.7	18.4	3.2	3.1	1.5	4.7
Si	32.5	26.3	13.8	41.5	17.3	13.7	6.1	25.3	5.5	4.3	2.4	7.9
P	2.2	1.8	0.8	2.9	1.3	1.0	0.5	1.7	1.9	1.0	0.5	2.4
S	26.1	22.8	4.9	34.6	22.3	20.4	8.8	32.1	145.2	38.8	18.0	157.4
Cl	189.6	40.5	2.9	303.7	99.1	6.8	1.9	109.0	45.4	7.3	2.4	40.4
K	11.7	10.0	2.9	14.9	6.6	6.1	2.1	10.1	15.7	6.4	2.9	15.6
Ca	32.5	24.9	9.6	40.3	16.7	12.3	4.9	21.0	6.7	4.1	2.2	6.8
Ti	1.0	0.6	0.3	1.3	0.7	0.4	0.2	1.0	0.2	0.2	0.1	0.3
V	0.2	0.1	0.1	0.2	0.1	0.1	0.1	0.2	0.2	0.1	0.0	0.3
Cr	4.0	0.9	0.3	2.9	0.8	0.3	0.2	0.6	0.1	0.1	0.0	0.2
Mn	1.8	0.6	0.3	1.3	1.1	1.2	0.3	1.6	0.7	0.3	0.0	0.7
Fe	55.2	36.8	19.9	66.2	26.8	21.5	11.5	37.7	9.8	7.8	4.3	13.3
Ni	4.3	0.7	0.2	2.6	0.6	0.1	0.1	0.3	0.9	0.1	0.0	0.5
Cu	1.4	0.8	0.4	1.8	0.9	0.7	0.4	1.1	0.7	0.3	0.1	0.5
Zn	3.4	0.9	0.4	1.8	1.3	0.7	0.3	1.7	4.3	1.6	0.6	5.7
Br	1.1	0.4	0.1	1.3	0.4	0.2	0.1	0.5	1.9	1.1	0.5	2.4
Sr	0.2	0.2	0.1	0.3	0.1	0.1	0.0	0.2	0.1	0.0	0.0	0.1
Zr	0.0	0.0	-0.1	0.1	0.1	0.0	0.0	0.1	0.0	0.0	0.0	0.0
Mo	1.9	0.1	0.1	0.7	0.2	0.1	0.0	0.2	0.1	0.1	0.0	0.1
Sn	0.3	0.1	0.0	0.2	0.2	0.1	0.1	0.2	0.2	0.1	0.1	0.3
Sb	0.2	0.1	0.0	0.2	0.1	0.1	0.0	0.1	0.2	0.1	0.0	0.2
Ba	1.0	0.4	0.2	0.8	0.5	0.4	0.2	0.7	0.3	0.2	0.1	0.4
Pb	0.3	0.1	0.0	0.3	0.3	0.1	0.1	0.5	1.6	0.5	0.2	1.8

Figure captions

Figure 1. Map of south eastern UK. Indicated are the sampling sites MR (kerbside site Marylebone Road), NK (urban background site North Kensington), DE (rural site Detling), and the elevated BT Tower site for meteorological measurements (adapted from Google Maps).

Figure 2. Relative contribution for trace elements in $PM_{10-2.5}$, $PM_{2.5-1.0}$ and $PM_{1.0-0.3}$ to total PM_{10} mean concentration per element at MR (top), NK (middle) and DE (bottom). Absolute mean total PM_{10} element concentrations are shown above each bar.

Figure 3. Mean, median and 25-75th percentile urban increment values for trace elements at NK relative to DE for $PM_{10-2.5}$ (top), $PM_{2.5-1.0}$ (middle) and $PM_{1.0-0.3}$ (bottom). Note that the median of Zr in $PM_{10-2.5}$ is below detection limit.

Figure 4. Mean, median and 25-75th percentile trace element concentrations at MR split in four wind direction sectors (N, E, S, W) normalized to the global median concentration per element for $PM_{10-2.5}$ (top), $PM_{2.5-1.0}$ (middle) and $PM_{1.0-0.3}$ (bottom). See Sect. 4.2.2 for the definition of the wind direction sectors.

Figure 5. Mean, median and 25-75th percentile kerb increment values for trace elements at MR relative to NK for $PM_{10-2.5}$ (top), $PM_{2.5-1.0}$ (middle) and $PM_{1.0-0.3}$ (bottom) split in SW and NE wind sectors. See Sect. 4.2.2 for the definition of the wind direction sectors.

Figure 6. Diurnal cycles of 2 h median concentrations of Na, Si, S, Fe and Sb for $PM_{10-2.5}$ (left), $PM_{2.5-1.0}$ (middle) and $PM_{1.0-0.3}$ (right) at MR, NK, DE split in SW and NE wind sectors. See Sect. 4.2.2 for the definition of the wind direction sectors. Hour of day is start of 2 h sampling period, so 00:00 LT means sampling from 00:00 to 02:00 LT.

Figure 7. Weekly cycles of 2 h median concentrations of Na, Si, S, Fe and Sb for $PM_{10-2.5}$ (left), $PM_{2.5-1.0}$ (middle) and $PM_{1.0-0.3}$ (right) at MR, NK, DE.

Figure 8. (top) Diurnal (left) and weekly (right) cycles of traffic flow at MR, (middle and bottom left) diurnal cycles of 2 h median NO_x and total PM_{10} mass concentrations at MR, NK and DE split in SW and NE wind sectors, and (middle and bottom right) weekly cycles of 2 h median NO_x and total PM_{10} mass concentrations at MR, NK and DE. See Sect. 4.2.2 for the definition of the wind direction sectors. Time stamp is start of 2 h averaging period, so 00:00 LT means averaging between 00:00 and 02:00 LT.

Figure 9. (top panel) Time series of (top left axis) $PM_{1.0\text{-}0.3}$ S, K, Zn and Pb concentrations at NK and (top right axis) wind direction from BT Tower, time series of (bottom left axis) $PM_{10\text{-}2.5}$ Na, Si, S and Sb concentrations at NK and (bottom right axis) total PM_{10} mass concentration at NK; (bottom panel) three NK footprints simulated with the NAME model corresponding to the vertical lines (A, B, C) indicated in the top panel. Trajectories are simulated for particles released from NK and followed back at 0-100 m a.g.l. for the previous 24 h at: **(A)** 23 January 2012 09:00 LT, **(B)** 31 January 2012 21:00 LT, **(C)** 6 February 2012 18:00 LT; particle concentrations increase from blue to red.

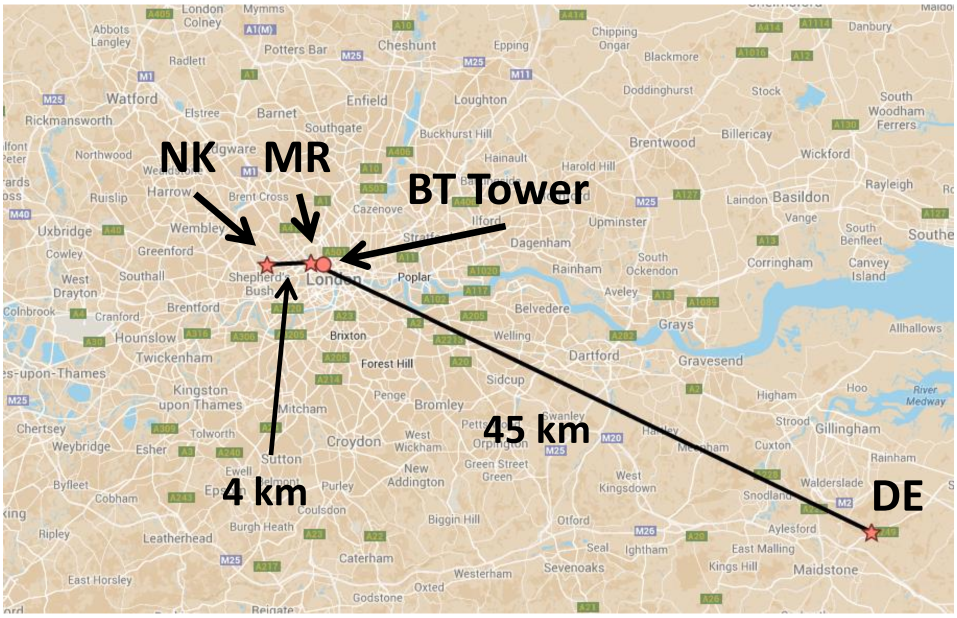

Figure 1. Map of south eastern UK. Indicated are the sampling sites MR (kerbside site Marylebone Road), NK (urban background site North Kensington), DE (rural site Detling), and the elevated BT Tower site for meteorological measurements (adapted from Google Maps).

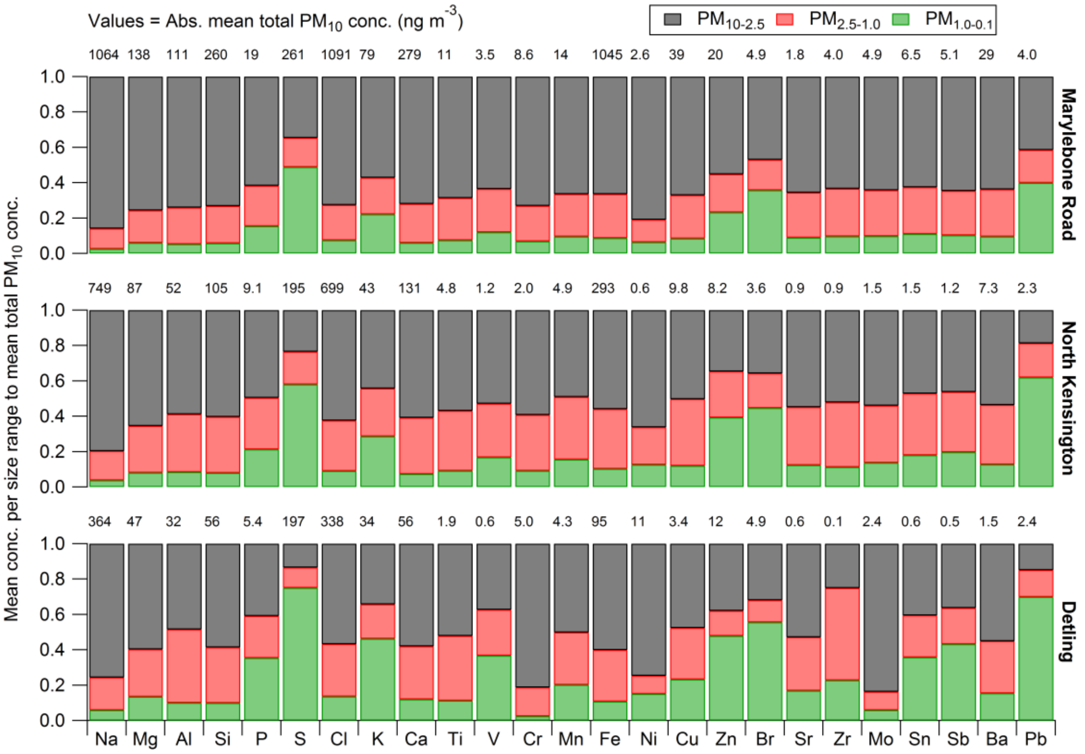

Figure 2. Relative contribution for trace elements in $PM_{10-2.5}$, $PM_{2.5-1.0}$ and $PM_{1.0-0.3}$ to total PM_{10} mean concentration per element at MR (top), NK (middle) and DE (bottom). Absolute mean total PM_{10} element concentrations are shown above each bar.

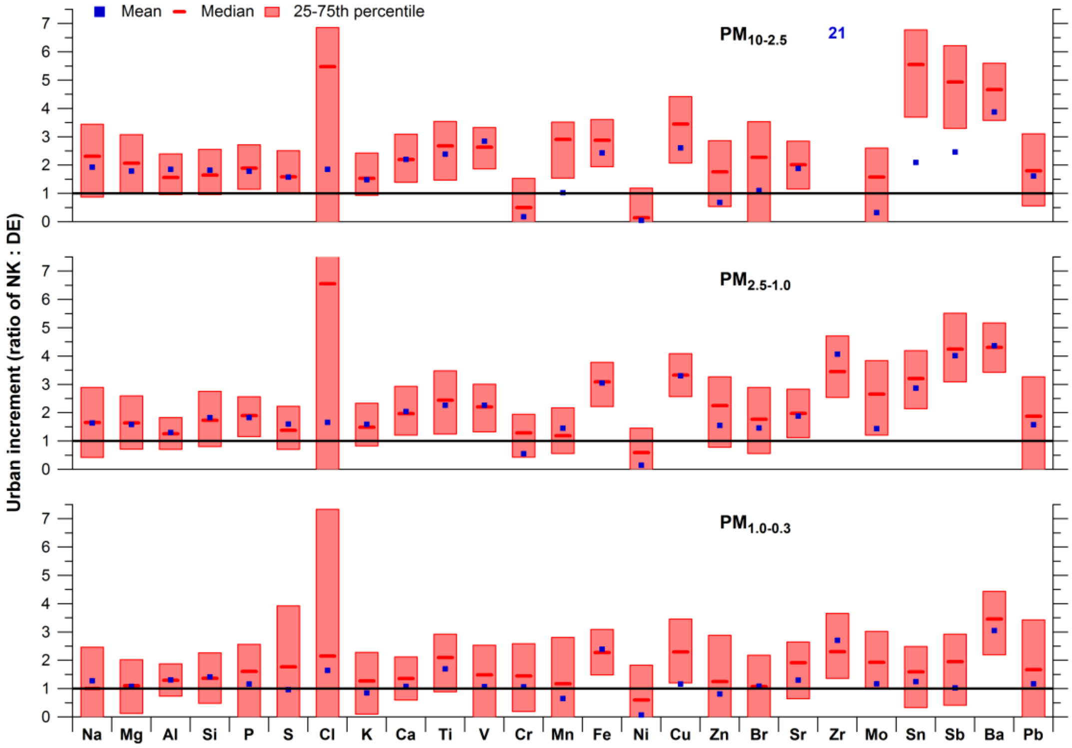

Figure 3. Mean, median and 25-75th percentile urban increment values for trace elements at NK relative to DE for $PM_{10-2.5}$ (top), $PM_{2.5-1.0}$ (middle) and $PM_{1.0-0.3}$ (bottom). Note that the median of Zr in $PM_{10-2.5}$ is below detection limit.

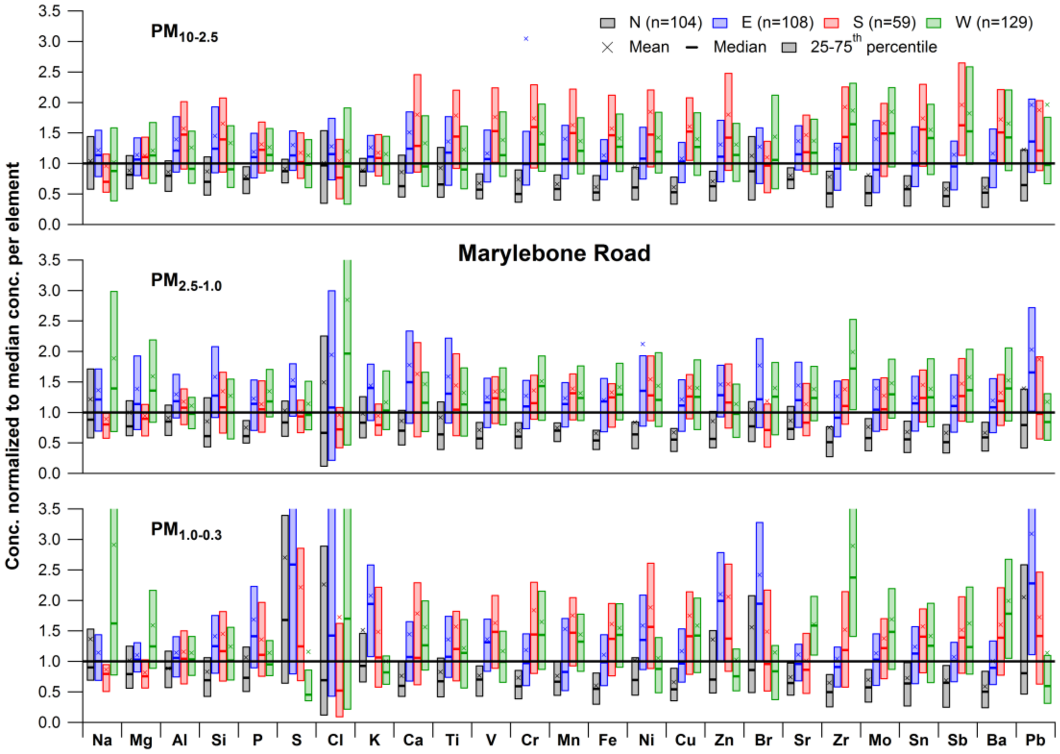

Figure 4. Mean, median and 25-75th percentile trace element concentrations at MR split in four wind direction sectors (N, E, S, W) normalized to the global median concentration per element for $PM_{10-2.5}$ (top), $PM_{2.5-1.0}$ (middle) and $PM_{1.0-0.3}$ (bottom). See Sect. 4.2.2 for the definition of the wind direction sectors.

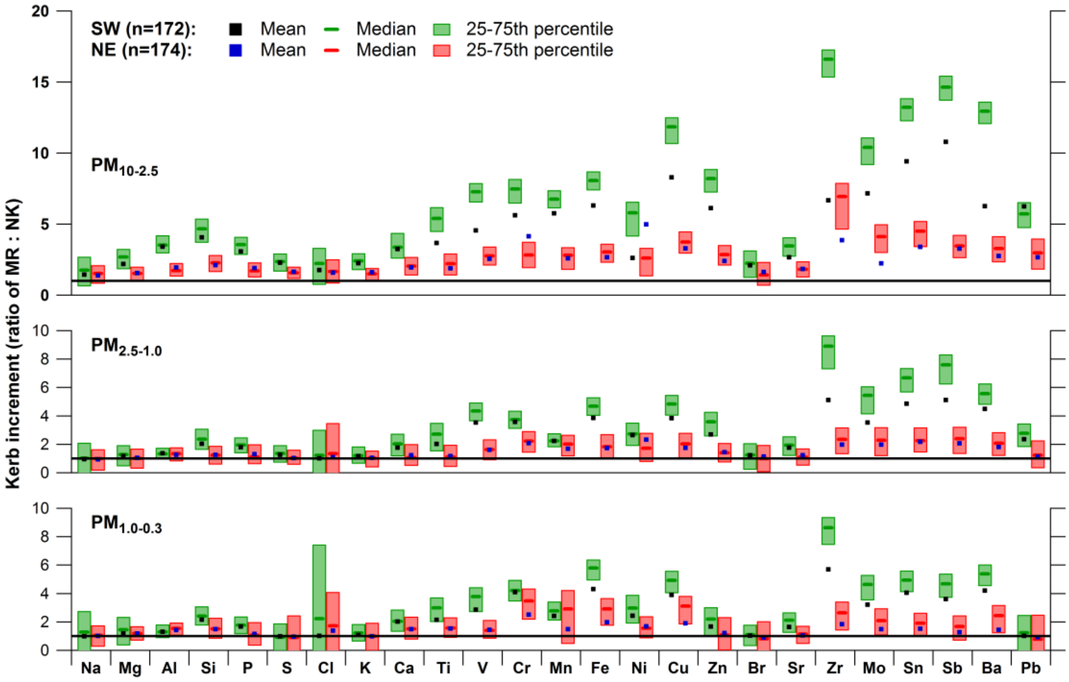

Figure 5. Mean, median and 25-75th percentile kerb increment values for trace elements at MR relative to NK for $PM_{10\text{-}2.5}$ (top), $PM_{2.5\text{-}1.0}$ (middle) and $PM_{1.0\text{-}0.3}$ (bottom) split in SW and NE wind sectors. See Sect. 4.2.2 for the definition of the wind direction sectors.

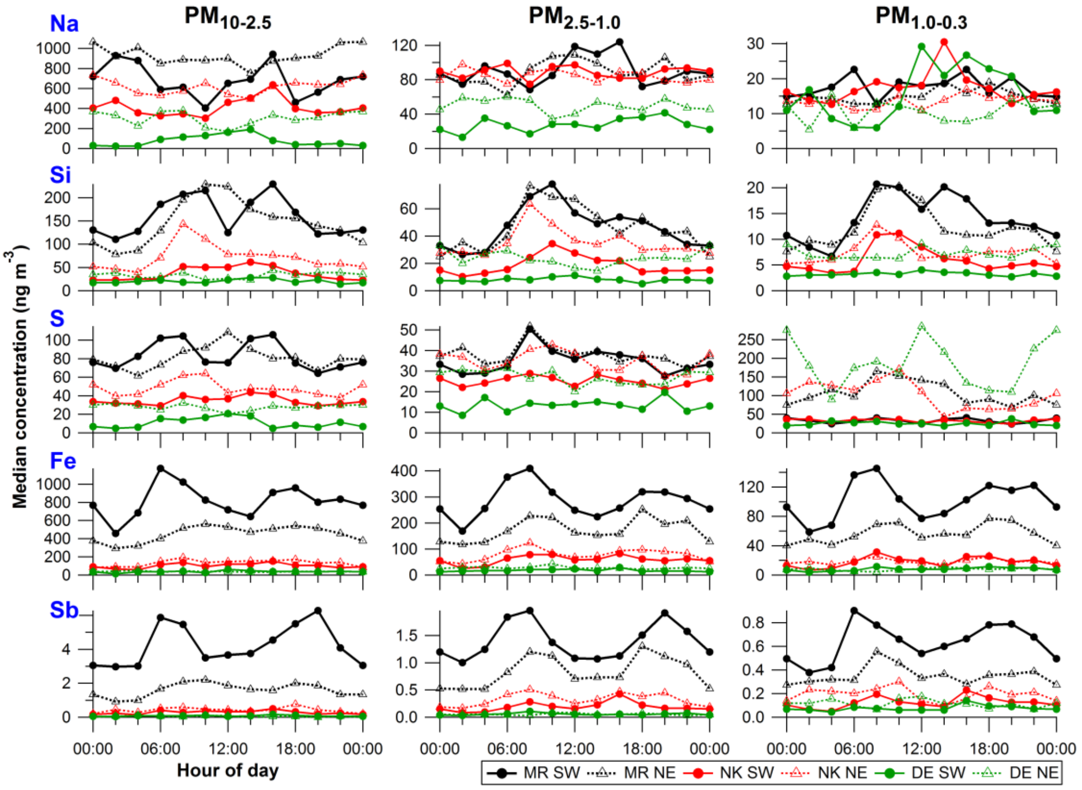

Figure 6. Diurnal cycles of 2 h median concentrations of Na, Si, S, Fe and Sb for $PM_{10\text{-}2.5}$ (left), $PM_{2.5\text{-}1.0}$ (middle) and $PM_{1.0\text{-}0.3}$ (right) at MR, NK, DE split in SW and NE wind sectors. See Sect. 4.2.2 for the definition of the wind direction sectors. Hour of day is start of 2 h sampling period, so 00:00 LT means sampling from 00:00 to 02:00 LT.

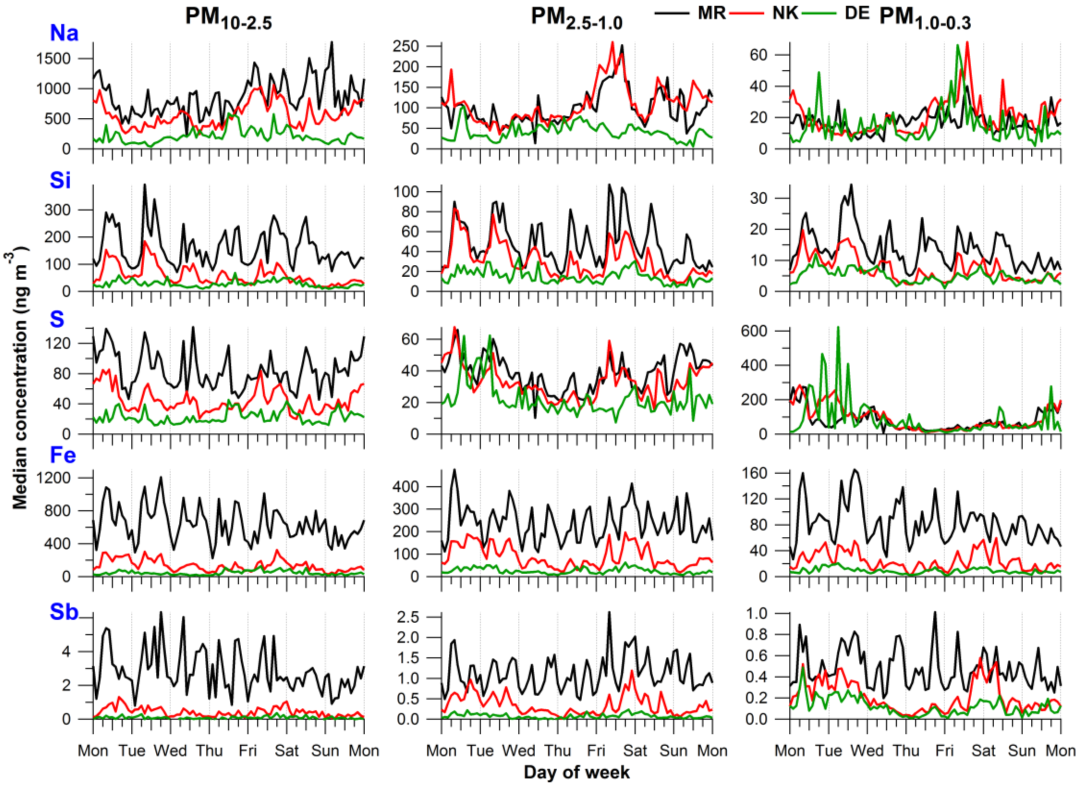

Figure 7. Weekly cycles of 2 h median concentrations of Na, Si, S, Fe and Sb for $PM_{10-2.5}$ (left), $PM_{2.5-1.0}$ (middle) and $PM_{1.0-0.3}$ (right) at MR, NK, DE.

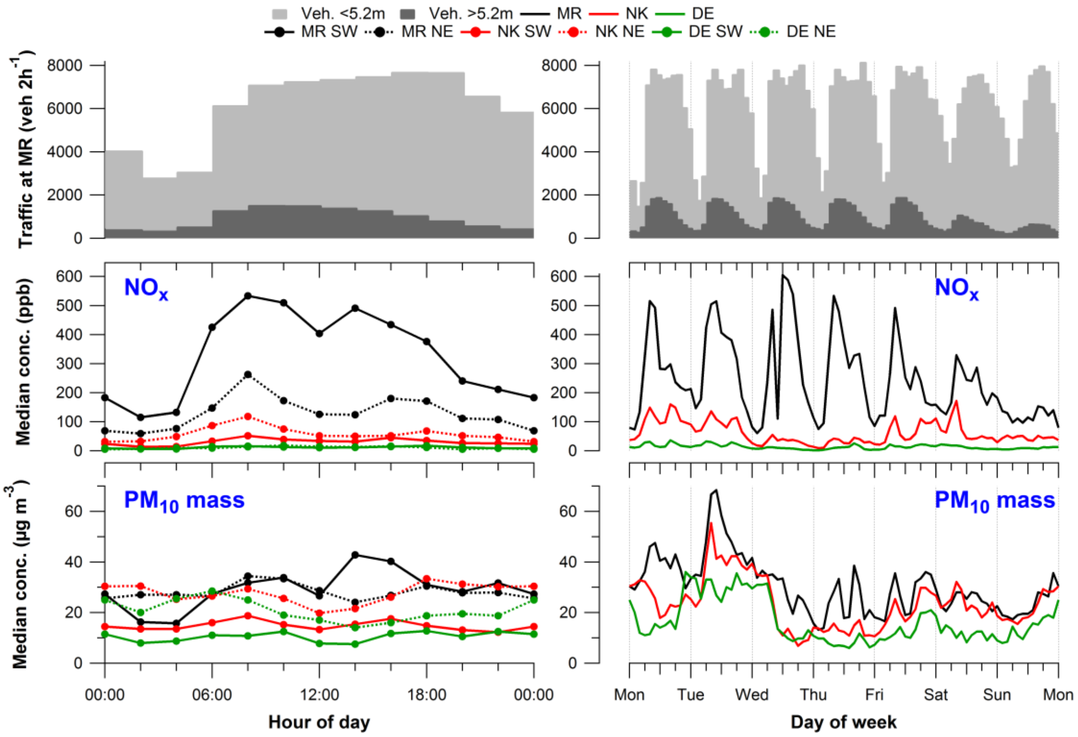

Figure 8. (top) Diurnal (left) and weekly (right) cycles of traffic flow at MR, (middle and bottom left) diurnal cycles of 2 h median NO_x and total PM_{10} mass concentrations at MR, NK and DE split in SW and NE wind sectors, and (middle and bottom right) weekly cycles of 2 h median NO_x and total PM_{10} mass concentrations at MR, NK and DE. See Sect. 4.2.2 for the definition of the wind direction sectors. Time stamp is start of 2 h averaging period, so 00:00 LT means averaging between 00:00 and 02:00 LT.

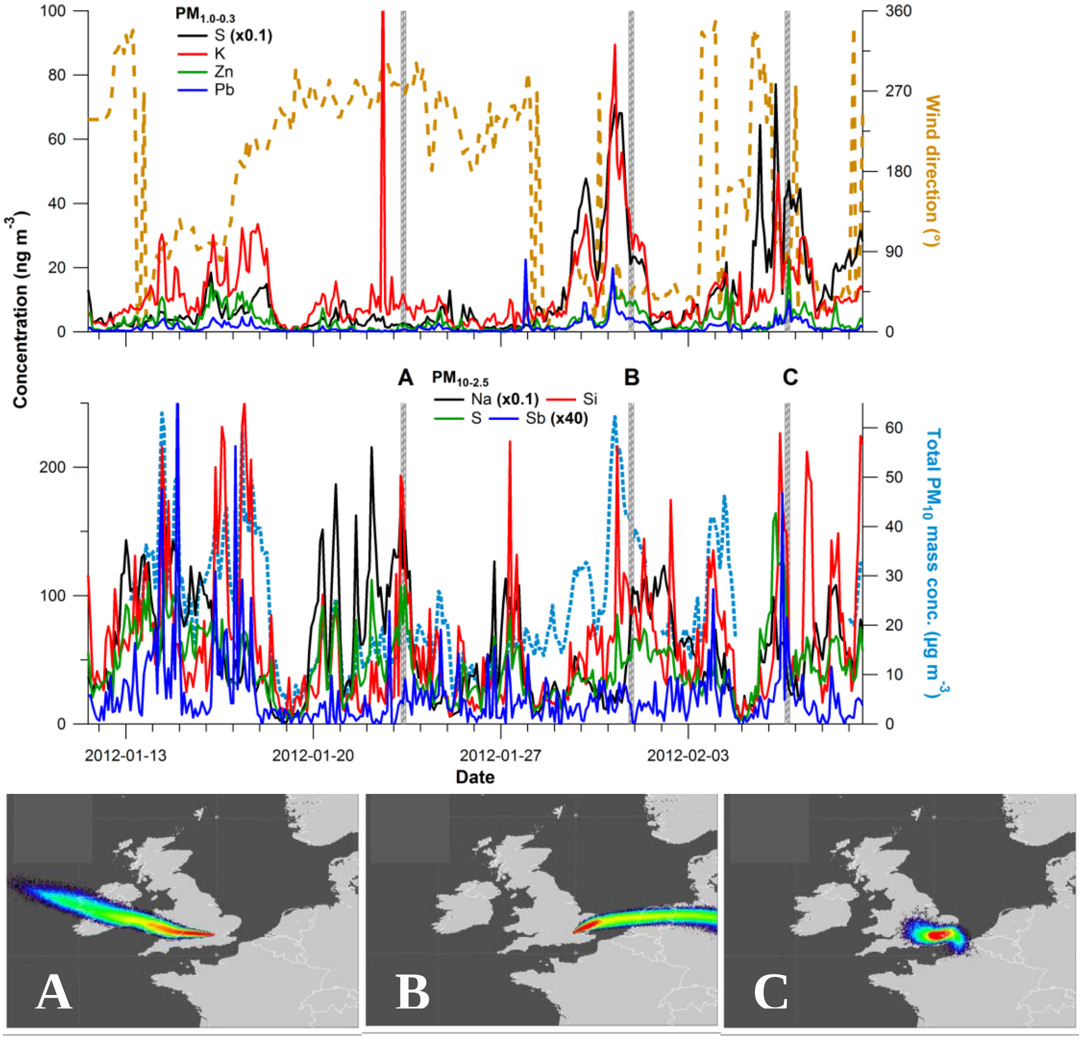

Figure 9. (top panel) Time series of (top left axis) PM$_{1.0-0.3}$ S, K, Zn and Pb concentrations at NK and (top right axis) wind direction from BT Tower, time series of (bottom left axis) PM$_{10-2.5}$ Na, Si, S and Sb concentrations at NK and (bottom right axis) total PM$_{10}$ mass concentration at NK; (bottom panel) three NK footprints simulated with the NAME model corresponding to the vertical lines (A, B, C) indicated in the top panel. Trajectories are simulated for particles released from NK and followed back at 0-100 m a.g.l. for the previous 24 h at: **(A)** 23 January 2012 09:00 LT, **(B)** 31 January 2012 21:00 LT, **(C)** 6 February 2012 18:00 LT; particle concentrations increase from blue to red.

Supplement A: RDI backup filter and PM$_{1.0}$ cut off analysis

RDI backup filter analysis

RDI backup filters (Balston 050-11-BQ 2 µm, microfiber, fluorocarbon resin binder) from the ClearfLo winter campaign were immersed in water and sonicated for about 1.5 h. One filter per measurement site was available. Total sulphate (SO_4^{2-}) mass was obtained by analysing the solutions with ion chromatography and converted to concentrations by dividing by the total air volume that passed through the filter during the campaign.

Table S1 compares the S concentrations from the RDI PM$_{1.0-0.3}$ stage with S (from SO_4^{2-}) collected by the backup filter. The sum of both (Total S < 1 µm) is compared with S from AMS sulphate measurements. The ratios of 0.67 to 1.26 in the last column reveal reasonable mass-closure between the RDI and AMS.

Table S1. Comparison between S from RDI PM$_{1.0-0.3}$ fractions and backup filters (S from SO_4^{2-}) with S from the AMS (S from SO_4^{2-}). Units in ng m^{-3}. The ratio of S in the RDI to the AMS is given in the last column (ratio of RDI Total S < 1 µm to AMS S).

Site	RDI PM$_{1.0-0.3}$ S	S in backup filter	Total S <1 µm	AMS S	Ratio RDI : AMS
MR	127	398	525	607	**0.86**
NK	113	405	518	412	**1.26**
DE	145	359	504	749	**0.67**

~~Table S1 compares the S concentrations from the RDI PM$_{1.0-0.3}$ stage with S (from SO_4^{2-}) collected by the backup filter. The sum of both (Total S < 1 µm) is compared with S from AMS sulphate measurements. The ratio in the last column reveals mass-closure between the RDI and AMS within 25 %.~~

~~**Table S1.** Comparison between S from RDI PM$_{1.0-0.3}$ fractions and backup filters (S from SO_4^{2-}) with S from the AMS (S from SO_4^{2-}). Units in ng m^{-3}. The ratio of S in the RDI to the AMS is given in the last column (ratio of RDI Total S < 1 µm to AMS S).~~

Site	RDI PM$_{1.0-0.3}$ S	S in backup filter	Total S <1 µm	AMS S	Ratio RDI : AMS
MR	195	398	593	476	**1.25**
NK	174	405	579	607	**0.95**
DE	224	359	583	715	**0.82**

RDI PM$_{1.0}$ cut off analysis

As noted in the main text and in Supplement C, elements whose mass is dominated by the PM$_{1.0}$ fraction are typically underestimated by RDI-SR-XRF relative to external measurements like the AMS and 24 h filter measurements. One explanation is that the collection efficiency of the RDI PM$_{1.0}$ stage is smaller than expected, e.g. by a larger-than-expected size cut off. We therefore performed new laboratory measurements of the RDI size-dependent collection efficiency, and compare these to earlier characterisations by Bukowiecki et al. (2009) and Richard et al. (2010).

Figure S1 shows the setup used for the collection efficiency measurements. $(NH_4)_2SO_4$, NH_4NO_3 and NaCl particles were nebulized, dried and size-selected using a differential mobility analyser (DMA, TSI, Inc., Shoreview, MN, USA), and then sampled with the RDI. The DMA was operated with sample and sheath flow rates of 0.3 and 3.0 L min^{-1}, respectively. A condensation particle counter (CPC1, TSI, Inc., Shoreview, MN, USA) with a flow rate of 1.0 L min^{-1} was continuously connected at the inlet stage of the RDI to measure the particles entering the RDI, and to correct for fluctuations in nebulizer performance. A second line led to an additional CPC (CPC2, 1 L min^{-1}) and an Aerodyne aerosol mass spectrometer (AMS, Aerodyne Research, Inc., Billerica, MA, USA) with a flow rate of 0.1 L min^{-1}. This line could be connected at the inlet, after the $PM_{2.5\text{-}1.0}$ (B) stage or after the $PM_{1.0\text{-}0.3}$ (C) stage. Measurements following the B and C stages were made by connecting the line to a small hole in the lid covering these stages, resulting in sampling of the air flow at a 90° angle (see picture in Figure S1). The total flow through the system was controlled by a mass flow controller connected to a clean air generator pumping air into the nebulizer and RDI simultaneously. The RDI was operated using three wheels with freshly mounted 6 µm polypropylene foils coated with Apiezon to minimize particle bouncing effects, to simulate ambient field measurements. Tests ruled out differences in measurements on the top or bottom side of the lid at the B and C stages. For the final results, all data was collected at the bottom side of the B and C stages.

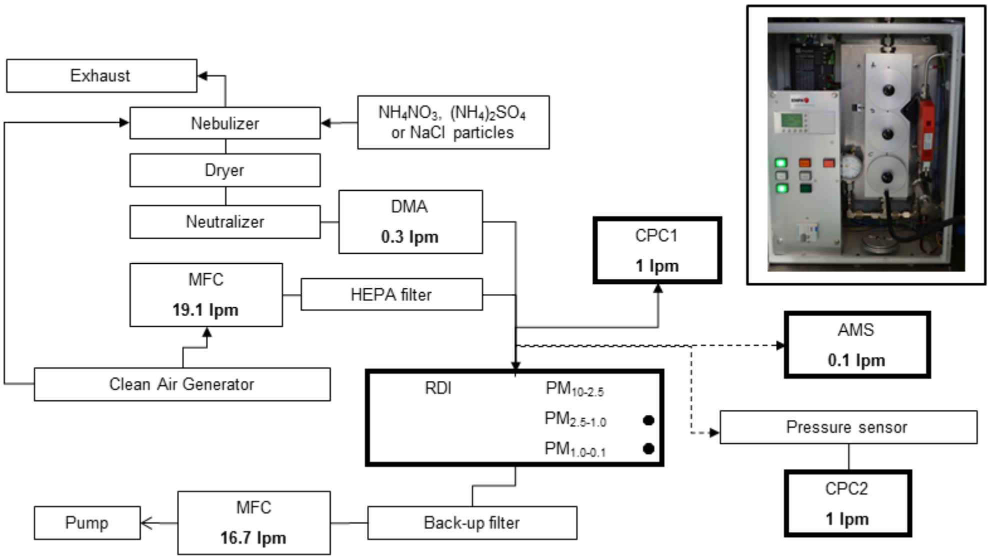

Figure S1. Setup of the collection efficiency measurements of the RDI $PM_{1.0}$ impactor stage. The line with the AMS and CPC2 was connected at the inlet, after the $PM_{2.5\text{-}1.0}$ or after the $PM_{1.0\text{-}0.3}$ stage. The picture of the RDI shows the connection at the bottom side of the lid of the $PM_{1.0\text{-}0.3}$ stage.

As noted above, measurements were conducted at the RDI inlet, after the B stage impactor (nominal size cut = 1.0 µm) and after the C stage impactor (nominal size cut = 0.1 µm). RDI collection efficiency at each stage is defined as 1 minus transmission. To correct for fluctuations in nebulizer concentrations, all data for a given set of CPC2/AMS measurements were normalized to a constant inlet (CPC1) concentration. Transmission from the inlet across the B stage impactor was between 90 and 100 % for all sizes (aerodynamic diameter $d < 950$ nm), indicating negligible particle losses and/or unintended collection of small particles. C stage collection efficiency (CE_C) was therefore calculated using Eq. (S1):

$$\boldsymbol{CE_C = 1 - \left(Conc_C * \frac{CPC1_{ref}}{CPC1_{measC}}\right) / \left(Conc_B * \frac{CPC1_{ref}}{CPC1_{measB}}\right)} \tag{S1}$$

Concentrations were measured using both CPC2 and the AMS. For large particles, where the fraction of multiple charged particles passed by the DMA is negligible, these two methods yield similar results. For smaller particles, collection efficiency as calculated by the CPC2 is biased low due to the presence of multiple charged particles with larger diameters, as clearly evidenced from AMS size distributions. For simplicity, we therefore present only the AMS results here. RDI collection efficiencies are calculated by fitting a lognormal distribution to each mode and using the resulting mass concentrations in Eq. S1. This allows simultaneous calculation of RDI collection efficiencies for several sizes, providing an internal consistency and stability check for the measurements.

Figure S2 shows the collection efficiency of the $PM_{1.0\text{-}0.3}$ (C stage) nozzle for two RDIs (RDI1 and RDI2) as a function of *d* for NH_4NO_3 particles. *D* is calculated from AMS size measurements, assuming a density of 1.74 and a Jayne shape factor (DeCarlo et al., 2004) of 0.8. Cut points are estimated by a sigmoidal fit to the collection efficiency curves, and yield different cut points for the two RDIs. RDI1 has a cut point of 290 ± 25 nm and RDI2 a cut point of 410 ± 15 nm. This discrepancy was investigated using RDI2 equipped with the $PM_{1.0\text{-}0.3}$ nozzle of RDI1 (RDI2 (nozzle RDI1)), demonstrating that the difference between the two RDIs is governed by nozzle performance, because the cut point of this system is 300 ± 20 nm and therefore closer to the RDI1 performance. Similar cut points for the various systems were obtained using $(NH_4)_2SO_4$ and NaCl particles (not shown).

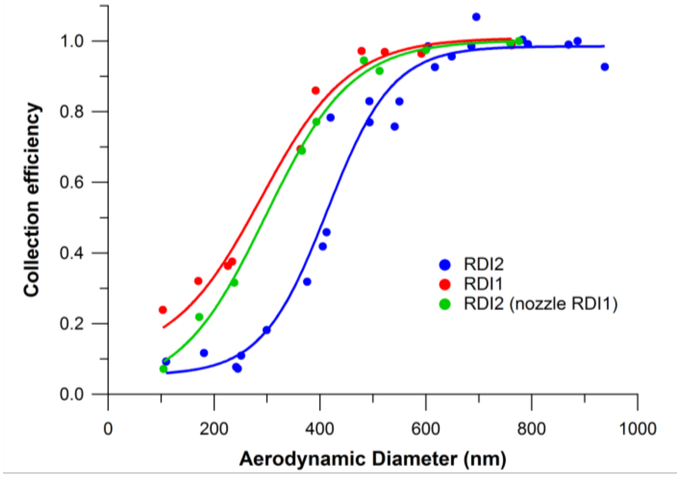

Figure S2. Collection efficiency of the RDI $PM_{1.0\text{-}0.3}$ impactor stage as a function of aerodynamic diameter.

Measurements of the nozzle sizes under a microscope reveal small differences between the RDIs. A 1.0 µm cut point at the B stage impactor is obtained with a nozzle size of 0.68 x 10 mm. The RDI1 and RDI2 B stage nozzles were 0.70 x 10 mm, and a third RDI that was used at Marylebone Road during ClearfLo had a size of 0.71 x 10 mm. The C stage nozzle size should measure 0.30 x 10 mm for a cut point of 0.1 µm. However, the nozzle sizes were 0.30-0.31 x 10, 0.30-0.32 x 10 and 0.32 x 10 for RDI1, RDI2 and the third RDI, respectively. We expect the deviations from these measurements from the machining of the nozzles, resulting in higher cut points than expected for the $PM_{1.0}$ stage, and possibly also for the $PM_{2.5-1.0}$ stage.

Conclusions

The $PM_{1.0-0.3}$ collection efficiency curves are different for the two RDIs. RDI2 has a larger small-end cut point of 410 ± 15 nm than RDI1 of 290 ± 25 nm. RDI2 with the $PM_{1.0-0.3}$ nozzle of RDI1 resulted in a similar cut point of RDI1 of 300 ± 20 nm. The slightly larger nozzles than theoretically calculated are the likely reason for the observed increase in the small-end cut point of the $PM_{1.0-0.3}$ nozzle and thus in reduced particle collection at the C stage.

Supplement B: Changes in SR-XRF analysis

The data described in the main text was obtained with RDI-SR-XRF analysis. The following significant changes were made in the SR-XRF analysis compared to the methodology described in Bukowiecki et al. (2005, 2008) and Richard et al. (2010):

1. At SLS, we replaced the silicon drift detector (Roentec Xflash 2001 type 1102, Bruker AXS) with an e2v SiriusSD detector (SiriusSD-30133LE-IS). This detector is equipped with a thin polymer window resulting in a wider energy range down to about 300 eV and a better energy resolution of 133 eV (Mn Kα at 5.9 keV). In addition, the setup accepts a higher throughput resulting in negligible dead time effects. We also replaced the helium chamber with an in-house built vacuum chamber (sample exposure system for micro-X-ray fluorescence measurements, SESmiX) which reaches about 10^{-6} bar. This extended the measured range of elements down to Na and Mg.

2. Reference standards for calibration of element fluorescence counts to mass concentrations were produced on the same 6 µm PP substrate as used for RDI sampling, in contrast to the previous standard where a much thicker 100 µm PET foil (Folex, BG-32.5 RS plus) was used. Two standards suitable for measurements at both SLS and HASYLAB contained elements in equal concentrations, and have a similar mix of elements as the standard previously used. Two additional standards containing only specifically selected light elements were produced. One standard contained Na, Al, P, Cl and Ca; the other Mg, Si, S, K and Ca. The concentrations of these elements were increased by a factor 3.8 relative to the other two standards to improve signal-to-noise ratios in the SR-XRF calibration. Co was added to these additional standards, but in the same concentration as in the other two foils and was used as a quality check of the fabrication procedure of the four standards. The concentration difference of the light elements was taken into account before applying the relative calibration of the sample elements. The new reference standards allowed the use of identical geometry and irradiation time for RDI samples and reference standards, meaning that all SR-XRF measurements exhibit the same scattering and secondary fluorescence excitation. This reduced uncertainties in both the absolute and relative calibration of the samples.

3. Previously, spectra were fitted with the WinAxil software package (Canberra Inc; Van Espen et al., 1986). This rather old spectral fitting package allows little flexibility in spectrum continuum correction and peak fitting. PyMCA (Sole et al., 2007) on the other hand, is more flexible, but lacks the possibility to save uncertainty calculations in batch mode. In this study, spectra were fitted with an in-house developed software package called Spectral Analysis for Multiple Instruments – toolkit for XRF (SAMI-XRF) using the IGOR Pro software environment (Wavemetrics, Inc., Portland, OR, USA) to evaluate the data and create custom interfaces to accomplish specialized tasks. SAMI sequentially determines (1) energy calibration of the X-ray line as a function of detector channel; (2) spectrum continuum correction; (3) peak width calibration as a function of energy (assuming Gaussian peak shape and a general square root law of the full-width-half-maximum (FWHM) energy relation); and (4) peak fitting of the entire spectrum, at which stage only peak heights are fitted as a free parameter and all other parameters are fixed. Steps (1) and (3) are performed with user-selected reference peaks, and incorporates fitting of complex (multi-Gaussian) peak shapes caused by nearly complete overlapping $K\alpha_1$ and $K\alpha_2$ lines. Step (2) utilizes collected spectra of a blank foil as a reference for the continuum shape, and scales this reference to user-selected element-free regions of the processed spectra. Step (4) allows lines to be fitted freely or fixed to another line, e.g.

to the strongest line in a shell. For example, the Kα_2 and Kβ lines can be fixed to the Kα_1 line according to the relative intensities given by Bearden (1967). In this study, all lines within an electron shell were fitted fixed to the strongest line in that shell. Additionally, Ni, Cu and Zn L$\alpha_{1,2}$ lines were fixed to the Kα_1 line to reduce the influence of peak overlap with Na. The ratios of L$\alpha_{1,2}$ to Kα_1 for Ni, Cu and Zn were determined by fitting calibration standards having these elements but low Na. Final fits were then obtained using the acquired relations, thereby reducing uncertainties in the Na concentrations due to peak overlap and improving Na quantification.

Supplement C: Data intercomparison

A short description of the data intercomparison between RDI-SR-XRF data and independent filter data is given in Sect. 3 of the main text. Here the details of this comparison are given. We compare XRF data with filter data (24 h PM$_{10}$ trace element data analysed with ICP-MS; roughly 9 % uncertainty at a 95 % confidence interval and calibrated with NIST standards) for 18 elements collected at MR and NK (no filter data was available at DE). For this comparison, the three size ranges of the RDI were summed up to total PM$_{10}$ and averaged to the filter collection period. The intercomparison results are shown in Fig. S3, and are divided into four groups to facilitate discussion. Fit coefficients and Pearson's *R* values for the intercomparison are shown in Table S2, while XRF uncertainties and detection limits are given in Table S3. For ~~all~~ most elements~~, except Mn and the lightest elements,~~ the sample inhomogeneity provides the largest source of uncertainty of maximal 20 %. Significant uncertainties of 54-~~35~~9 % in Na-~~Si~~Ca arise from corrections on self-absorption effects for the calibration standards. We assume a static size distribution of the coarse and intermediate fraction ambient samples. Therefore, no additional uncertainties arise from self-absorption corrections in the samples. RDI flow rate fluctuations are estimated at a maximum of 5 %. Absolute and relative calibration uncertainties are larger for lighter elements due to their low fluorescence yields, making them harder to detect. For Na-K these uncertainties are 13 %, for Ca-Pb only 2 %. The last source of uncertainty is the energy calibration of an X-ray line as function of detector channel and shows the effect of line overlap in the detection of a specific line. The uncertainties range between 1 and 22 % for most elements, but are around 60 % for Mn due to the overlap with Fe being present in much higher concentrations (on average a factor of 55). Overall, the total uncertainties are estimated at 21-~~30~~40 % for most elements (46-83 % for Mn; 60-43 % for Na-Si). All RDI data points lie well above their detection limits (last column Table S3).

Elements shown in Fig. S3a (Al, Ca, Ti, Mn, Fe, Cu, Zn, Sr, Sb, Ba) agree within approximately ± 50 % with good correlations (Pearson's *R* > 0.78). Na and Mg are shown separately in Fig. S3b, because these elements are strongest affected by XRF self-absorption. In Fig. S3c-d, we show elements for which the intercomparison shows significant biases and/or no significant correlation between RDI and filters. Note that the elements exhibiting good agreement in Fig. 3a-b span orders of magnitude difference in concentration (and fluorescence counts), suggesting that there are no global or concentration-dependent biases in the RDI-SR-XRF data. For elements exhibiting lesser agreement (Fig. S3c-d), this leaves the element relative calibration (i.e. element fluorescence yield as a function of line energy), spectral peak fitting, and instrument size cut points as potential sources of error in the XRF analysis.

Figure S3b shows good agreement for Na and Mg within a factor of 1.10-1.30 and good correlations (Pearson's *R* 0.89-0.99) despite the large correction of the RDI data due to self-absorption effects in the calibration standards and the coarse and intermediate ambient samples. This leads to significant uncertainty in the absolute concentrations of those elements. Furthermore, the XRF relative calibration curve for Na and Mg is difficult to constrain due to the low response of these elements, but only led to an uncertainty of 13 % (for Na-K compared to 2 % for Ca-Pb).

Figure S3c shows good correlations for Mo (Pearson's *R* = 0.90), but the RDI measures a factor 2.4 higher concentrations than found on the filters, whereas Ni shows no significant correlation between RDI and filters (Pearson's *R* = 0.56). The most likely reason for the discrepancy between both methods is the ICP-MS extraction efficiency. This was 66 % for Ni, but unknown for Mo, leading to increased uncertainties in the absolute concentrations of the filter data. As shown in the main text, the RDI time series of these elements (including both urban/kerb increments and diurnal/weekly cycles) are consistent with those of elements expected to be co-emitted by the same sources. Visual inspection of the spectrum indicates that significant interferences between lines are unlikely, and this is confirmed by peak fitting sensitivity tests investigating the response of the calculated concentrations to uncertainties in line energy calibration (i.e. energy as a function of detector channel). We estimate a 3 % uncertainty in the measurement of Mo due to spectral analysis and an overall uncertainty of 21 %. Mo falls in a well-constrained region of the calibration curve (although is not directly measured on calibration foils), so relative calibration errors would require a systematic bias across this entire region of the calibration curve. While there are not enough jointly measured elements within the intercomparison to evaluate this possibility, good agreement between RDI and filter measurements is obtained through Sr (Kα = 14.1 keV) and at Sb (Kα = 26.4 keV) (Mo Kα lines fall at 17.5 keV), suggesting such a bias is unlikely. Spectral analysis uncertainties are 6 % for Ni (overall uncertainty of 22 %). Unlike Mo, the relative calibration is well-constrained both in terms of elements directly measured on calibration foils and in terms of intercomparison with nearby elements in the XRF calibration curve, where Ni falls just above Mn and Fe and just below Cu and Zn. RDI and filter measurements are shown to be in good agreement for these six elements in Fig. S3a.

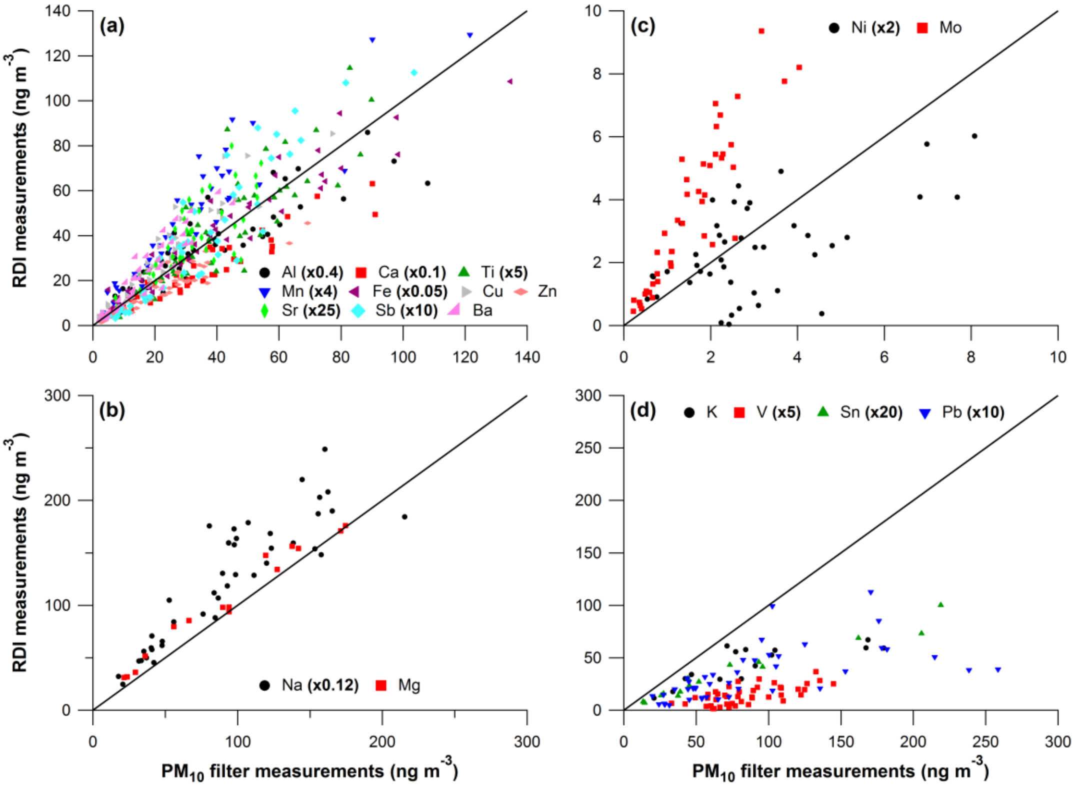

Figure S3. Total PM$_{10}$ element mass concentrations measured by the RDI (sum of PM$_{10\text{-}2.5}$, PM$_{2.5\text{-}1.0}$ and PM$_{1.0\text{-}0.3}$ fractions) at MR and NK averaged to 24 h versus 24 h PM$_{10}$ filter measurements of elements for (a) elements that agree within ± 50 %, (b) elements that agree but have a higher uncertainty due to self-absorption corrections, (c) elements with poor correlations, (d) other elements. The one-to-one line is added in black. See Table S2 for fit coefficients and Pearson's *R* values. Note that many elements are scaled to improve visualization.

Table S2. Fit coefficients and Pearson's *R* values for elements measured with the RDI ($PM_{10-2.5}$, $PM_{2.5-1.0}$ and $PM_{1.0-0.3}$ fractions summed to total PM_{10} and averaged to 24 h) relative to 24 h PM_{10} filter measurements. Data points were fitted with an orthogonal fit and forced zero intercept.

Element	Fit coefficient	Pearson's *R*
Na	~~1.30~~1.32	0.89
Mg	1.09	0.99
Al	~~0.89~~0.90	~~0.89~~0.88
K	~~0.55~~0.46	0.78
Ca	~~0.81~~0.70	0.94
Ti	1.04	0.86
V	0.17	0.66
Mn	1.37	0.91
Fe	0.95	0.96
Ni	0.71	0.56
Cu	1.30	0.95
Zn	0.70	0.94
Sr	1.21	0.78
Mo	2.35	0.90
Sn	0.43	0.98
Sb	1.18	0.93
Ba	1.36	0.94
Pb	0.34	0.61

The elements K, V, Sn and Pb in Fig. S3d show reasonable correlations between RDI and filter measurements (Pearson's *R* > 0.61) but the RDI data is less than half the filter data (filter measurements of K and Sn only at NK). Pb has a significant fraction of the mass in the fine fraction (see Fig. 2 in main text). Underestimation by the RDI is explained by its small-end cut point of 290-410 nm. Typically, K, V and Sn are also mainly emitted in the fine fraction, and might be affected by the cut off similarly to Pb.

S is a useful element for evaluation of the small-end cut off, as it is dominant in the fine fraction and measurable by several techniques. Therefore, we compared S data obtained with the RDI to simultaneous S mass calculated from sulphate (SO_4) measured by an AMS at MR, NK, and DE. The results in Supplement A show that the S mass in the RDI is on average about ~~three~~ 4.5 times lower than that measured by the AMS. This is consistent with the difference between RDI and filter measurements for fine fraction dominated elements. The RDI backup filter, which collects particles too small to impact at the $PM_{1.0-0.3}$ stage, was analysed for SO_4^{2-} using ion chromatography (Supplement A). Adding the S from this analysis to the S collected at the RDI $PM_{1.0-0.3}$ stage yielded mass closure with the S from AMS measurements within ~ ~~25~~30 % at all three sites. This suggests that elements with considerable mass in the small end of the $PM_{1.0}$ size range are not sampled by the $PM_{1.0-0.3}$ stage. This affects S and Pb, and potentially also K, S, Zn, Br and Sn. To further investigate this effect, new RDI collection efficiency measurements for the $PM_{1.0}$ deposition stage were performed (Supplement A). The actual small-end cut off was determined to be 290-410 nm, rather than the previously measured value of 100 nm (Bukowiecki et al., 2009; Richard et al., 2010), and found to be very sensitive to the machining tolerances of the $PM_{1.0}$ nozzle.

Only a small fraction of the measured elements are affected by this cut off issue in the sense that absolute values are smaller than with a $PM_{1.0-0.1}$ stage. Further, because the analyses presented in the main text depends on site-to-site ratios (for the same element) and relative concentration changes, potential biases are reduced by the similar (though not identical, see Fig. S2 in Supplement A) cut offs of the different RDI units. The conclusions presented in the main text are thus not significantly affected by this artefact.

Table S3. Estimated total uncertainty (% of measured value) of the calculated element concentrations per size fraction, and detection limits for each element (ng m^{-3}).

Element	PM$_{10-2.5}$ (%)[a]	PM$_{2.5-1.0}$ (%)[a]	PM$_{1.0-0.3}$ (%)[a]	DL (ng m^{-3})[b]
Na	59	59	60	2.552
Mg	55	55	55	0.962
Al	48	48	48	1.709
Si	43	43	43	0.420
P	37	37	37	0.118
S	34	34	34	0.503
Cl	31	31	31	0.158
K	28	28	28	0.031
Ca	23	23	23	0.267
Ti	24	26	27	0.024
V	30	30	24	0.008
Cr	27	27	26	0.015
Mn	83	69	46	0.042
Fe	21	21	21	0.033
Ni	22	22	21	0.005
Cu	21	21	21	0.028
Zn	21	21	21	0.058
Br	21	21	21	0.117
Sr	21	21	21	0.036
Zr	21	21	21	0.036
Mo	21	21	21	0.037
Sn	21	21	21	0.061
Sb	21	21	21	0.052
Ba	21	21	21	0.254
Pb	21	21	21	0.137

[a] Combination of uncertainties regarding sample inhomogeneity (20 %), self-absorption corrections (Na 54, Mg 49, Al 41, Si 35, P 27, S 23, Cl 19, K 13 and Ca 9 %)[d], RDI flow rate (5 %), absolute and relative calibration (Na-K 13 %, Ca-Pb 2 %) and spectral analysis specific per element and size fraction (median uncertainties for all data points).

[b] Taken as 3x the standard deviation of the spectra signals used for continuum corrections.

[c] Na uncertainties might be underestimated due to the overlap with the L lines of Ni, Cu and Zn. In the current analysis the ratio of the Lα to Kα lines are determined empirically, and quantification of the associated uncertainties is under investigation.

[d] Uncertainties regarding self-absorption corrections are based on the microscopic analysis of the particle size on the calibration standards. The particle size of the dried droplets shows a geometric mean of the volume size distribution of 9 µm, and 50 % of the particles are in the range 4-14 µm (see also Table 2 in main text).

~~**Table S3.** Estimated total uncertainty (% of measured value) of the calculated element concentrations per size fraction, and detection limits for each element (ng m^{-3}).~~

~~Element~~	~~PM$_{10-2.5}$ (%)~~[a]	~~PM$_{2.5-1.0}$ (%)~~[a]	~~PM$_{1.0-0.3}$ (%)~~[a]	~~DL (ng m^{-3})~~[b]
~~Na~~	~~59~~	~~59~~	~~60~~	~~2.552~~
~~Mg~~	~~55~~	~~55~~	~~55~~	~~0.962~~
~~Al~~	~~48~~	~~48~~	~~48~~	~~1.709~~
~~Si~~	~~43~~	~~43~~	~~43~~	~~0.420~~
~~P~~	~~25~~	~~25~~	~~25~~	~~0.118~~
~~S~~	~~24~~	~~24~~	~~24~~	~~0.503~~

~~Cl~~	~~24~~	~~24~~	~~24~~	~~0.158~~
~~K~~	~~24~~	~~24~~	~~24~~	~~0.031~~
~~Ca~~	~~21~~	~~21~~	~~21~~	~~0.267~~
~~Ti~~	~~24~~	~~26~~	~~27~~	~~0.024~~
~~V~~	~~30~~	~~30~~	~~24~~	~~0.008~~
~~Cr~~	~~27~~	~~27~~	~~26~~	~~0.015~~
~~Mn~~	~~83~~	~~69~~	~~46~~	~~0.042~~
~~Fe~~	~~21~~	~~21~~	~~21~~	~~0.033~~
~~Ni~~	~~22~~	~~22~~	~~21~~	~~0.005~~
~~Cu~~	~~21~~	~~21~~	~~21~~	~~0.028~~
~~Zn~~	~~21~~	~~21~~	~~21~~	~~0.058~~
~~Br~~	~~21~~	~~21~~	~~21~~	~~0.117~~
~~Sr~~	~~21~~	~~21~~	~~21~~	~~0.036~~
~~Zr~~	~~21~~	~~21~~	~~21~~	~~0.036~~
~~Mo~~	~~21~~	~~21~~	~~21~~	~~0.037~~
~~Sn~~	~~21~~	~~21~~	~~21~~	~~0.061~~
~~Sb~~	~~21~~	~~21~~	~~21~~	~~0.052~~
~~Ba~~	~~21~~	~~21~~	~~21~~	~~0.254~~
~~Pb~~	~~21~~	~~21~~	~~21~~	~~0.137~~

[a] ~~Combination of uncertainties regarding sample inhomogeneity (20 %), self-absorption corrections (Na-Si 54-35 %)~~[d]~~, RDI flow rate (5 %), absolute and relative calibration (Na-K 13 %, Ca-Pb 2 %) and spectral analysis specific per element and size fraction (median uncertainties for all data points).~~

[b] ~~Taken as 3x the standard deviation of the spectra signals used for continuum corrections.~~

[c] ~~Na uncertainties might be underestimated due to the overlap with the L lines of Ni, Cu and Zn. In the current analysis the ratio of the Lα to Kα lines are determined empirically, and quantification of the associated uncertainties is under investigation.~~

[d] ~~Uncertainties regarding self-absorption corrections are based on the microscopic analysis of the particle size on the calibration standards. The particle size of the dried droplets shows a geometric mean of the volume size distribution of 9 µm, and 50 % of the particles are in the range 4-14 µm.~~

Supplement D: Additional tables and figures

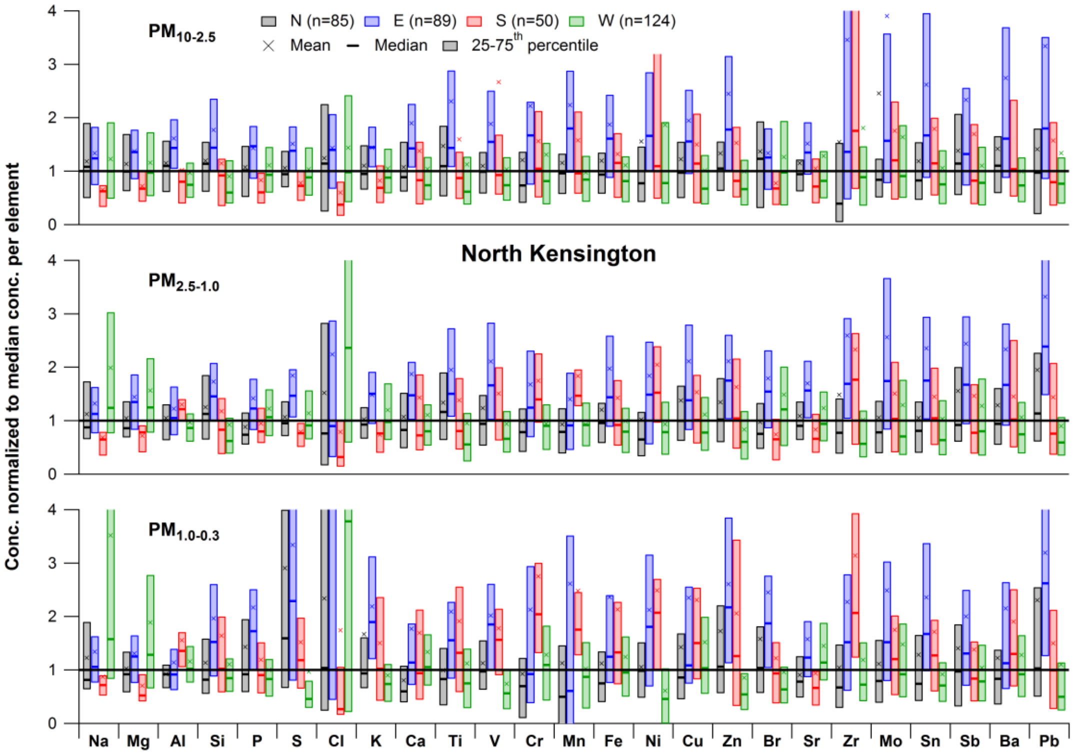

Figure S4. Same as Fig. 4 in main text, but for NK with mean, median and 25-75th percentile trace element concentrations split in four wind direction sectors (N, E, S, W) normalized to the global median concentration per element for $PM_{10-2.5}$ (top), $PM_{2.5-1.0}$ (middle) and $PM_{1.0-0.3}$ (bottom). See Sect. 4.2.2 for the definition of the wind direction sectors.

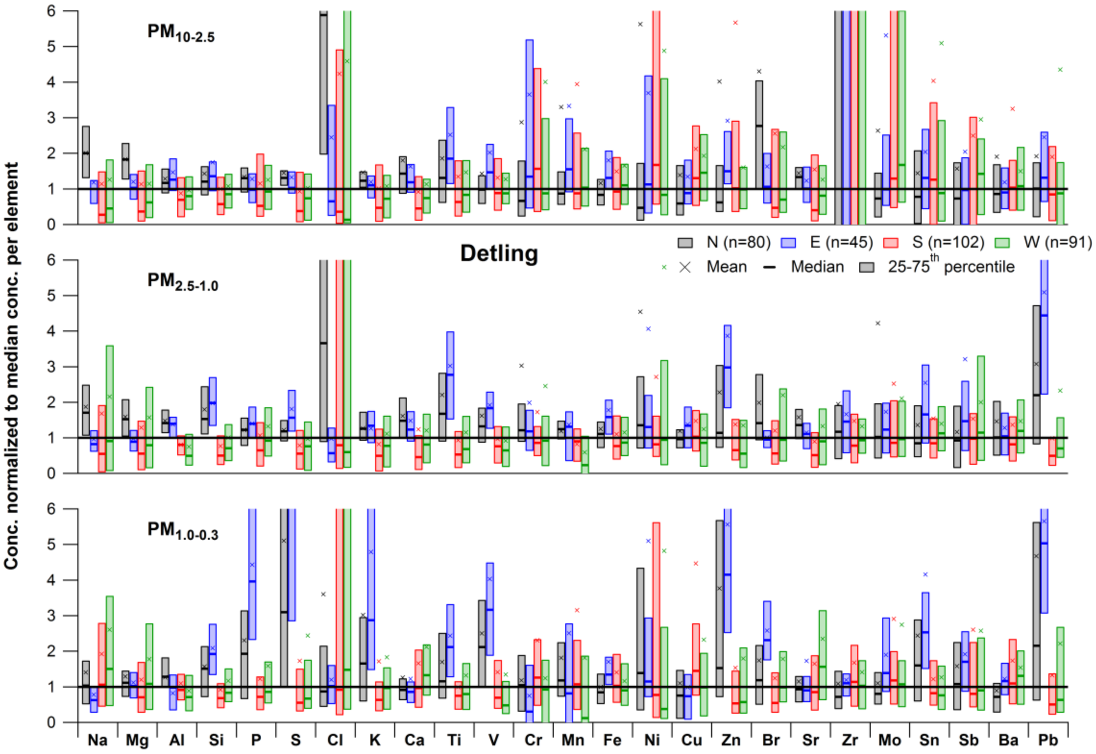

Figure S5. Same as Fig. 4, but for DE with mean, median and 25-75th percentile trace element concentrations split in four wind direction sectors (N, E, S, W) normalized to the global median concentration per element for PM$_{10-2.5}$ (top), PM$_{2.5-1.0}$ (middle) and PM$_{1.0-0.3}$ (bottom). See Sect. 4.2.2 for the definition of the wind direction sectors.

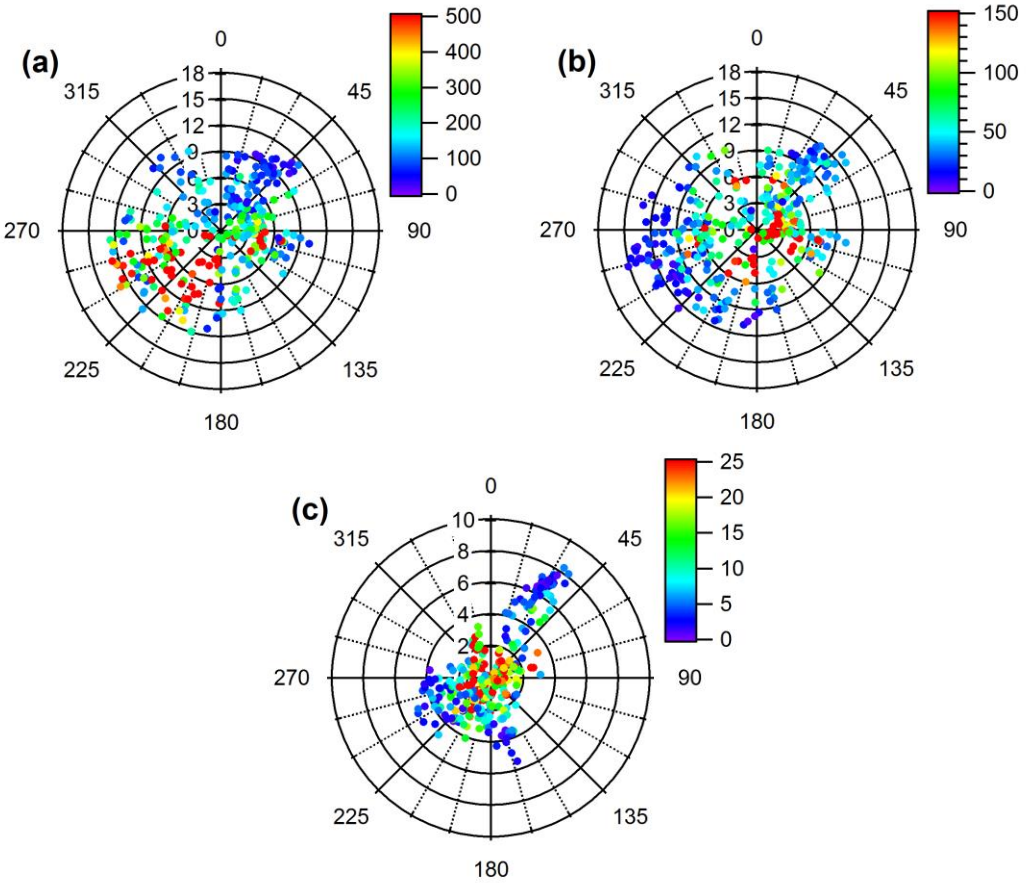

Figure S6. Wind roses as a function of wind direction (angle) and wind speed (diameter) at (a) BT Tower, color-coded by NO_x concentrations (ppb) at MR, (b) BT Tower, color-coded by NO_x concentrations (ppb) at NK, (c) DE, color-coded by NO_x concentrations (ppb) at DE for the RDI sampling periods (see Table 1 in main text).

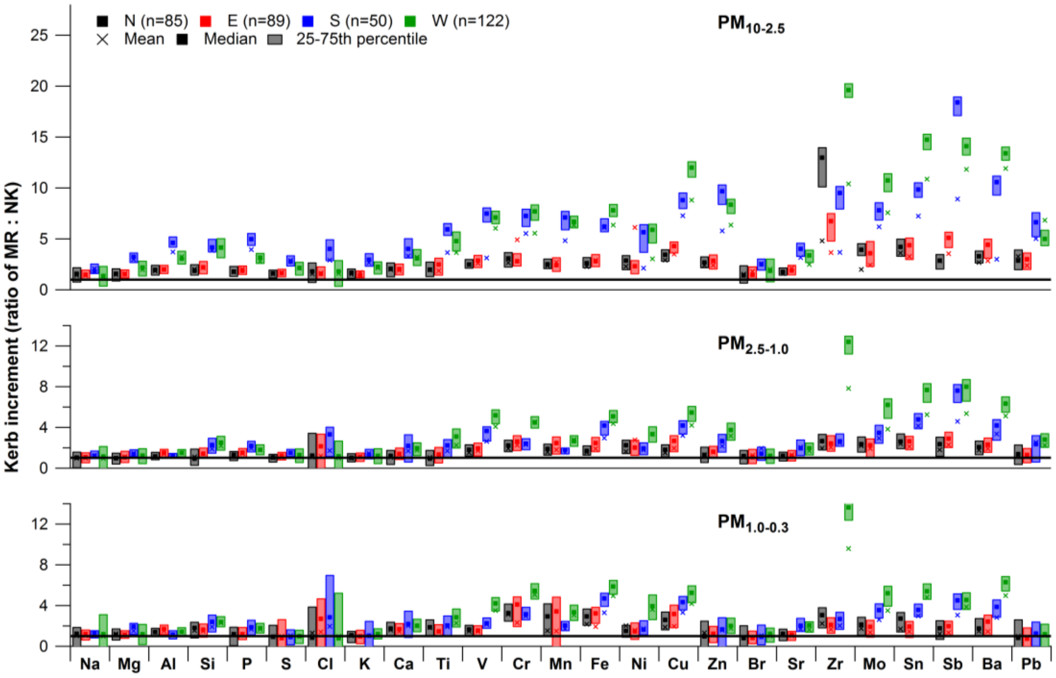

Figure S7. Same as Fig. 5, but with mean, median and 25-75th percentile kerb increment values for trace elements at MR relative to NK for $PM_{10-2.5}$ (top), $PM_{2.5-1.0}$ (middle) and $PM_{1.0-0.3}$ (bottom) split in N, E, S and W wind sectors. See Sect. 4.2.2 for the definition of the wind direction sectors.

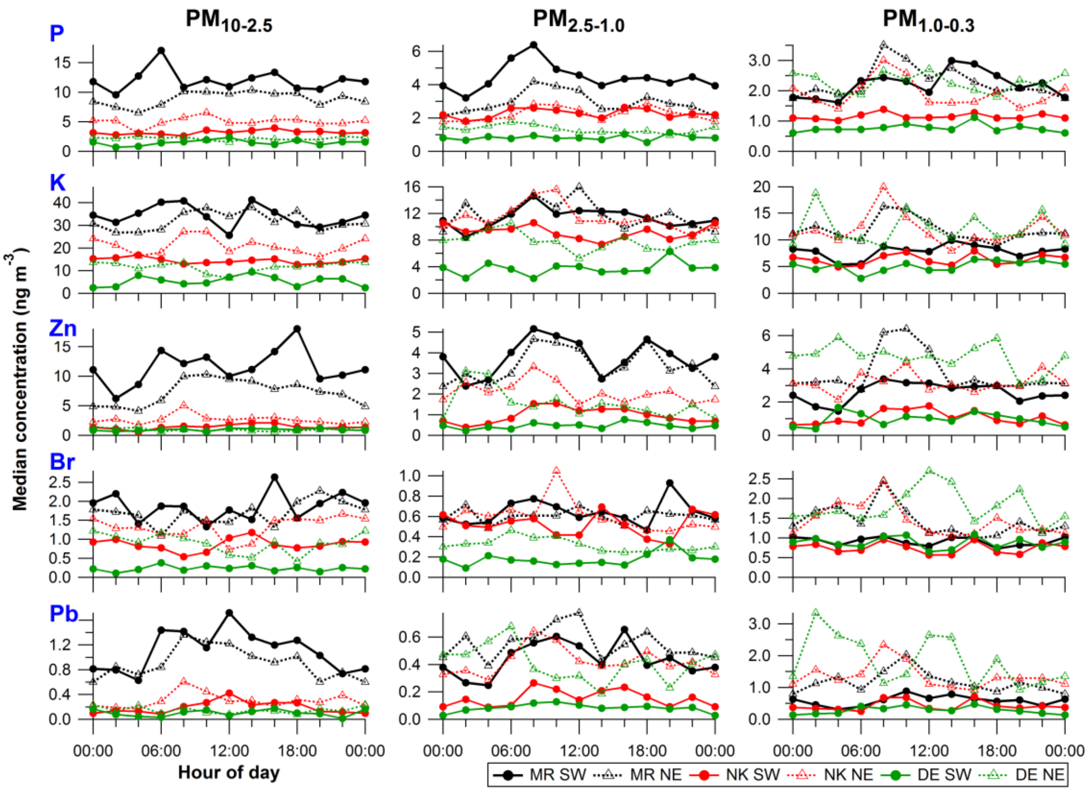

Figure S8. Same as Fig. 6, but for all other elements: P, K, Br, Zn, Pb (regional background); Mg (sea salt), Al, Ca, Ti, Sr (mineral dust); Cl (sea salt), V, Cr, Mn, Ni (traffic-related); Cu, Zr, Mo, Sn, Ba (brake wear). Diurnal cycles of 2 h median concentrations for $PM_{10-2.5}$ (left), $PM_{2.5-1.0}$ (middle) and $PM_{1.0-0.3}$ (right) at MR, NK, DE split in SW and NE wind sectors. See Sect. 4.2.2 for the definition of the wind direction sectors. Hour of day is start of 2 h sampling period, so 00:00 LT means sampling from 00:00 to 02:00 LT.

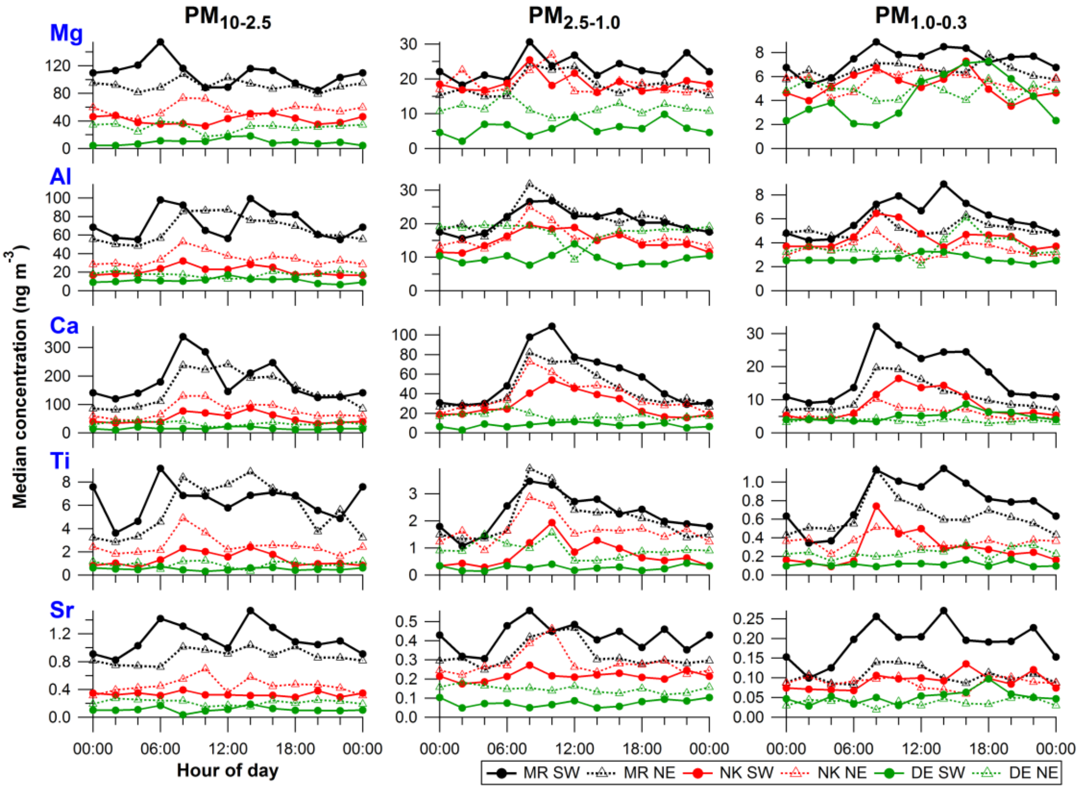

Figure S8. Continued.

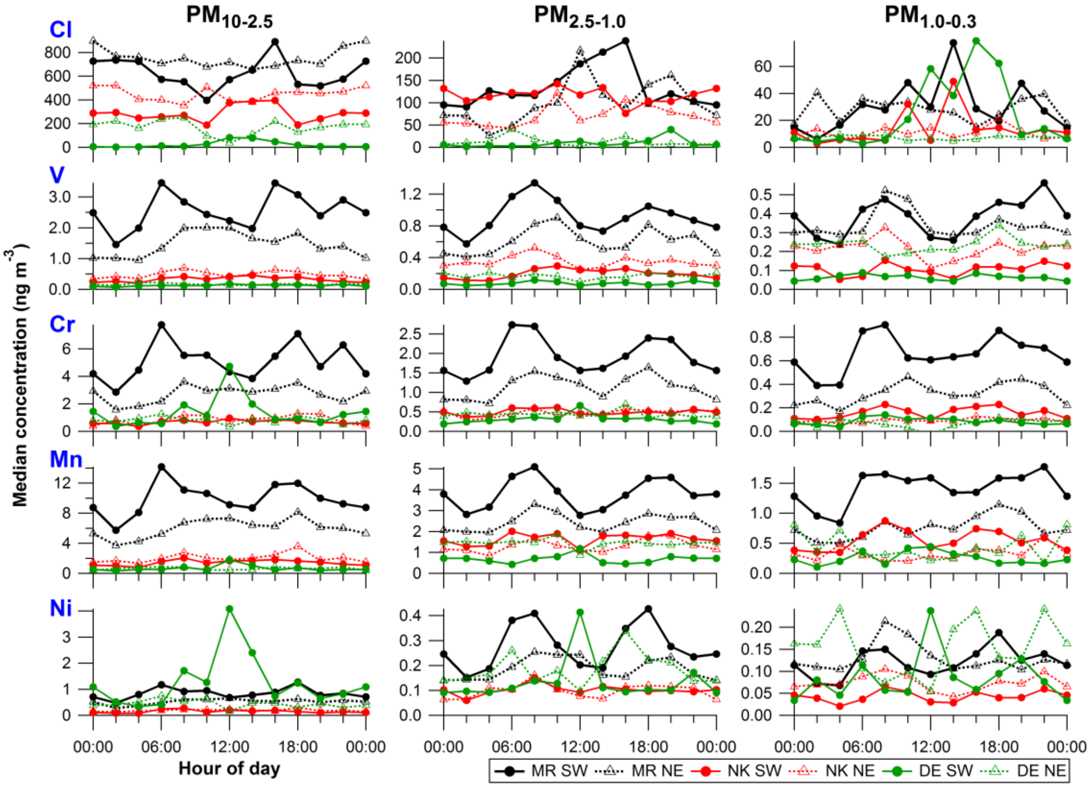

Figure S8. Continued.

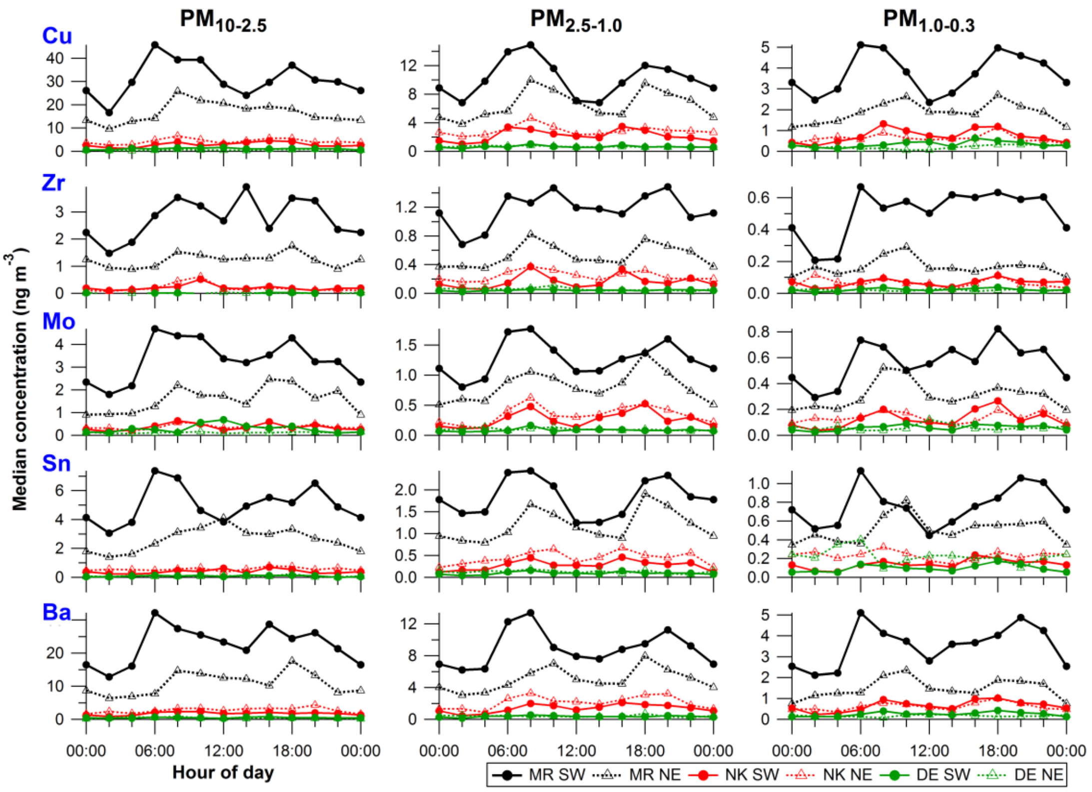

Figure S8. Continued.

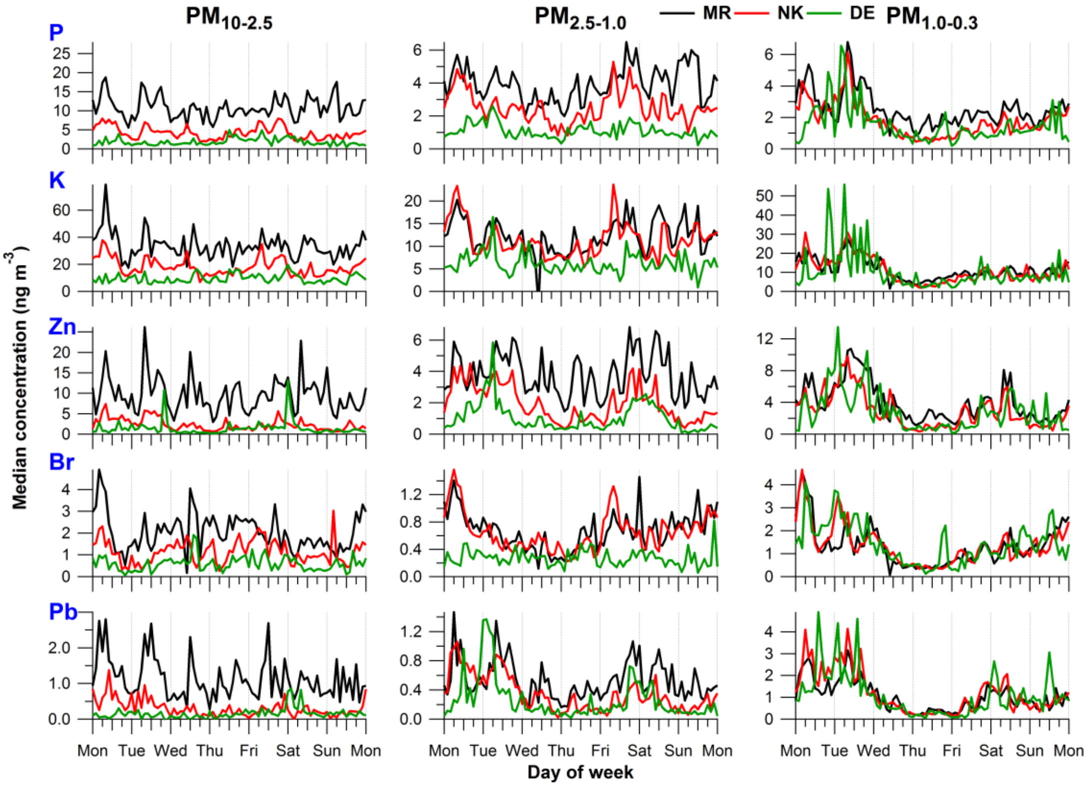

Figure S9. Same as Fig. 7, but for all other elements: P, K, Br, Zn, Pb (regional background); Mg (sea salt), Al, Ca, Ti, Sr (mineral dust); Cl (sea salt), V, Cr, Mn, Ni (traffic-related); Cu, Zr, Mo, Sn, Ba (brake wear). Weekly cycles of 2 h median concentrations for $PM_{10\text{-}2.5}$ (left), $PM_{2.5\text{-}1.0}$ (middle) and $PM_{1.0\text{-}0.3}$ (right) at MR, NK, DE.

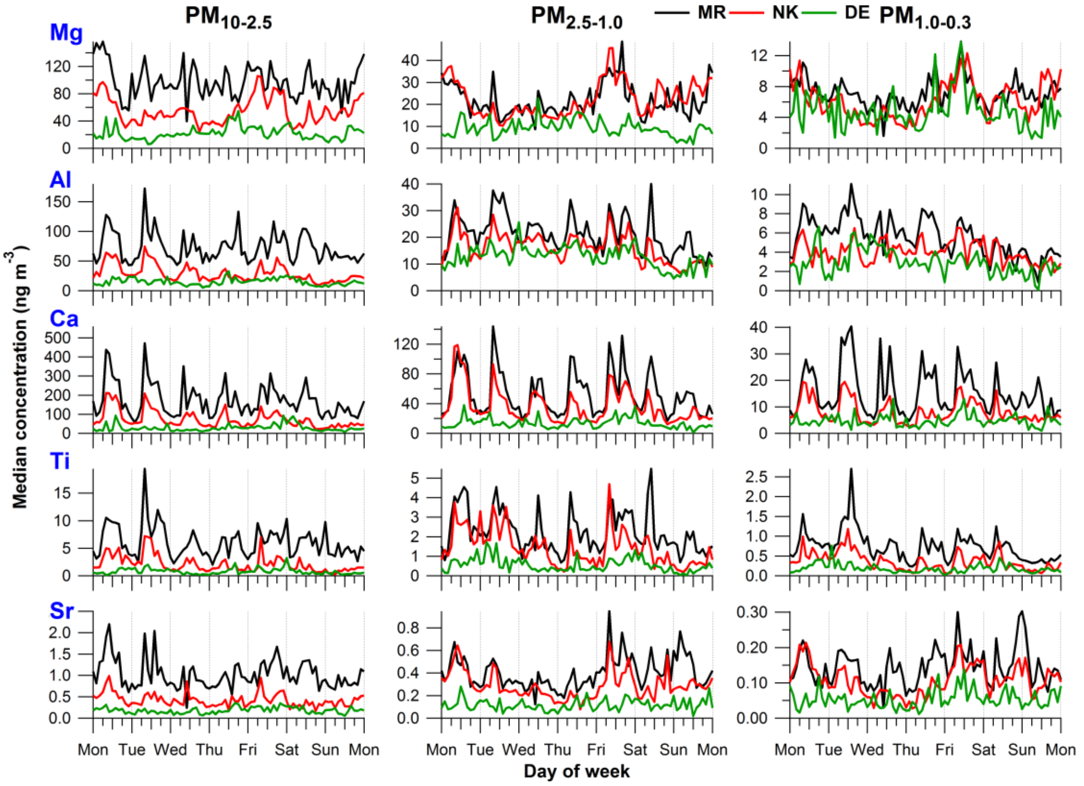

Figure S9. Continued.

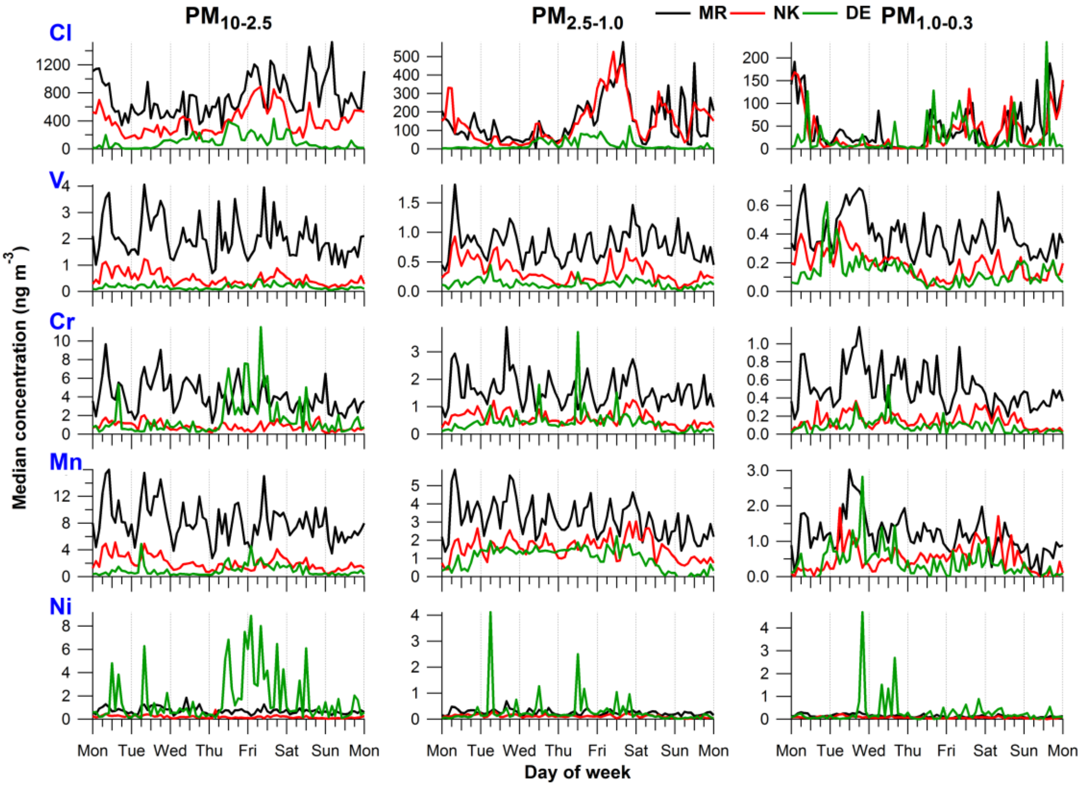

Figure S9. Continued.

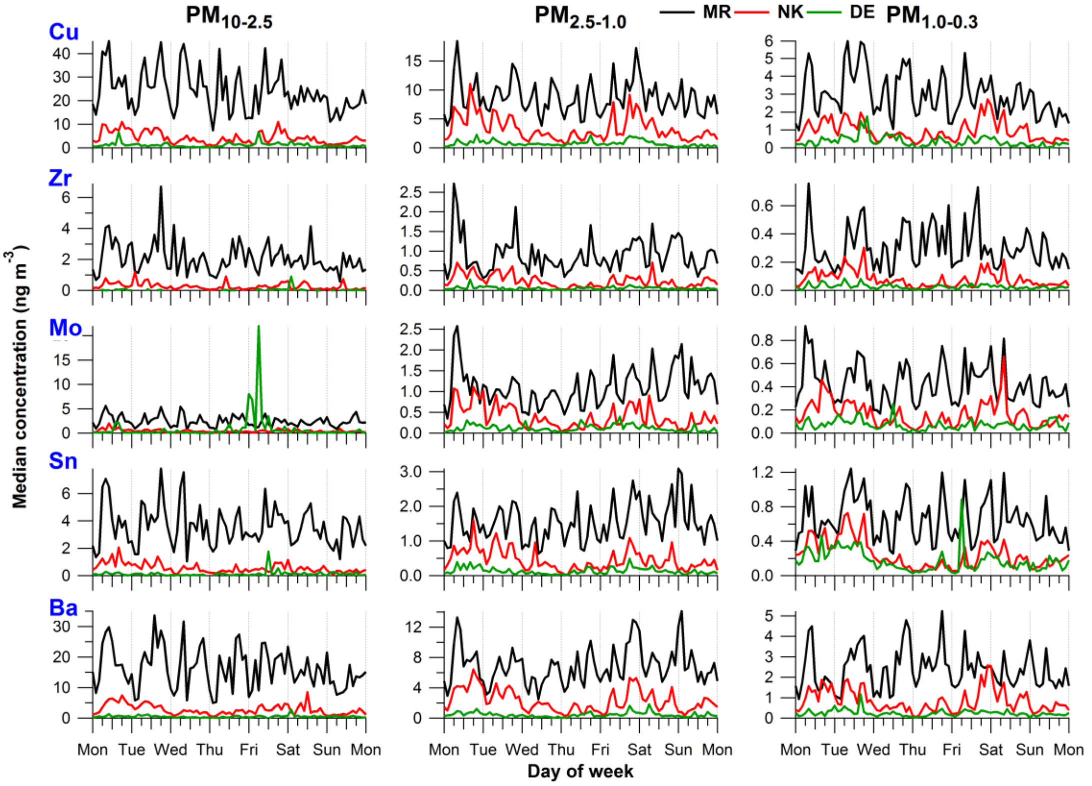

Figure S9. Continued.

References

Bearden, J. A.: X-ray wavelengths, Rev. Mod. Phys., 39, 78-124, doi:10.1103/revmodphys.39.78, 1967.

Bukowiecki, N., Hill, M., Gehrig, R., Zwicky, C. N., Lienemann, P., Hegedus, F., Falkenberg, G., Weingartner, E., and Baltensperger, U.: Trace metals in ambient air: Hourly size-segregated mass concentrations determined by synchrotron-XRF, Environ. Sci. Technol., 39, 5754-5762, 2005.

Bukowiecki, N., Lienemann, P., Zwicky, C. N., Furger, M., Richard, A., Falkenberg, G., Rickers, K., Grolimund, D., Borca, C., Hill, M., Gehrig, R., and Baltensperger, U.: X-ray fluorescence spectrometry for high throughput analysis of atmospheric aerosol samples: The benefits of synchrotron X-rays, Spectrochim. Acta B, 63, 929-938, 2008.

Bukowiecki, N., Richard, A., Furger, M., Weingartner, E., Aguirre, M., Huthwelker, T., Lienemann, P., Gehrig, R., and Baltensperger, U.: Deposition uniformity and particle size distribution of ambient aerosol collected with a rotating drum impactor, Aerosol Sci. Technol., 43, 891-901, 2009.

DeCarlo, P. F., Slowik, J. G., Worsnop, D. R., Davidovits, P., and Jimenez, J. L.: Particle morphology and density characterization by combined mobility and aerodynamic diameter measurements. Part 1: Theory, Aerosol Sci. Technol., 38, 1185-1205, doi:10.1080/027868290903907, 2004.

Richard, A., Bukowiecki, N., Lienemann, P., Furger, M., Fierz, M., Minguillon, M. C., Weideli, B., Figi, R., Flechsig, U., Appel, K., Prevot, A. S. H., and Baltensperger, U.: Quantitative sampling and analysis of trace elements in atmospheric aerosols: impactor characterization and synchrotron-XRF mass calibration, Atmos. Meas. Tech., 3, 1473-1485, 2010.

Sole, V. A., Papillon, E., Cotte, M., Walter, P., and Susini, J.: A multiplatform code for the analysis of energy-dispersive X-ray fluorescence spectra, Spectrochim. Acta B, 62, 63-68, 2007.

Van Espen, P., Janssens, K., and Nobels, J.: AXIL-PC, software for the analysis of complex X-ray spectra, Chemometrics Intell. Lab. Syst., 1, 109-114, 1986.